MID-INFRARED MULTI-SPECTRUM SENSING AND IMAGING FOR NON-DESTRUCTIVE MATERIAL CHARACTERIZATION

A Dissertation

by

JUNCHAO ZHOU

Submitted to the Graduate and Professional School of
Texas A&M University
in partial fulfillment of the requirements for the degree of

DOCTOR OF PHILOSOPHY

Chair of Committee,	Pao Tai Lin
Committee Members,	Jun Zou
	Steven M. Wright
	Raymundo Arroyave
Head of Department,	Miroslav M. Begovic

May 2022

Major Subject: Electrical Engineering

ABSTRACT

Mid-infrared (mid-IR) spectroscopy has become a powerful technique for chemical analysis. The fingerprint absorption bands in mid-IR can be used to uniquely identify a molecular specie. Such fingerprinting capability along with non-invasive measurement makes mid-IR sensing an ideal technology for applications involving chemical analysis in complex environments, such as pharmaceutical production, clinical health condition monitoring, environment monitoring, and remote sensing. Typically, FTIR is used to obtain the mid-IR spectrum of a specimen. However, such bench-top FTIR instrument is unpractical for field-deployed applications. To address this issue, miniaturized nanophotonic devices are alternatives for mid-IR sensing. The focus of this research is to apply mid-IR sensing technique in non-invasive chemical composition analysis.

First, a mid-IR visualization system was demonstrated to show the capability of mid-IR sensing for ultra-fast chemical identification. The fundamental components for mid-IR sensing were discussed in the experiment. Next, on-chip vortex beam generation from waveguides was studied by FDTD simulation. A spiral phase plate was then fabricated on a glass plate to show the vortex beam generation from 3.0 μm to 3.7 μm experimentally. Third, the second-order nonlinear property of $BaTiO_3$ thin film was studied by second-harmonic generation in the mid-IR region. The nonlinear integrated photonics gives opportunity for on-chip mid-IR light generation. Last, mid-IR integrated photonics for volatile organic compounds (VOC) sensing was studied for enhanced sensitivity. SiN waveguides typically offer 5 times enhancement compared with Si waveguides. Nanoparticles-coated waveguides offer another 10-15 times enhancement. Mid-IR waveguides with nanoparticle coatings is believed to bring the sensitivity towards sub ppm level of VOC gases.

ACKNOWLEDGEMENTS

I am pleased to acknowledge the many individuals, for their support and assistance in different aspects, during the course of this doctoral studies.

First of all, I would like to express my sincere gratitude to my advisor, Dr. Pao-Tai Lin, for his guidance, advice, and invaluable ideas, without which this thesis would not have been possible. Dr. Lin has a gift for seeing the potential in a person even before they see it in themselves, as was the case with me. We had numerous discussions about experimental details, issues in the experiments and how to solve the issues. His ever-friendly attitude gave me the freedom to express, explore and implement new ideas. His patience, optimism, excitement for the work, and frequent encouragement inspired me to stay true to my objectives despite various adversities.

I am tremendously fortunate to have committee members Dr. Zou, Dr. Wright and Dr. Arroyave. I thank them for supporting my thesis work. They provided me with precious advice and critical comments during prelim exam, which enabled me to make necessary improvements for my dissertation.

I also want to thank my lab mates, Tiening Jin, Zhihai Lin, Junyan Li for their help in the experiments. Moreover, I want to thank Dr. Mingzhao Liu and Dr. Ming Lu in Brookhaven National Laboratory, NY for their help in using the equipment in the national lab.

My everlasting gratitude gives to my parents, for their unconditional and continuous love and support. For many years, we could only connect with each other by cell phone. Although you are on the opposite side of the earth, you provide me with the most solid backing for pursing the degree.

CONTRIBUTORS AND FUNDING SOURCES

Contributors

This work was supervised by a dissertation committee consisting of Dr. Lin [advisor], Dr. Zou and Dr. Wright of the Department of Electrical and Computer Engineering and Dr. Arroyave of the Department of Materials Science and Engineering.

All the work conducted for the dissertation was completed by the student independently.

Funding Source

Graduate study was supported by Texas A&M University (TAMU) President's Excellence X-Grants.

NOMENCLATURE

Mid-infrared	Mid-IR
Volatile organic compound	VOC
Fourier transform infrared	FTIR
Point of use	POU
Spiral phase plate	SPP
Figure of merit	FOM
Orbital angular momentum	OAM
Laguerre-Gaussian mode	LG mode
Hermite-Gaussian mode	HG mode
Finite difference time domain	FDTD
Gradient refractive index plate	GRP
Second harmonic generation	SHG
Optical parametric oscillator	OPO
Optical parametric amplifier	OPA
Sum frequency generation	SFG
Difference frequency generation	DFG
Pulsed laser deposition	PLD
Barium titanate	BTO
Strontium titanate	STO
Plasma enhanced chemical vapor deposition	PECVD
Reactive-ion etching	RIE
X-ray diffraction	XRD
Mass flow controllers	MFC

TABLE OF CONTENTS

LIST OF FIGURES

Page

CHAPTER I

INTRODUCTION

1.1 Mid-infrared plays an important role for material characterization

The mid-infrared (mid-IR) spectral region, 2.5 – 20 μm (4000 cm^{-1} – 500 cm^{-1}), has become a key application for sensing chemical molecules because most molecules have intense absorption bands in this region. Depending on the consisting functional groups, different molecules have a series of different absorption bands across the mid-IR region, called molecular-fingerprint absorption bands. A mid-IR spectral analysis of a given molecule thus provides a unique way to non-invasively identify and quantify that molecule in any phase of matter. Figure 1.1 shows some characteristic IR absorption bands of some important organic functional groups. For an organic compound molecule consisting of several functional groups, a combination of several absorption bands will show up in the spectrum, allowing one to speculate the molecule composition. On the other hand, it can be determined if there is a certain molecule contained in the test sample by examining the absorption peaks in the spectrum.

Mid-IR absorption spectroscopy offers numerous applications such as production monitoring for pharmaceutical industry [1], gas sensing for leakage monitoring [2], and label-free detection of proteins for biomedical research [3]. Determination of some key molecules leads to multiple applications. For example, sensing of carbon dioxide for its absorption at 4.3 μm and 15.0 μm in wavelength finds applications in environmental monitoring, air conditioning, and clinical diagnosis such as anesthesia analysis and blood gas analysis. Moreover, mid-IR absorption spectroscopy opens a new path for monitoring diseases by offering real-time and non-invasive detection of biomarkers caused by those diseases. Human breath contains some volatile organic

compounds (VOCs) of very low concentration (ppm or ppb level). Breath analysis by monitoring some VOCs can diagnose conditions such as asthma, liver disease, and lung cancer if the concentration of some VOC biomarkers in the breath are different than their normal levels [4]. There are more applications of mid-IR sensing not limited to the examples listed above. The specificity and non-invasive nature of mid-IR spectroscopy makes it an important technique for sensing and distinguishing molecules in a variety of systems.

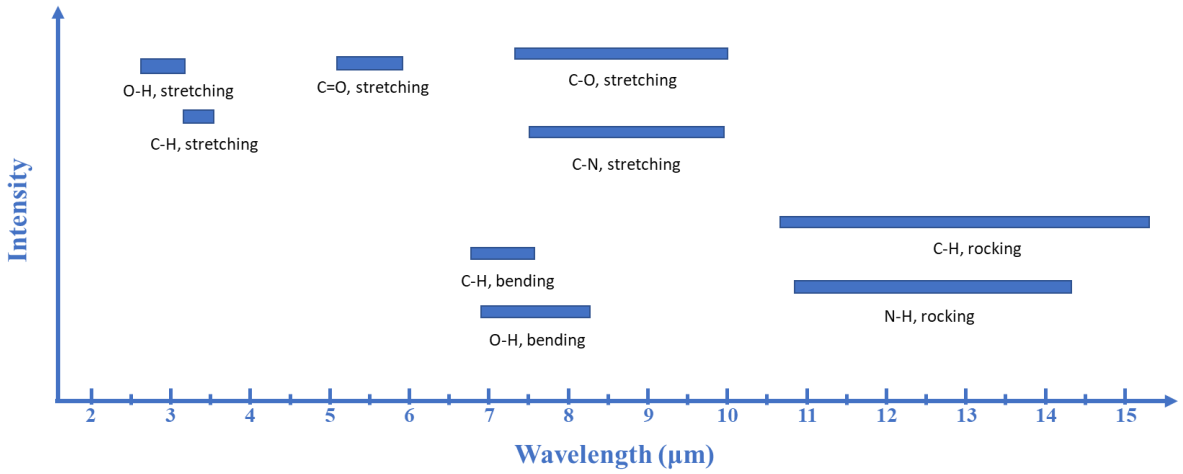

Figure 1.1 Characteristic IR absorption of some important functional groups

1.2 Limitations of conventional mid-IR absorption spectroscopy

Fourier transform infrared spectrometers (FTIR) are mainly used to measure the absorption spectrum of a specimen in the mid-IR region, in order to identify and quantify materials' composition. In an FTIR system, a blackbody radiator is used as an IR light source. IR light detectors such as pyroelectric detectors, cooled photoelectric detectors or liquid nitrogen cooled mercury cadmium telluride (MCT) are the most widely used detectors for the mid-IR light. The IR light is collimated first and then goes through an interferometer before passing through the sample. The IR detectors measures the interferogram of the background and the sample and a Fast-Fourier

Transform (FFT) algorithms is used to convert the interferogram data to a spectrum. The absorption spectrum of the sample is obtained by subtracting the signal from the background. FTIR offers a fast and reproducible way to obtain detailed qualitative and quantitative chemical information of a sample. However, such FTIR system requires a bench-top optical configuration setup, which is unpractical for industry or clinical environment where point-of-use (POU) and real-time monitoring is required. FTIR is also unable to detect chemicals of very low concentration. The detection of chemicals of very low concentration typically requires a very long optical path, which is unpractical for a FTIR system. Therefore, it is significant to develop new mid-IR sensing systems that offers portable, high sensitivity analysis of chemical compositions.

1.3 Mid-IR spectral sensing towards on-chip systems

To address the limitations of FTIR spectroscopy, nanophotonic devices offers a promising route towards enabling miniaturized platforms for IR spectroscopic analysis. On-chip photonics or integrated photonics utilizes dielectric waveguides for absorption spectroscopy [5]. With the development of nonlinear optics, integrated nonlinear photonics provides a promising way for on-chip IR tunable light sources. Thus, we studied the nonlinear optical properties of $BaTiO_3$ in the mid-IR region. Perovskite oxides, such as $LiNbO_3$, $KNbO_3$, and $BaTiO_3$, are attractive materials because they exhibit excellent ferroelectric and nonlinear optical properties at room temperature. Their ferroelectric properties lead to a variety of applications including sensors [6], non-volatile memory devices [7], and optical communications [8,9]. Perovskite oxides have the chemical formula ABO_3, where their polar property determines the polarization, which is the net dipole moment in the unit volume. The nonlinear interactions between the electric dipole and light waves create nonlinear optical responses such as SHG, sum-frequency generation (SFG), difference-

frequency generation (DFG), optical parametric oscillation (OPO), etc [10]. The nonlinear optics technology has been applied to provide light sources over ultraviolet, visible, infrared, and THz bands through nonlinear light conversion [11-13]. For the nonlinear materials in mid-IR, the proposed material is BTO. BTO has a broad transparent window in visible and infrared (IR) range [14,15]. Through the Pockels effect, the refractive indexes of BTO thin films are tunable by applying external electric fields [16,17]. The second order nonlinear susceptibilities of BTO can be further enhanced by inducing stress in the BTO thin film [18]. Moreover, BTO thin films can be epitaxially grown on the Si substrates with an intermediate buffer layer [19,20], thus providing additional functionality to present Si photonic devices.

Vortex beams with orbital angular momentum (OAM) have drawn considerable interest for their broad applications in nonlinear optics [21], quantum optics [22,24], optical tweezers [25], and biosciences [26]. Although OAM has been studied over different spectral ranges, including visible, near-Infrared, and long millimeter waves [27-29], it has not been investigated in the mid-IR regime at λ = 2.5 μm – 15 μm on a chip scale platform. With OAM, mid-IR light can further be used to trap and manipulate small molecules in optical sensing.

1.4 References

[1] Wartewig, Siegfried, and Reinhard HH Neubert. "Pharmaceutical applications of Mid-IR and Raman spectroscopy." Advanced drug delivery reviews 57, no. 8 (2005): 1144-1170.

[2] Jiang, Meng, Xuefeng Wang, Junlong Wang, Yizhao Wang, Pan Li, and Qiaoling Feng. "Research on propane leak detection system and device based on mid infrared laser." In AOPC 2017: Fiber Optic Sensing and Optical Communications, vol. 10464, p. 104641Y. International Society for Optics and Photonics, 2017.

[3] Barth, Andreas. "Infrared spectroscopy of proteins." *Biochimica et Biophysica Acta (BBA)-Bioenergetics* 1767, no. 9 (2007): 1073-1101.

[4] Donodin, Alexander, Vasilii Voropaev, Vladimir Lazarev, Mikhail Tarabrin, Konstantin Kudrin, Igor Reshetov, and Valerii Karasik. "Femtosecond thulium-doped fiber-ring laser for mid-IR spectroscopic breath analysis." In *Saratov Fall Meeting 2018: Laser Physics, Photonic Technologies, and Molecular Modeling*, vol. 11066, p. 1106603. International Society for Optics and Photonics, 2019.

[5] Katiyi, Aviad, and Alina Karabchevsky. "Figure of merit of all-dielectric waveguide structures for absorption overtone spectroscopy." *Journal of Lightwave Technology* 35, no. 14 (2017): 2902-2908.

[6] D. Damjanovic, P. Muralt and N. Setter. "Ferroelectric sensors." *IEEE Sensors Journal*, **1**, 191-206 (2001).

[7] A. Chanthbouala, A. Crassous, V. Garcia, K. Bouzehouane, S. Fusil, X. Moya, J. Allibe, B. Dlubak, J. Grollier, S. Xavier, C. Deranlot, A. Moshar, R. Proksch, N. D. Mathur, M. Bibes and A. Barthelemy. "Solid-state memories based on ferroelectric tunnel junctions." *Nature Nanotechnology* **7**, 101 (2012).

[8] D. Sando, Y. Yang, C. Paillard, B. Dkhil, L. Bellaiche and V. Nagarajan. "Epitaxial ferroelectric oxide thin films for optical applications." *Applied Physics Reviews* **5**, 041108 (2018).

[9] C. Xiong, W. H. P. Pernice, J. H. Ngai, J. W. Reiner, D. Kumah, F. J. Walker, C. H. Ahn and H. X. Tang. "Active silicon integrated nanophotonics: ferroelectric BaTiO3 devices." *Nano Letters* **14**, 1419-1425 (2014).

[10] N. Bloembergen, "Nonlinear Optics." World Scientific, River Edge, NJ, 4th edition, 1996. ISBN 978-981-02-2598-8.

[11] A. Hermans, C. Kieninger, K. Koskinen, A. Wickberg, E. Solano, J. Dendooven, M. Kauranen, S. Clemmen, M. Wegener, C. Koos and R. Baets. "On the determination of χ (2) in thin films: a comparison of one-beam second-harmonic generation measurement methodologies." *Scientific Reports* **7** 44581 (2017).

[12] L. E. Myers, R. C. Eckardt, M. M. Fejer, R. L. Byer, W. R. Bosenberg and J. W. Pierce. "Quasi-phase-matched optical parametric oscillators in bulk periodically poled $LiNbO_3$." *Journal of the Optical Society of America B* **12**, 2102-2116 (1995).

[13] M. A. Belkin, F. Capasso, A. Belyanin, D. L. Sivco, A. Y. Cho, D. C. Oakley, C. J. Vineis and G. W. Turner. "Terahertz quantum-cascade-laser source based on intracavity difference-frequency generation." *Nature Photonics* **1**, 288 (2007).

[14] Y. Garbovskiy and A. Glushchenko. "Optical/ferroelectric characterization of $BaTiO_3$ and $PbTiO_3$ colloidal nanoparticles and their applications in hybrid materials technologies." *Applied Optics* **52**, E34-E39 (2013).

[15] M. K. Trivedi, G. Nayak, S. Patil, R. M. Tallapragada, O. Latiyal and S. Jana. "Impact of biofield treatment on atomic and structural characteristics of barium titanate powder." *Industrial Engineering Management*, **4**, pp.1000166 (2015).

[16] P. T. Lin, Z. Liu and B. W. Wessels. "Ferroelectric thin film photonic crystal waveguide and its electro-optic properties." *Journal of Optics A: Pure and Applied Optics* **11**, 075005 (2009).

[17] A. Petraru, M. Siegert, M. Schmid, J. Schubert and Ch. Buchal. "Ferroelectic $BaTiO_3$ Thin Film Optical Waveguide Modulators." MRS Online Proceedings Library Archive **688** (2001).

[18] T. Zhao, H. Lu, F. Chen, G. Yang and Z. Chen. "Stress-induced enhancement of second-order nonlinear optical susceptibilities of barium titanate films." *Journal of Applied Physics* **87**, 7448-7451 (2000).

[19] M. B. Lee, , M. Kawasaki, M. Yoshimoto and H. Koinuma. "Heteroepitaxial growth of $BaTiO_3$ films on Si by pulsed laser deposition." *Applied Physics Letters* **66**, 1331-1333 (1995).

[20] M. H. M. Hsu, D. Van Thourhout, M. Pantouvaki, J. Meersschaut, T. Conard, O. Richard, H. Bender, P. Favia, M. Vila and R. Cid. "Controlled orientation of molecular-beam-epitaxial $BaTiO_3$ on Si (001) using thickness engineering of $BaTiO_3$ and $SrTiO_3$ buffer layers." *Applied Physics Express* **10**, 065501 (2017).

[21] Neshev D N, Alexander T J, Ostrovskaya E A, Kivshar Y S, Martin H, Makasyuk I and Chen Z 2004 Observation of discrete vortex solitons in optically induced photonic lattices *Physical Review Letters* **92** 123903.

[22] Andersen M, Ryu C, Cladé P, Natarajan V, Vaziri A, Helmerson K and Phillips W D 2006 Quantized rotation of atoms from photons with orbital angular momentum *Physical Review Letters* **97** 170406.

[23] Barreiro S and Tabosa J 2003 Generation of light carrying orbital angular momentum via induced coherence grating in cold atoms *Physical Review Letters* **90** 133001.

[24] Mair A, Vaziri A, Weihs G, Zeilinger A 2001 Entanglement of the orbital angular momentum states of photons *Nature* **412** 313-316.

[25] He H, Friese M E J, Heckenberg N R, Rubinsztein-Dunlop H 1995 Direct observation of transfer of angular momentum to absorptive particles from a laser beam with a phase singularity *Physical Review Letters* **75** 826-829.

[26] Grier D G 2003 A revolution in optical manipulation Nature **424** 810-816.

[27] Karimi E, Schulz S A, De Leon I, Qassim H, Upham J and Boyd R W 2014 Generating optical orbital angular momentum at visible wavelengths using a plasmonic metasurface *Light: Science & Applications* **3** e167.

[28] Simpson N, Dholakia K, Allen L and Padgett M 1997 Mechanical equivalence of spin and orbital angular momentum of light: an optical spanner *Optics Letters* **22** 52-54.

[29] Yan Y, Xie G, Lavery M P, Huang H, Ahmed N, Bao C, Ren Y, Cao Y, Li L and Zhao Z 2014 High-capacity millimetre-wave communications with orbital angular momentum multiplexing *Nature Communications* **5** 4876.

[30] Cai, D.; Neyer, A.; Kuckuk, R.; Heise, H. M. Raman, mid-infrared, near-infrared and ultraviolet-visible spectroscopy of PDMS silicone rubber for characterization of polymer optical waveguide materials. *J. Mol. Struct.* **2010**, 976, 274-281.

[31] Aguiar, K. R.; Santos, V. G.; Eberlin, M. N.; Rischka, K.; Noeske, M.; Tremiliosi-Filho, G.; Rodrigues-Filho, U. P. Efficient green synthesis of bis(cyclic carbonate)poly(dimethylsiloxane) derivative using CO_2 addition: a novel precursor for synthesis of urethanes. *RSC Adv.* **2014**, 4, 24334-24343.

[32] H. D. Megaw, "Origin of ferroelectricity in barium titanate and other perovskite-type crystals." *Acta Crystallographica* **5**, 739-749 (1952).

[33] S. A. Denev, T. TA Lummen, E. Barnes, A. Kumar and V. Gopalan. "Probing ferroelectrics using optical second harmonic generation." *Journal of the American Ceramic Society* **94**, 2699-2727 (2011).

[34] O. Diéguez, K. M. Rabe and D. Vanderbilt. "First-principles study of epitaxial strain in perovskites." *Physical Review B* **72**, 144101 (2005).

CHAPTER II

MID-INFRARED MULTI-SPECTRAL ANALYSIS OF STRUCTURE AND COMPOSITION OF MATERIALS[*]

2.1 Introduction

In this work we developed a mid-IR vision system that implements multi-spectral and robotic scanning techniques. This platform is not only capable of tracking objects, but also differentiating materials simultaneously, because the mid-IR spectrum overlaps with the characteristic and finger-print absorptions assigned to numerous chemical functional groups. Hence, images captured in mid-IR reveal the object structures and provide information associated with the chemical compositions and the material properties [1,2]. In addition, recent progress has demonstrated that the complementary metal–oxide–semiconductor (CMOS) technology has the capability to manufacture mid-IR microphotonic devices [3]. Thus, it will lead the integration of the mid-IR components, such as its light source and detectors, with present vision microprocessors [4-6]. The mid-IR sensing platform can be applied for pharmaceutical technology, biomedical applications, and manufacturing [7-9], where spatial and chemical analyses are both required. For instance, in pharmaceutical systems, real-time and multi-point monitoring is required during the drug–polymer phase separation process. Similarly, for biomedical diagnosis, imaging with chemical property requisition is desired for cell screening. The mid-IR scanning system overcomes challenges of present Fourier Transform Infrared - Attenuated Total internal Reflection (FTIR-ATR), which can only acquire a spectrum at a discrete single point, thus making it unable to efficiently provide

[*] Reprinted with permission from "Midinfrared multispectral detection for real-time and noninvasive analysis of the structure and composition of materials." by Junchao Zhou and Pao-Tai Lin, 2018. *ACS Sensors* 3, no. 7 1322-1328, Copyright @ 2018 American Chemical Society.

spatial material information. In addition, FTIR-ATR needs to be directly in contact with the samples during the measurement, so it is not suitable for remote/non-contact sensing.

In brief, this work provides a new machine vision platform able to achieve real-time and non-invasive object tracking and material characterization. This new functionality of material visualization will grant robotics additional sensing intelligence for extensive applications, such as agriculture evaluation, biomedical imaging, and environmental toxics monitoring.

2.2 System Overview

2.2.1 Block diagram of the mid-IR visualization system

Figure 2.1 (a) is the block diagram illustrating the three major components of the mid-IR visualization system: a mid-IR tunable laser, robotic scanning stages, and mid-IR signal receivers. Combination of these components allowed the system to tune the light wavelengths for multi-spectral analysis and to regulate the object scanning speeds for optimization of the data acquisition rates. Both structural profiles and material properties were revealed after interpreting the spectrally attenuated light intensity. In detail, the tunable laser was used to illuminate the sample objects. Its wavelength was tuned to align with various mid-IR absorption bands that correspond to the chemical functional groups of interest. Hence, objects made by different chemicals were able to be differentiated through the spectra collected from the transmitted light. The tunable laser had a narrow emission linewidth that prevented inaccuracy caused by spectral crosstalk. In parallel, dynamic object tracking was achieved using an agile scanning stage. The testing objects were attached onto the surface of a rotating plate that was anchored to a spinner driven by a stepper motor. The plate rotational speed and the object positions were controlled by a LabVIEW installed computer. At the end of the system, the signal receiver was a single pixel detector or a camera that recorded the mid-IR intensity variation after the light transmitted through the rotating plate. The

accuracy of the object position tracking and the material identification depended on the rotation speed of the plate as well as the response time of the signal receptor. This mid-IR visualization technique was capable of analyzing material properties such as chemical compositions and elemental distribution. Thus, it provides a novel functionality beyond conventional visible or NIR vision systems that are limited to sorting out structural information like the shape, size, or position.

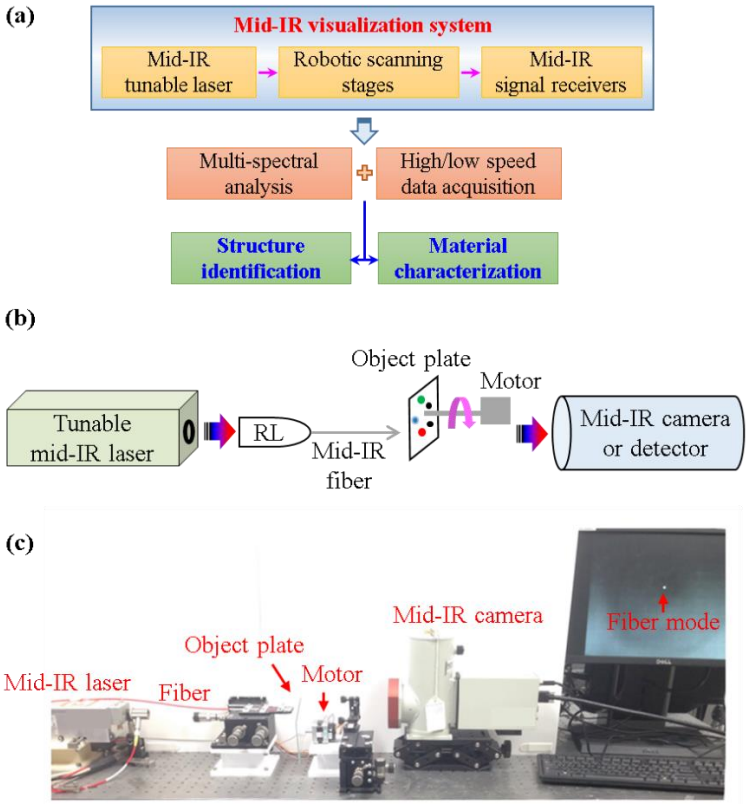

Figure 2.1 (a) The block diagram for the mid-IR visualization system. It includes three major components: the mid-IR laser, scanning stages, and the signal receivers. The multispectral data, at λ = 2.45 to 3.7 μm, was acquired in either high speed (ω > 200 rpm) or low speed (ω < 0.5 rpm) rotating rates. The system can provide material and structural information simultaneously. (b) The schematic of the experimental setup and (c) the actual configuration of the mid-IR scanning system. The mid-IR light from the laser was coupled into the front end of the mid-IR fiber using reflective collimated lens (RL). The light emitted from the fiber was then projected into an object plate that contained SU-8 and PDMS samples. The plate was connected to a motor and rotated at a speed ω. The fiber mode after passing through the plate was monitored by a mid-IR camera or a photodetector.

2.2.2 Experimental setup of the mid-IR visualization system

The mid-IR system can profile mobile targets and instantaneously identify their material properties. Meanwhile, there were two modes available in operation, one at a lower scanning speed and the other at a higher speed. The schematic of the experimental setup and the actual configuration of the scanning system are displayed in Figure 2.1 (b) and (c), respectively. The tunable pulsed laser had a narrow linewidth of 5 nm and the emission wavelength can be tuned from $\lambda = 2.50$ to 3.70 μm. The laser pulse duration was 10 ns with a 150 kHz repetition rate. The mid-IR light was initially coupled into the front end of a single mode fiber through a reflective collimated lens. The back end of the fiber was placed next to the rotation plate so the light emitted from the fiber was projected toward the plate before the light beam became widely diverged. During the low-speed scanning test, the rotation rate of the stepper motor was set at 0.26 rpm. The image and intensity of the fiber mode after passing through the object plate were continuously monitored by a mid-IR camera. On the other hand, in the high-speed scanning test, the rotation rate was increased to 231 rpm. The signal receiver was replaced by a 1.6 MHz bandwidth mid-IR photodetector and then connected to a 2 GHz oscilloscope, so the fast-varying intensity of the fiber mode could be recorded and analyzed instantaneously.

The testing objects were made by two different chemicals, polydimethylsiloxane (PDMS) and SU-8, to show that the mid-IR visualization system was capable of performing real-time material identification in addition to position tracking. PDMS and SU-8 were selected because they can be easily patterned on the substrate and can be differentiated using the mid-IR light. Though SU-8 and PDMS are both transparent in the visible spectrum, they have distinct mid-IR absorption spectra [10-12]. Figure 2.2 (a) illustrates the design of the plate and the coordination of the testing objects. For a circular array of SU-8 objects, their angular separation between adjacent spots were

15º, 30º, 45º, 60º, 75º, 90º, and 45º, counting clockwise. For the other array made by PDMS, the relative angular positions between neighboring spots were 70º, 55º, 95º, 55º, 40º, and 45º. These round objects had a 1 cm diameter and were placed at 4.5 cm away from the plate center. Figure 2.2 (b) shows the fabricated testing plate with the PDMS and SU-8 objects on its surface. The PDMS samples were prepared by the injection molding process and then adhered onto the plate surface. For SU-8, the samples were patterned on the surface by photolithography. The thickness of the SU-8 objects measured by a profilometer was 60 μm. The testing plate was then mounted on a PC controlled stepper motor to carry on the mid-IR visualization test.

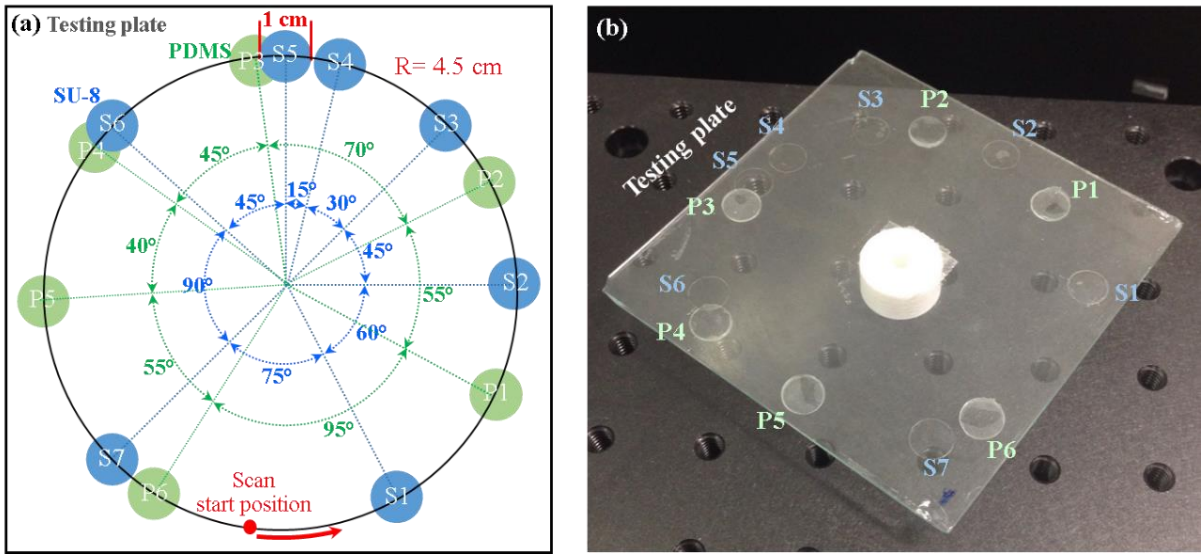

Figure 2.2 (a) The design of the testing plate. The coordination of the SU-8 and PDMS objects are represented by the blue and green circles, respectively. The radius of the circular scanning path, R, is 4.5 cm. (b) The fabricated 10 × 10 cm testing plate and the SU-8 and PDMS circles with a diameter of 1 cm.

2.3 Results and discussion

2.3.1 Characteristic mid-IR absorption of PDMS and SU-8

Figure 2.3 (a) and (b) show the infrared transmission spectra of the SU-8 and the PDMS at λ = 2.50 - 3.70 μm measured by using the mid-IR tunable laser. From Figure 2.3 (a), SU-8 had two absorption bands, one at λ = 2.78 - 3.12 μm associated with the O–H stretch and the other at λ = 3.30 - 3.54 μm caused by the aromatic C–H stretch. On the other hand, from Figure 2.3 (b) PDMS had a strong absorption at λ = 2.70 - 3.00 μm and λ = 3.20 - 3.60 μm due to the asymmetric C–H stretching from the Si-CH_3 group [13,14]. Clearly, SU-8 and the PDMS revealed distinct mid-IR absorption spectra because of their dissimilar chemical functional groups and molecular structures. For SU-8, it consists of rigid aromatic rings and epoxy rings, while the major functional group of PDMS is siloxane. Thus, samples composed of SU-8 and PDMS can be differentiated by imaging those objects at wavelengths corresponding to their unique absorption bands.

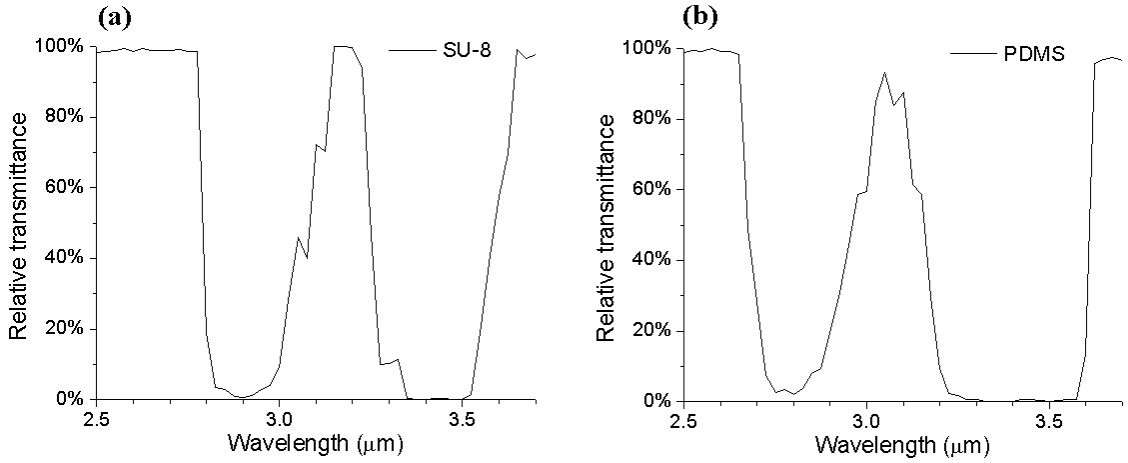

Figure 2.3 The infrared transmission spectra of (a) the SU-8 and (b) the PDMS at λ = 2.50 - 3.70 μm. SU-8 had strong absorption at λ = 2.78 - 3.12 μm and 3.30 - 3.54 μm due to the characteristic O–H and C–H absorptions. PDMS showed absorption at λ = 2.70 - 3.00 μm and λ = 3.20 - 3.60 μm due to the Si-CH_3 functional group.

Figure 2.4 displayed the mid-IR fiber mode after the light passed through the SU-8 and PDMS objects. The mode images were captured at various wavelengths. At λ = 2.54 μm, a sharp fundamental fiber mode was found after transmitting through SU-8 and PDMS, indicating SU-8 and PDMS were both transparent at that wavelength. Upon tuning the wavelength to λ = 2.98 μm, the mode after SU-8 became much darker because of the O–H strong characteristic absorption. Nevertheless, the mode after PDMS remained sharp and clear since PDMS was transparent at λ = 2.98 μm. Once the wavelength shifted to λ = 3.46 μm the fiber mode disappeared after SU-8; similarly, only a tiny and blurred spot was left after PDMS. The decreasing mode intensity at λ = 3.46 μm was caused by the characteristic C–H absorption existing in both PDMS and SU-8. Clearly, the observed spectral attenuation of the fiber mode was determined by the infrared absorption bands associated with the testing objects. Thus, the mid-IR scanning technique was able to visualize the material compositions.

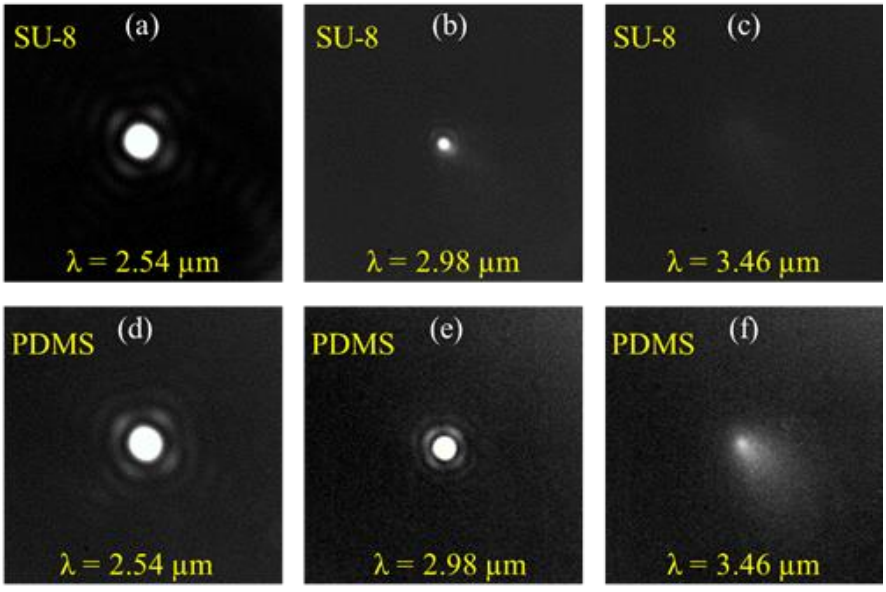

Figure 2.4. Optical images of the mid-IR fiber mode after passing through the SU-8 and the PDMS objects. The fiber light was tuned to three different wavelengths: (a) and (d) at λ = 2.54 μm, (b) and (e) at λ = 2.98 μm, and (e) and (f) at λ = 3.46 μm. SU-8 and PDMS were both transparent at λ = 2.54 μm. At λ = 2.98 μm, SU-8 showed stronger absorption than PDMS. At λ = 3.46 μm, SU-8 and PDMS were opaque.

2.3.2 Material identification using mid-IR fiber scanning at low speed

Real-time and non-invasive material identification was carried out by the mid-IR fiber scanning method. The design and the preparation of the testing plate and objects were previously illustrated in the section Experimental Setup. Figure 2.5 (a) displays the sequence of the SU-8 and PDMS objects in time. Figure 5 (b) - (f) show the transient response of the fiber mode intensity when the object plate was rotated at 0.26 rpm, which is equivalent to a full rotation in 231 s. The absorptions caused by the SU-8 and PDMS were indicated by red and green arrows, respectively. Five different wavelengths at λ = 2.54, 2.74, 2.98, 3.22 and 3.46 μm were chosen to perform the fiber scanning. Figure 2.3 showed that SU-8 has strong absorption at λ = 2.98 and 3.46 μm, while PDMS has strong absorption at λ = 2.74, 2.98, 3.22 and 3.46 μm. On the other hand, PDMS and SU-8 were both transparent at λ = 2.54 μm, but opaque at 3.46 μm. Overall, the mid-IR scanning was operated at three different spectral regimes: **I.** PDMS and SU-8 were both transparent, **II.** PDMS had a stronger absorption than SU-8, **III.** PDMS and SU-8 both were opaque. The figure of merit (FOM) is used to estimate the sensitivity of the device and is defined as follows:

$$FOM = \left|\frac{A_{PDMS} - A_{SU-8}}{A_{PDMS} + A_{SU-8}}\right| \qquad (1)$$

, where A_{PDMS} and A_{SU-8} are the intensity attenuations caused by PDMS and SU-8.

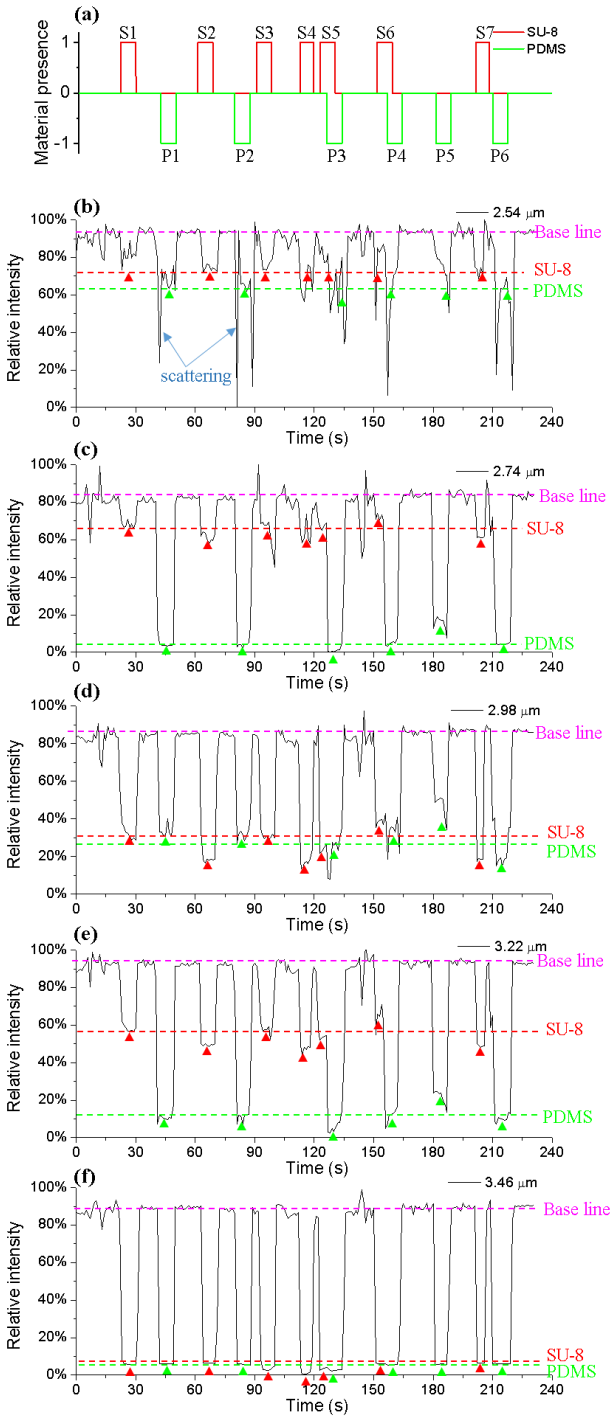

Figure 2.5 (a) The arrangement of the SU-8 and PDMS objects in time. (b) – (f) The transient response of the fiber mode intensity at $\omega = 0.26$ rpm. The wavelength was adjusted to $\lambda = 2.54$, 2.74, 2.98, 3.22, and 3.46 μm, in sequence. The red and the green arrows indicate the absorption caused by the SU-8 and PDMS objectives, respectively. At (b), the spike-like intensity variation was caused by scattering. At (c) and (e), PDMS showed stronger absorption than the SU-8. At (d) and (f), PDMS and SU-8 had similar absorption.

I. At λ = 2.54 μm. As shown in Figure 2.5 (b), there were two types of intensity attenuation, one appeared to be a sharp intensity change like a spike, while the other attenuation lasted longer, for few seconds. The spike-like intensity variation appeared whenever the scanning fiber encountered the edges of the objects because the fiber light was scattered. On the other hand, the intensity change with a longer duration happened when the scanning fiber crossed over an SU-8 and a PDMS object. The decrease of the light transmission was due to the reflection at the interfaces between the air, the testing plate, and the objects. Thus, the intensity attenuation at λ = 2.54 μm was attributed to the configuration of the objects on the testing plate, including the structures and the positions, instead of their mid-IR absorption.

II. At λ = 2.74 and 3.22 μm. Figure 2.5 (c) is the plot of the light attenuation at λ = 2.74 μm where two different modulation depths were found. The larger attenuation was attributed to the PDMS object, because at λ = 2.74 μm PDMS had much stronger absorption compared to the SU-8. Similar absorption patterns were found in Figure 2.5 (e) when the wavelength was adjusted to λ = 3.22 μm. The spatial coordination and the relevant angular positions of the objects can be extrapolated from the transient intensity plots. This is because at a constant rotation speed the time was linearly related to the angular coordinate. Here, each temporal intensity variation was caused by an object encounter. Based on the intensity attenuation of the objects, the material of the detected objects was revealed. The larger attenuation was assigned to PDMS and the smaller to SU-8. A sequence with an object order of S1 – P1 – S2 – P2 – S3 – S4 – S5 – P3 – S6 – P4 – P5 – S7 – P6 was then resolved. The S and P denoted the SU-8 and PDMS, respectively. At a spinning rate of 0.026 rpm, the circular scanning repeated the intensity pattern after every 231 s interval. The sequence obtained from the system at λ = 2.74 and 3.22 μm exactly matched the object layouts

displayed in Figure 2 (a), indicating the mid-IR platform can precisely track the position of arrays of objects as well as visualize their material compositions.

III. At λ = 2.98 and 3.46 μm. As shown in Figure 2.5 (d), at λ = 2.98 μm, SU-8 and PDMS introduced similar intensity attenuation because their absorption was comparable at that wavelength. Likewise, Figure 2.5 (f) illustrated that the attenuation of these two materials was nearly identical at λ = 3.46 μm, so only one modulation depth was found over time. In addition, sharp edges following strong intensity variation were obtained instead of the spike-like patterns caused by scattering, like those observed in Figure 2.5 (b). Therefore, at λ = 2.98 and 3.46 μm, absorption was the dominant effect during the mid-IR scanning and it overwhelmed the scattering effect.

The FOM of the device at each wavelength can be calculated from Figure 5. The highest FOM was obtained at λ = 2.74 μm, where PDMS has a strong absorption A_{PDMS} = 80% and SU-8 has a lower absorption A_{SU-8} = 19%. Based on equation (1), the FOM is 0.62 at λ = 2.74 μm and at low scanning speed.

2.3.3 Material identification using mid-IR fiber scanning at high speed

The developed mid-IR visualization system was capable of performing high speed fiber scanning. The rotation speed of the object plate was increased from 0.26 rpm to 231 rpm, which was equivalent to a lateral scanning rate of 109 cm/s, and the time interval to complete a full rotation was 0.26 second. The scanning wavelengths were selected at λ = 2.50, 2.74, 3.00, and 3.46 μm. From Figure 2.3, PDMS was transparent at λ = 2.50 μm, while SU-8 was transparent at λ = 2.50 and 2.74 μm. Figure 6 (a) displays the order of the SU-8 and PDMS objects in time. The scanning results at different wavelengths are drawn in Figure 2.6 (b) - (e).

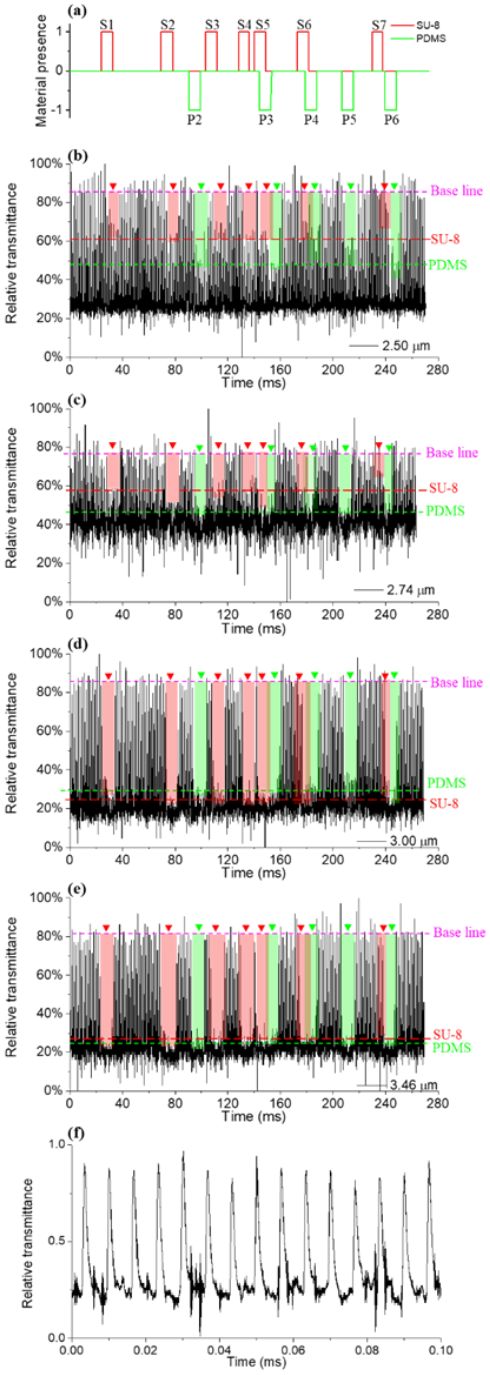

Figure 2.6 (a) The arrangement of the SU-8 and PDMS objects in time. (b) – (e) The transient response of the fiber mode intensity at ω = 231 rpm. The wavelength was adjusted to λ = 2.50, 2.74, 3.00, and 3.46 μm, in sequence. (f) The magnified diagram of the transient plots shows a train of short and discrete signals. At (b) and (c), PDMS showed stronger absorption than SU-8. At (d) and (e), PDMS and SU-8 caused comparable intensity attenuation.

I. At $\lambda = 2.50$ μm. As shown in Figure 2.6 (b), intensity attenuations were observed even though PDMS and SU-8 were both transparent. This is due to the light reflection that was introduced by the interfaces between the objects and the testing plates. Thus, the intensity variation at this wavelength was more relevant to structure features, such as edges of objects or additional interfaces on the object plate, instead of the infrared absorption.

II. At $\lambda = 2.74$ μm. Two different modulation depths were found in Figure 2.6 (c). The stronger attenuation was associated with PDMS while the weaker was attributed to SU-8, since PDMS had higher absorption than SU-8 at this wavelength. The angular positions of the objects were resolved as S1 – S2 – P2 – S3 – S4 – S5 – P3 – S6 – P4 – P5 – S7 – P6. The intensity patterns in Figure 2.5 (c) and Figure 2.6 (c) were noticeably similar since they were both characterized at $\lambda = 2.74$ μm. In addition, P1 was removed during the high speed test, and the rearrangement of objects was observed in the scanning measurement.

III. At $\lambda = 3.00$ and 3.46 μm. Once the wavelength reached $\lambda = 3.00$ μm in Figure 2.6 (d), only one modulation depth was found, like the result displayed in Figure 2.5 (d). In addition, the same pattern profile was found at $\lambda = 3.46$ μm as shown in Figure 2.6 (e). This was because SU-8 and PDMS both had strong absorption at these two wavelengths.

The transmission curves displayed in Figure 2.6 (b) - (e) were compiled by a train of short and discrete signals which are illustrated in the magnified diagram in Figure 2.6 (f). The scanning system had a 150 kHz sampling rate that was determined by the repetition rate of the mid-IR pulsed laser. Thus, the separation between adjacent pulses was 6.67×10^{-3} us. In addition, at $\lambda = 2.74$ μm, the A_{PDMS} was 32% and the A_{SU-8} was 19%, so the FOM at high-speed scanning was 0.26. The variation of FOM at different scanning speeds is due to the difference of the responsivity between the mid-IR camera and the detector. From Figure 2.6, we demonstrated that mid-IR robotic

scanning is capable of recognizing different materials through the multi-spectral method even when the system was operated in fast scanning rates. The non-invasive visualization enables accurate and real-time monitoring, which is critical for applications including micro-reactors and lab on-a-chip that require in-situ and in-parallel chemical analysis.

2.4 Conclusions

In summary, we present a robotic scanning system that accomplished object tracking and material identification instantaneously. The system consisted of a probe fiber connected with a mid-IR tunable laser, a programmable rotation stage, and a mid-IR camera and high-speed detector as the signal receivers. Applying multi-spectral scanning, the system was able to distinguish objects which are transparent in the visible spectrum and made by different chemicals. In the case of distinguishing PDMS and SU-8 objects, a mid-IR probe was operated at $\lambda = 2.74$ and 3.22 μm because PDMS possesses strong characteristic absorption caused by C–H and O–H groups. The scanning system can accurately track fast moving objects on a plate rotating above 210 rpm. Thus, the robotic system provides a new visualization technology that enables the real-time and nondestructive monitoring demanded for industrial manufacturing and biomedical diagnostics.

2.4 References

[1] Bechtel, H. A.; Muller, E. A.; Olmon, R. L.; Martin, M. C.; Raschke, M. B. Ultrabroadband infrared nanospectroscopic imaging. *Proc. Natl. Acad. Sci.* **2014**, 111, 7191-7196.

[2] Petersen, C. R.; Møller, U.; Kubat, I.; Zhou, B.; Dupont, S.; Ramsay, J.; Benson, T.; Sujecki, S.; Abdel-Moneim, N.; Tang, Z.; Furniss, D.; Seddon, A.; Bang, O. Mid-infrared supercontinuum covering the 1.4-13.3 µm molecular fingerprint region using ultra-high NA chalcogenide step-index fibre. *Nat. Photonics* **2014**, 8, 830-834.

[3] Carletti, L.; Monat, C.; Orobtchouk, R.; Rojo-Romeo, P.; Lin, Z.; Jamois, C.; Leclerc, J.-L.; Viktorovitch, P.; Letartre, X.; Grillet, C. Mid-IR integrated photonics for sensing applications, in *Proc. SPIE* 9370, Quantum Sensing and Nanophotonic Devices XII, 93701J (8 February 2015).

[4] Lin, P.; Singh, V.; Wang, J.; Lin, H.; Hu, J.; Richardson, K.; Musgraves, J. D.; Luzinov, I.; Hensley, J.; Kimerling, L. C.; Agarwal, A. Si-CMOS compatible materials and devices for mid-IR microphotonics. *Opt. Mater. Express* **2013**, 3, 1474-1487.

[5] Lin, P.; Kwok, S. W.; Lin, H-Y G.; Singh, V.; Kimerling, L. C.; Whitesides, G. M.; Agarwal, A. Mid-infrared spectrometer using opto-nanofluidic slot-waveguide for label-free on-chip chemical sensing. *Nano Lett.* **2013**, 14, 231-238.

[6] Lin, P.; Singh, V.; Hu, J.; Richardson, K.; Musgraves, J. D.; Luzinov, I.; Hensley, J.; Kimerling, L. C.; Agarwal, A. Chip-scale mid-infrared chemical sensors using air-clad pedestal silicon waveguides. *Lab on a Chip* **2013**, 13, 2161-2166.

[7] Higashi, K.; Ueda, K.; Moribe, K. Recent progress of structural study of polymorphic pharmaceutical drugs. *Adv. Drug Deliv. Rev.* **2017**, 117, 71-85.

[8] Van Eerdenbrugh, B.; Lo, M.; Kjoller, K.; Marcott, C.; Taylor, L.S.; Nanoscale mid-infrared imaging of phase separation in a drug–polymer blend. *J. Pharm. Sci.* **2012**, 101, 2066-2073.

[9] Talari, A. C. S.; Martinez, M. A. G.; Movasaghi, Z.; Rehman, S.; Rehman, I. U. Advances in Fourier transform infrared (FTIR) spectroscopy of biological tissues. *Appl. Spectrosc. Rev.* **2017**, 52, 456-506.

[10] Kalaiselvi, S. M. P.; Tan, T. L.; Rawat, R. S.; Lee, P.; Heussler, S. P.; Breese. M. B. H. FTIR spectroscopic studies on cross linking of Su-8 photoresist. *Cosmos* **2013**, 9, 37-46.

[11] Robin, C. J.; Jonnalagadda, K. N. Effect of size and moisture on the mechanical behavior of SU-8 thin films. *J. Micromech. Microeng.* **2016**, 26, 025020.

[12] Johnson, L. M.; Gao, L.; Shields IV, G. W.; Smith, M.; Efimenko, K.; Cushing, K.; Genzer, J.; Lopez, G. P. Elastomeric microparticles for acoustic mediated bioseparations. *J. Nanobiotechnology* **2013**, 11, 22.

[13] Cai, D.; Neyer, A.; Kuckuk, R.; Heise, H. M. Raman, mid-infrared, near-infrared and ultraviolet-visible spectroscopy of PDMS silicone rubber for characterization of polymer optical waveguide materials. *J. Mol. Struct.* **2010**, 976, 274-281.

[14] Aguiar, K. R.; Santos, V. G.; Eberlin, M. N.; Rischka, K.; Noeske, M.; Tremiliosi-Filho, G.; Rodrigues-Filho, U. P. Efficient green synthesis of bis(cyclic carbonate)poly(dimethylsiloxane) derivative using CO_2 addition: a novel precursor for synthesis of urethanes. *RSC Adv.* **2014**, 4, 24334-24343.

CHAPTER III

MID-IR VORTEX BEAM GENERATION[*,**]

3.1 Introduction

Light with orbital angular momentum (OAM) or optical vortices was first observed when there was a change of angular momentum larger than $\hbar$ during higher-order atomic or molecular transitions[1,2]. Later, Allen et.al. demonstrated that light beams carrying OAM can be achieved by an astigmatic optical system[3], and the results led to various applications such as transferring OAM to atoms[4]. More recently, light beams with OAM draw considerable interest in optical communication because of their infinite eigenstates providing additional bandwidth that improved the data transmission rates[5,6]. In addition, the angular momentum of light can be utilized in nonlinear optics[7], quantum optics[8-10], optical tweezers[11], and biosciences[12]. In recent years, Airy-like beams carrying optical vortices were explored extensively due to their non-diffraction and self-acceleration behavior[13-15]. And the interplay between the topological phase and self-acceleration was discussed thoroughly[16]. Although OAM has been studied over different spectral ranges, including visible, near-Infrared, and long millimeter waves[17-19], it has not been investigated in the mid-IR regime at λ = 2.5 μm – 15 μm on a chip scale platform. Mid-IR has shown its potential in optical networking[20-22], biomedical sensing[23,24], molecular spectroscopy[25], and thermal imaging[26]. For communication, mid-IR has provided a broader spectrum that accommodated additional channels for high-speed data transmission. Meanwhile, for biomedical sensing, mid-IR has enabled label-free molecule detection because its spectrum

[*] Reprinted with permission from "Efficient mid-Infrared vortex beam generation using optical waveguides integrated with micro-spiral phase plates." by Junchao Zhou and Pao-Tai Lin, 2019. *Journal of Optics* 21, no. 10 105801, Copyright @ 2019 IOP Publishing Ltd.

[**] Reprinted with permission from "Efficient vortex beam generation using gradient refractive-index microphase plates."by Junchao Zhou and Pao-Tai Lin, 2021. *Applied Optics* 60, no. 13, 3997-4003, Copyright @ 2021 Optica Publishing Group

overlapped with characteristic absorption of various chemical functional groups. Thus, it is critical to explore a methodology that can efficiently generate mid-IR light with OAM using a chip-scale platform.

It has shown that a light beam with the Laguerre-Gaussian (LG) mode retained OAM properties[1,27]. The LG mode beam can be formed by two approaches, direct generation or external optical mode transformation. The first approach includes thermal lensing[28], reflectivity modulation of a cavity mirror[29], or a higher-order LG mode excitation through a ring-shaped pump beam[30]. However, this approach was not able to actively control the helical phase front handedness of the LG mode beam, since the mechanism to select the topological charge has not been fully investigated. The second approach is to transform the Hermite-Gaussian (HG) modes into the required LG modes with helical phase fronts, where angular phase changes by integer multiples of 2π are required. The HG to LG mode conversion can be achieved by spatial light modulators[31], holograms[32], and spiral phase plates (SPP). In the far field of a LG beam, destructive interference occurs in the beam center because of its helicoidally shaped wavefront, which leads to a vortex beam with a characteristic donut-shaped intensity profile. Among the methods in creating LG modes, SPP has the advantages of high OAM generation efficiency as well as simplicity in experimental set-up.

3.2 FDTD simulation of mid-Infrared vortex beam generation using optical waveguides integrated with micro-spiral phase plates

3.2.1 Motivation

We proposed a device platform that integrates a micron scale SPP with aluminum nitride (AlN) optical waveguides to create mid-IR vortex beams. The micro-SPP was patterned on the waveguide facet thus it modified the wavefront of light emitted from the waveguide end. The multilevel structure of the micro-SPP was designed by the finite difference time domain (FDTD) method. The structure design, including the phase plate segmentation, was optimized to enable efficient conversion from the waveguide fundamental mode to the LG mode. The far-field intensity profiles of the output vortex beams were evaluated at different mid-IR wavelengths and polarizations. The optical phase map introduced by the micro-SPP explains the obtained HG → LG conversion efficiency as well as its spectral dependence. Thus, we demonstrated that integrated photonics is capable of efficient mid-IR OAM generation through the reconstruction of the waveguide surface.

3.2.2 LG mode analysis

LG modes, like HG modes, can be constructed by a complete basis set of paraxial light beams. HG modes have rectangular symmetry and are typically designated as TEM_{mn} modes. On the other hand, LG modes exhibit a circular symmetric profile around the beam axis and are often denoted as LG_{lp} modes with a radial index p and an azimuthal index l. A beam with Gaussian TEM_{00} mode will gain an additional phase shift of $exp(-iL\Omega)$ after passing through a spiral phase optic, *e.g.* a SPP. Here, L is the topological charge of the SPP. In a cylindrical coordinate system, the complex amplitude of the LG beam propagating along the z-axis has the following form[33,34]:

$$U_{l,p}(r,\Omega,z) = \sqrt{\frac{2p!}{\pi(p+|l|)!}}\frac{1}{W(z)}\left(\frac{\sqrt{2}r}{W(z)}\right)^{|l|} L_p^{|l|}\left(\frac{2r^2}{W^2(z)}\right) exp\left(-\frac{r^2}{W^2(z)}\right)$$

$$\times exp\,[-jkz - jk\frac{r^2}{2R(z)} - jl\Omega - j(l+2p+1)\zeta(z)], \quad (1)$$

with

$$W(Z) = W_0\sqrt{1+(\frac{z}{z_R})^2} \quad (2)$$

$$R(Z) = z\left[1+\left(\frac{z_R}{z}\right)^2\right] \quad (3)$$

$$\zeta(z) = tan^{-1}\frac{z}{z_R} \quad (4)$$

where $W(z)$ is the beam radius to achieve 1/*e* of the Gaussian term with W_0 being the beam waist, k is the wave number, $z_R = \pi W_0^2/\lambda$ is the Rayleigh range, $\zeta(z)$ is the Gaussian beam phase shift, and l is the azimuthal mode number describing the optical phase around the circumference by an integer of 2π. In addition, $(p+1)$ is the radial mode number that defines the number of radial nodes and L_p^l is the generalized Laguerre polynomial. When a TEM_{00} mode passes through a SPP, the output beam is a superposition of LG modes possessing different radial mode numbers *p*. It has been reported that the fundamental radial mode at $p = 0$ is dominant in the output beam [34,35]. Similar to the definition of coupling efficiency during an optical mode conversion [36,37], the overlap integral η is used to evaluate the weighting factor of the fundamental LG_{10} mode in a converted vortex beam:

$$\eta = \left|\frac{\int I_{FDTD}\times I_{LG,10}dxdy}{\int I_{FDTD}\times I_{FDTD}dxdy\cdot\int I_{LG,10}\times I_{LG,10}dxdy}\right|^2 \quad (5)$$

where I_{FDTD} is the far-field intensity distribution of the vortex beam obtained from the FDTD simulation, and $I_{LG,10}$ is the intensity profile of a fundamental LG_{10} mode calculated by equation (1).

3.2.3 The structure design of the mid-IR micro-SPP structures

The structures of the waveguide and the micro-SPP patterned on its facet are illustrated in Figure 3.1 (a). Both the waveguide and the SPP were made by mid-IR transparent AlN. The waveguide had width W and height H, and underneath it was a low refractive index SiO_2 layer. Figure 3.1 (b) shows the micro-SPP structure consisting of eight fan-shaped plates with different thicknesses. The height difference between the tallest and the shortest plates is noted as T. Thus, the height difference between the adjacent layers is T/(N-1), where N is the number of segments of the micro-SPP. On the waveguide facet, the area without the micro-SPP was covered by a thin metal layer. Therefore, for the light reaching the waveguide end, only the portion passing through the micro-SPP was collected in the far field while the rest was blocked by the metal. To create an ideal vortex beam with a topological charge *l*, the optical phase of the micro-SPP should be continuously changing from 0 to $2\pi l$ counter-clockwise along the center of the micro-SPP, as shown in Figure 3.1 (c). However, continuous micro-SPP was not practical in device fabrication. Thus, we adopted a discrete micro-SPP that consisted of N fan-shaped plates where the phase difference between adjacent plates increased by a step of $2\pi l/(N-1)$.

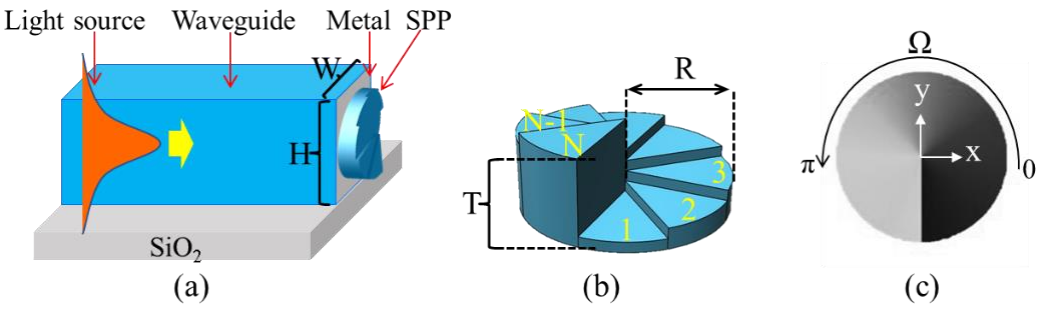

Figure 3.1 (a) The device structure for the FDTD simulation. The AlN waveguide had width W and height H. A micro-SPP was patterned on its end facet. The light source was excited from the left of the waveguide.

(b) The micro-SPP had N staircase-like segments with a radius R and total height difference T. (c) The optical phase map after the light passed through an ideal SPP that had a continuous height change. The total phase change over one turn, from $\Omega = 0^o$ to 360^o, is 2π radian.

In the FDTD simulation, waveguide fundamental TE mode was selected as light sources and this fundamental mode was HG beams with a Gaussian intensity profile. The micro-SPP consisted of 8 fan-shaped segments where the waveguide mode was superimposed on its structure. From the infrared variable angle spectroscopic ellipsometry (IR-VASE), the AlN index is 1.938 at $\lambda = 2.5$ μm and 1.911 at $\lambda = 3.5$ μm indicating that AlN had low optical dispersion and only caused minor effects on the vertex beam generation. In the initial simulation applying to an 8 segment micro-SPP, each plate had an arc of $\pi/4$ radian for $|l|=1$. The optical phase difference between the neighboring plates is $\Delta\varphi$:

$$\Delta\varphi = \frac{2\pi}{\lambda} \times \frac{T}{(N-1)} \times (n - n_0) \quad (6)$$

, where n and n_0 are the refractive indexes of the micro-SPP and the air. In the case at $\lambda = 3.0$ μm, n was 1.93 and n_0 was 1. Thus, T was adjusted to 3.3 μm so that $\Delta\varphi$ reached $2\pi/(8\text{-}1)$. In other words, the total optical phase difference $\Delta\varphi_{total}$, or the phase difference between the tallest and the shortest SPP segments, became 2π to create an ideal vortex beam. In order to achieve vortex beams with higher order topological charge $l > 1$, the total height difference T also needs to be multiplied by l so that the phase difference reaches $2\pi l$.

3.2.4 Dependence on wavelength for vortex beam generation

Figure 3.2 (a) illustrate the FDTD simulated far-field intensity profiles after 1 mm away from a waveguide facet that has an 8-segment micro-SPP patterned on its facet. The dimension of the waveguide was W x H = 20 x 20 μm. A fundamental TE mode was selected to excite the vortex

beam, while the light wavelength was tuned from λ = 2.9 to 3.6 μm to characterize its spectral response. At a shorter wavelength λ = 2.9 μm, the ring profile was not complete. Intensity variation was found at azimuthal angle Ω = 0° and 180° where two gaps appeared along the x axis. These gaps were gradually filled as the wavelength increased. A well-constructed ring with a complete circle was found at λ = 3.1 - 3.3 μm that corresponded to an ideal vortex beam. Nevertheless, the ring profile became nonuniform again after λ = 3.4 μm, where the left portion of the ring became brighter while the right became darker. Hence, we demonstrated that the N = 8 segment micro-SPP was capable of converting the waveguide fundamental mode into an ideal vortex beam within a 200 nm spectral window. Figure 3.2 (b) shows the overlap integral η between the fundamental LG_{10} mode and the far-field vortex beam drawn in Figure 3.2 (a). η was calculated when the beam waist w_0 of the LG_{10} mode was gradually increased from 1 μm to 10 μm at z = 1 mm. The maximum η, denoted as η_{max}, was found at w_0 = 5.3 μm. Figure 3.2 (c) shows the η_{max} calculated at different wavelengths. The largest η_{max} = 97 % was found at λ = 3.3 μm, indicating that the LG_{10} mode was the dominant mode of the generated vortex beam. In addition, the results also confirmed that the micro-SPP can achieve a high conversion efficiency from a fundamental Gaussian beam to a vortex HG mode.

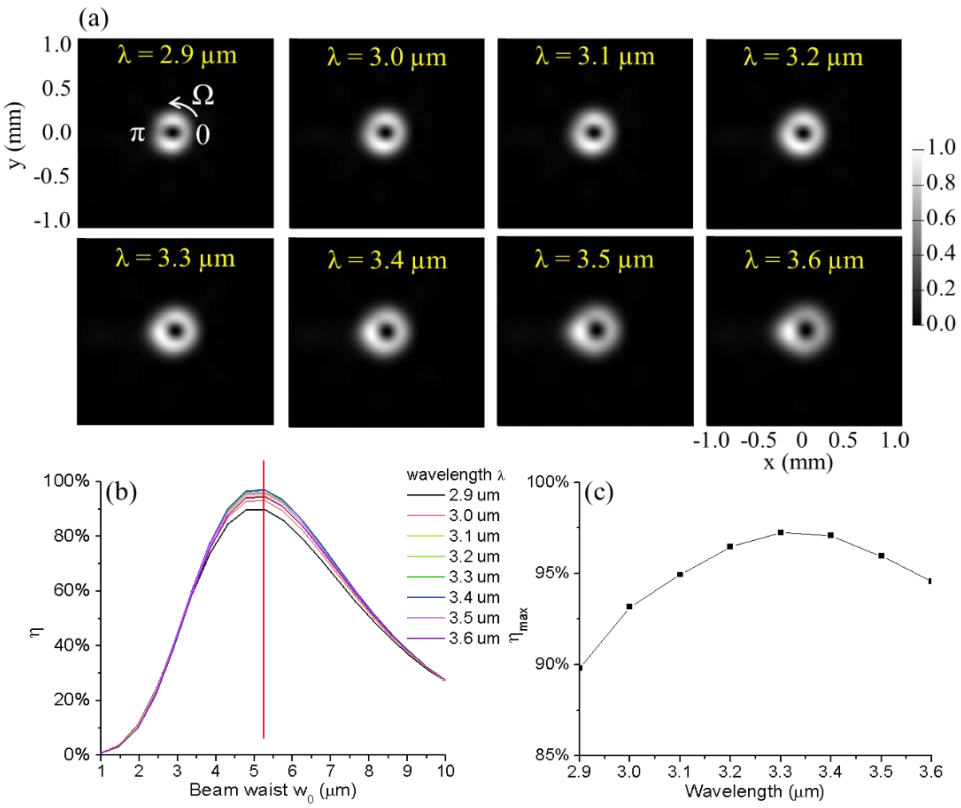

Figure 3.2. (a) The FDTD simulated far-field intensity profiles at z = 1 mm from a waveguide with an N = 8 micro-SPP. The wavelength of the light is tuned consequently from λ = 2.9 to 3.6 μm. Intensity profiles similar to an ideal vortex profile were found at λ = 3.1 - 3.3 μm. (b) The calculated overlap integral η of the LG_{10} mode for the far-field vortex beam created by the micro-SPP. The beam waist w_0 increased from 1 μm to 10 μm and the wavelength was tuned from λ = 2.9 to 3.6 μm. η_{max} was found at w_0= 5.3 μm and is indicated by the red line. (c) The maximum η at different wavelengths. The highest η_{max} = 97 % was found at λ = 3.3 μm.

To explain the observed wavelength dependence during the vortex beam generation, the optical phase maps were calculated in the plane after the micro-SPP. As illustrated in Figure 3.3, annular phase variation was clearly resolved at all wavelengths. Nevertheless, to form an ideal vortex beam, it requires a 2π phase change after completing one circle along the beam center (Ω from 0 to 360°). Figure 3.3 showed that $\Delta\varphi_{total}$ approached 2π as the wavelength shifted to λ = 3.2 μm that consequently created an ideal vortex beam. At λ > 3.4 μm, $\Delta\varphi_{total}$ became less than 2π causing the vortex beam to deform without forming a complete and uniform ring contour.

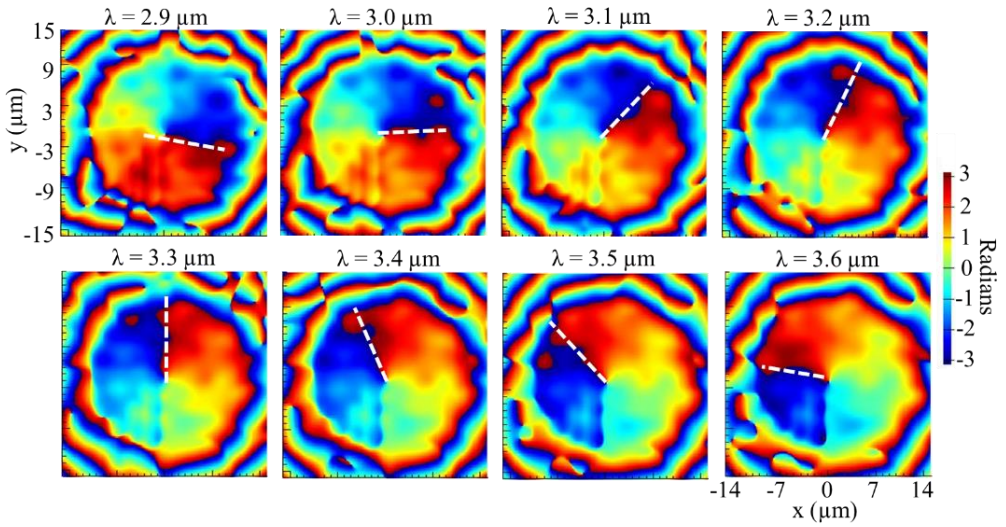

Figure 3.3 The optical phase maps of the E_x field after the waveguide light passed through an R = 10 μm micro-SPP with N = 8 segments. The light wavelength was tuned from λ = 2.9 to 3.6 μm. The white dash lines in the map indicate the reference angle where the optical phase φ was set to zero.

3.2.5 Dependence of segment number N on vortex beam generation

Ideally, the optical phase φ of a micro-SPP should change continuously from 0 to 2π along the azimuthal angle Ω. In practice, it is a challenge to fabricate a continuous micro-SPP using present micro fabrication technology. Thus, a discrete and staircase-like micro-SPP was adopted to create a vortex beam similar to an ideal one[38]. Figure 3.4 (a) show the FDTD simulated far-field intensity profiles projected from the waveguides at z = 1 mm. The waveguide facets were patterned by micro-SPP consisting of 4, 8, 16, 32 or 64 segments, respectively. The light wavelength was fixed at λ = 3.0 μm. At N = 4, only two bright spots were found along the y axis indicating no vortex beam was formed. When N increased to 8, a doughnut-shaped intensity profile was clearly observed indicating that a vortex beam was created. Similar intensity patterns were also found at N = 16, 32, and 64.

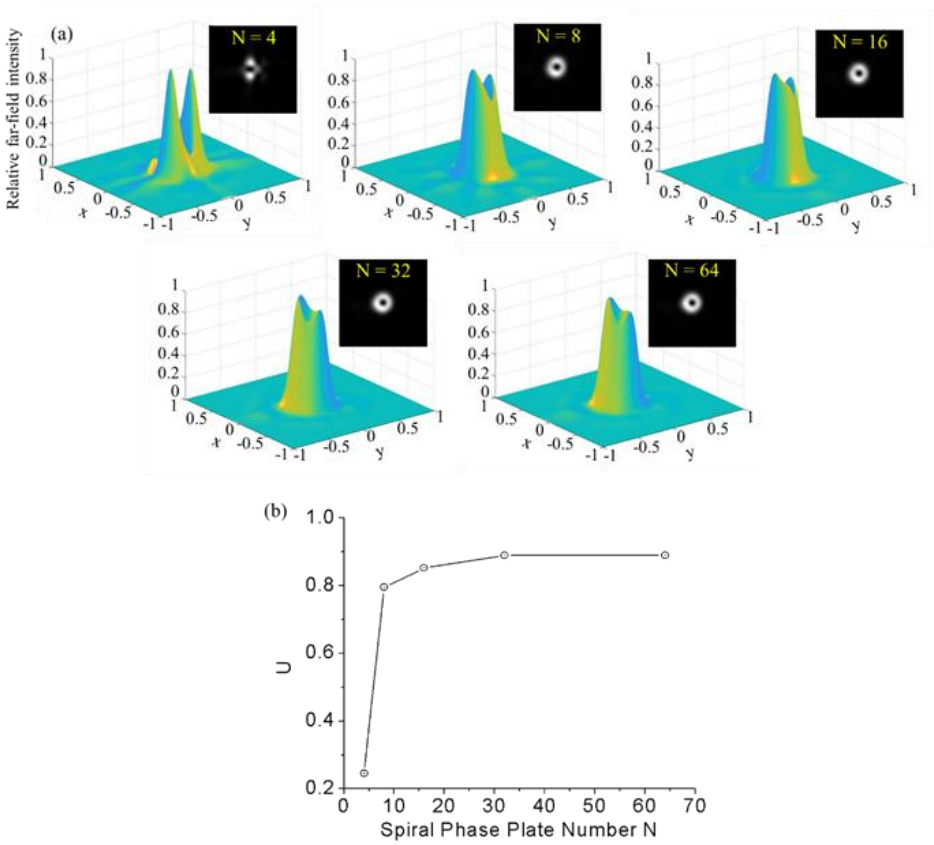

Figure 3.4 The far-field intensity profiles of the vortex beam at z = 1 mm projected from waveguides with their facets patterned by an N segmented micro-SPP. The N increased from 4 to 64. The light wavelength was fixed at λ = 3.0 μm. (b) The intensity uniformity U as the segment number N increased from 4 to 64. U improved from 0.30 to 0.79 as N increased from 4 to 8.

An important factor associated with an ideal vortex beam is the intensity uniformity along the azimuthal angle Ω. Here we define the intensity uniformity U as

$$U = 1 - \frac{I_{max} - I_{min}}{I_{max} + I_{min}} \quad (7)$$

, where I_{max} and I_{min} are the maximum and the minimum intensities obtained along Ω when the radius r was fixed at r_{max} of the maximum intensity. At N = 4, there was a strong intensity variation along Ω thus causing a low uniformity of U = 0.30. On the other hand, at N = 8, the variation significantly reduced and the uniformity improved to U = 0.79. Similarly, by extrapolating the intensity patterns at Figure 3.4 (a), we found U = 0.88, 0.91 and 0.91 at N = 16, 32, and 64 plates,

respectively. Figure 3.4 (b) displays the variation of U as N increased from 4 to 64. U increased sharply from 0.30 to 0.79 when N increased from 4 to 8. This indicates that a micro-SPP made with additional segments created a more uniform vortex beam. Nerveless, we also demonstrated that a micro-SPP utilizing 8 segments was sufficient to convert the majority of the waveguide fundamental mode into an ideal vortex beam.

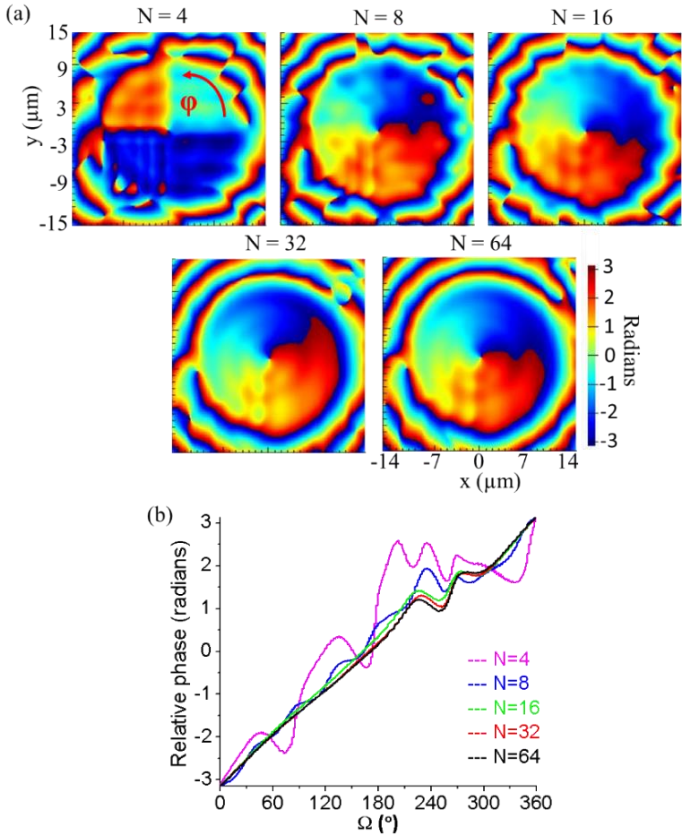

Figure 3.5 (a) The optical phase map of the E_x field for the micro-SPP that have a segment number N of 4, 8, 16, 32, and 64, respectively. Circular phase variation became smoother when more segments were utilized. (b) The optical phase extrapolated from (a). The phase monotonically increased with Ω at $N \geq 8$.

To understand the dependence of segment number N on the vortex beam generation, the optical phase maps from micro-SPP with N = 4 to N = 64 were calculated and drawn in Figure 3.5 (a). Annular phase variation was clearly observed at all N, except at N = 4, where its phase remained

the same at $\Omega = 180^{o} – 360^{o}$. The results explained the high efficiency in vortex irregular spots due to abrupt phase changes were found. Explicit phase variation along Ω at fixed radius of 5 μm is drawn in Figure 3.5 (b). At N = 4, strong non-monotonic phase variation was found as Ω increased. It explains the deficiency in creating an ideal vortex beam when a micro-SPP utilizes only 4 segments. On the other hand, at N = 8, a steady phase increase with Ω was revealed even though some minor phase deviation was found. Once 16 or more segments were utilized, the phase almost linearly increased with Ω with the exception of a trivial variation found at $\Omega = 240^{o}$. Figure 3.6 (a) showed the overlap integration analysis as the plate number N increases. The beam waist was considered between w_0 = 1 μm to 10 μm where the η_{max} was obtained at w_0 = 4.5 - 5.5 μm for each different plate number N. As displayed in Figure 3.6 (b), η_{max} increased sharply from 71 % to 93 % as the plate numbers increased from N = 4 to N = 8. η_{max} > 97 % was achieved at N ≥ 16, indicating that the LG_{10} mode has a high weighting factor for the generated vortex beam. Thus, a discrete micro-SPP was able to construct a phase profile similar to the phase created by a continuous SPP leading to efficient OAM generation.

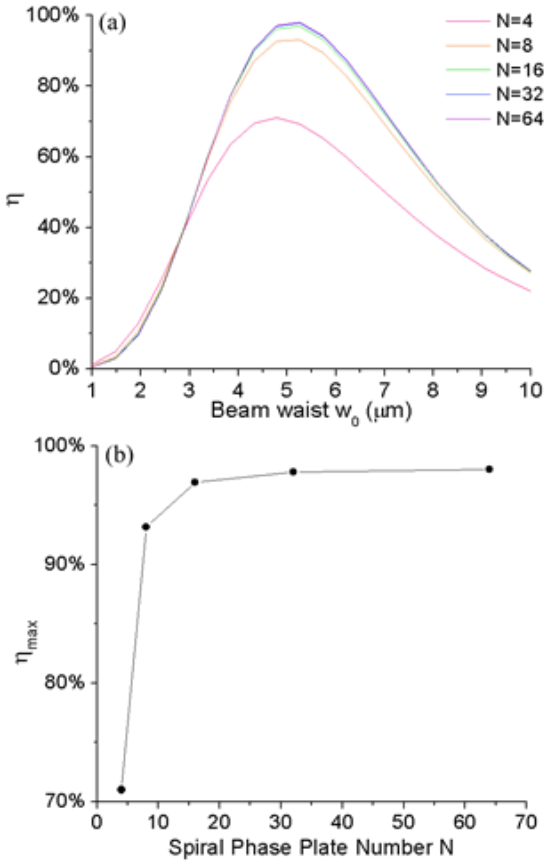

Figure 3.6 The calculated overlap integral η of the LG_{10} mode for the far-field vortex beams as the plate number N increased from 4 to 16. The beam waist w_0 was considered between 1 μm and 10 μm. (b) The maximum η obtained from different N. $\eta_{max} > 97$ % was found at $N \geq 16$.

3.2.6 Conclusions

On-chip vortex beam generation was achieved by reconstructing the mid-IR waveguide facet with N segment micro-SPP. For a micro-SPP with a height T of 3.3 μm and a radius R of 10 μm, an ideal vortex beam was created between λ = 3.1 and 3.3 μm. In addition, the conversion efficiency improved as the segment number N increased. When N increased from 4 to 8, the vortex beams circular uniformity I increased from 0.3 to 0.79 and the LG_{10} became the dominant mode. Hence, our micro-SPP integrated waveguides provided a small footprint platform capable of efficient vortex beam generation.

3.3 FDTD Simulation of mid-IR Vortex Beam Generation Using Gradient Refractive-Index Micro Phase Plates

3.3.1 Motivation

We proposed micro-GRPs integrated with optical fibers to create ideal vortex beams in the optical c band. Vortex beams generation by gradient phase masks has recently demonstrated by using nanostructured glass plates [39,40]. Unlike present SPPs creating a spiral phase profile through different segment heights, GRPs enable the phase difference by defining the material composition of each GRP segment, leading to an adjustment of the refractive index. Thus, GRPs are able to generate helical phase fronts identical to SPPs while preserving a flat facet, which is critical in device integration and also prevents the scattering caused by plate edges in SPPs. The proposed micro-GRPs structure consists of refractive index variable AlON. Their indexes are adjustable from 1.75 of Al_2O_3 to 1.95 of AlN by controlling the composition ratio between the AlN and Al_2O_3[41,42]. In other words, the GRPs become a spiral phase mask because the nitrogen concentrations of the neighboring segments were constantly increased while the oxygen concentrations decreased. The near-field optical phase diagrams and the far-field beam profiles after GRPs were simulated by FDTD to optimize the annular intensity uniformity of the vortex beam. In addition, simulation of higher-order LG beams was also demonstrated from the GRPs on a fiber. The micro-GRPs on a fiber thus provided a small footprint and integrable platform for efficient optical vortices formation.

3.3.2 The design of the micro-GRPs on a fiber

The structures of the fiber and the micro-GRPs patterned on the fiber facet were drawn in Figure 3.7 (a). Figure 3.7 (b) presented the optical phase diagram and the spatial phase variation created by the GRPs. The GRPs create a gradient phase profile along the azimuthal angle on a fiber tip. Because of the azimuthal phase term $e^{i\varphi}$, the fundamental Hermite-Gaussian mode (HG00) with a planar phase can be efficiently converted to the Laguerre-Gaussian modes, i.e., vortex beams, with helical phase fronts. The fiber core had a fixed radius of 15 μm. Meanwhile, the micro-GRPs had a radius *R* and thickness *T*, and consisted of *N*-segments of fan-shaped plates. The refractive indexes of the plates were linearly increased from 1.75 to 1.95. The *n*th plate had an index of $1.75 + 0.2n/(N-1)$, where *N* was the number of segments in the GRPs. The area of the fiber facet without the micro-GRPs was covered by a thin metal layer. Thus, only the light passing through the GRPs was projected to the far field, since the rest of light was blocked by the metal layer. A spiral optical phase diagram was formed due to the difference of the refractive indexes between the plates. To create a vortex beam with an integer number of topological charge *l*, the phase of the beam needed to be annually and monotonically increased from 0 to $2\pi l$. Nevertheless, continuous change of the refractive indexes along the azimuthal angle Ω was not practical in the device design. Alternatively, a step-like refractive-index profile can be created by using the GRPs consisting of *N* fan-shaped plates, where the phase difference between adjacent plates was $2\pi l/(N\text{-}1)$. The design of our micro-GRPs that provide a smooth planar surface and a small feature in micron-scale. Therefore, they have the advantage to directly integrate with other micro-photonic components, like fibers or waveguides, which is difficult to be achieved by other methods, such as computer-generated holograms and spatial light modulators [43-46].

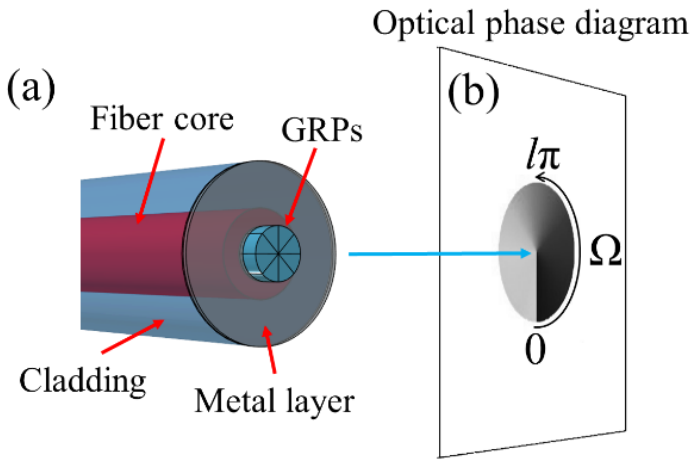

Figure 3.7 (a)The schematic of the fiber structure integrated with micro-GRPs on its facet. The radius of the fiber core is 15 μm. The GRPs had N segments with a radius R and a thickness T. The area on the fiber facet without the micro-GRPs was covered with a thin metal layer. (b)The optical phase of an ideal vortex beam should change continuously from 0 to $2\pi l$ when the azimuthal angle Ω increased from 0° to 360°.

The output far-field pattern for the light passing through the gradient SPPs was simulated using the FDTD method. The perfectly matched layer (PML) absorbing was applied in the boundary condition. In the FDTD simulation, a fundamental TE mode was selected as the fiber light source that had a Gaussian intensity profile as drawn in Figure 3.8 (a). For the *N*-segments micro-GRPs, the optical phase difference between the neighboring plates was obtained by the following equation

$$\Delta\varphi = \frac{2\pi}{\lambda} \times \frac{T}{(N-1)} \times (n_{\max} - n_{\min}) \qquad (1)$$

where n_{max} and n_{min} were the maximum and minimum refractive indexes of the GRPs. In our design, n_{max} and n_{min} were 1.95 and 1.75, corresponding to the refractive indexes of AlN and Al_2O_3. Thus, the GRPs had a total refractive index difference, Δn, of 0.2. To generate a vortex beam at λ = 1.55 μm, the desired thickness *T* of the GRPs was 7.75 × *l* μm so that the Δ*h* reached $2\pi l/(N\text{-}1)$. Consequently, the total optical phase difference $\Delta\varphi_{total}$ became $2\pi l$, which was required to form an ideal vortex beam with topological charge *l*. The structure of the *N* = 8 GRPs was

superimposed on the fiber facet, where its refractive index gradually increased from the 1st to the 8th segments illustrated in Figure 3.8 (b). The refractive index difference between adjacent plates is 0.0286.

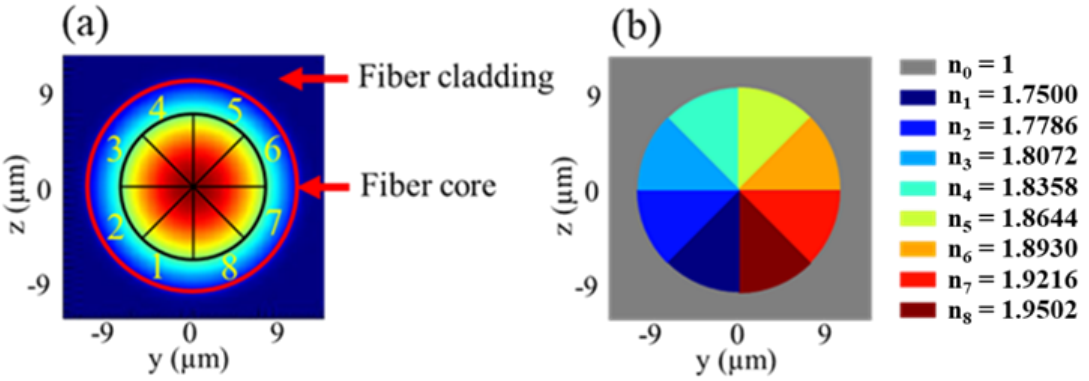

Figure 3.8 (a) The calculated intensity profile of the fundamental TE mode from an optical fiber. The wavelength was at λ = 1.55 μm. The structure of the 8 segment micro-GRPs was superimposed on the mode profile. The numbers 1 to 8 indicated the constituent segments. (b) The refractive index profile of the micro-GRPs where their refractive indexes gradually increased from n_{min} = 1.75 of segment 1 to n_{max} = 1.95 of segment 8.

3.3.3 Thickness dependence on the vortex beam generation

Figure 3.9 (a) - (h) plot the FDTD calculated far-field intensity profiles after the fiber light passed through the micro-GRPs at λ = 1.55 μm. The thickness *T* of the *N* = 8 and *R* = 10 μm GRPs was adjusted from 6.6 to 8.0 μm to improve the annular uniformity of the vortex beam. For *T* = 6.6 μm, the vortex beam was distorted since a spot with higher intensity was found at azimuthal angles Ω between 240° and 330°. When *T* increased from 6.6 to 7.2 μm, the light intensity at Ω = 0° - 240° increased and a near perfect ring profile, close to that of an ideal vortex beam, was achieved. Once *T* increased beyond 7.4 μm, the light intensity at Ω = 60° - 90° and 240° - 270° decreased, and a gap eventually appeared at Ω = 240° - 270° for *T* = 8.0 μm. The forming of the gap was due to the increase of the optical phase as T increased. Therefore, *T* = 7.2 μm was the

optimized thickness for ideal vortex beam generation at λ = 1.55 μm. There was a deviation found from the FDTD resolved thickness T = 7.2 μm and the theoretical value T = 7.75 μm calculated by Eq. (1). This was because the FDTD modeling utilized the effective refractive index from a fiber mode in the vortex beam calculation. On the other hand, Eq. (1) applied the material refractive indexes of AlON without considering the fiber mode. The deviation was also attributed to the difference of the light coupling efficiency from the fiber into each segment, as the refractive index of segments was gradually changed in the micro-GRPs.

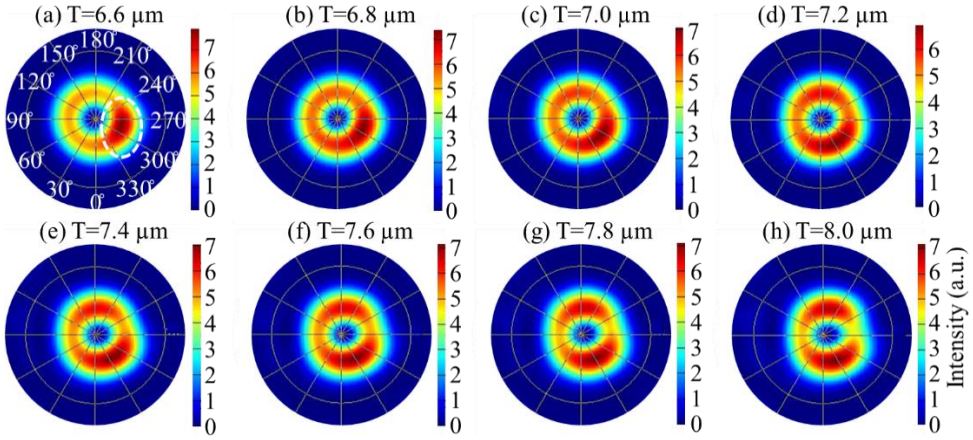

Figure 3.9 The FDTD calculated far-field intensity profiles of the light emitting from the fiber that had N = 8 segment micro-GRPs on its facet. The GRPs had R = 10 μm and the wavelength was at λ = 1.55 μm. (a) – (h) The thickness of the GRPs was swept from T = 6.6 to 8.0 μm to improve the vortex beam profile where an optimized T = 7.2 μm was obtained.

3.3.4 Wavelength dependence on the vortex beam generation

Figure 3.10 (a) - (h) illustrate the far-field intensity profiles after the fiber light passed through the micro-GRPs with N = 8, R = 10 μm, and T = 7.2 μm. The wavelength was swept from λ = 1.25 to 1.95 μm to monitor the variation of the beam profile that had been optimized at λ = 1.55 μm. At the shorter wavelength from λ = 1.25 to 1.45 μm, the light was localized in the upper and lower areas of the ring pattern and gaps were found at Ω = 90° and 270° as shown in Figure 3.10 (a), (b),

and (c). At λ = 1.55 μm, a uniform ring profile similar to an ideal vortex beam was plotted in Figure 3.10 (d). On the other hand, in Figure 4 (e) and (f), the ring became nonuniform at longer wavelengths λ = 1.65 and 1.75 μm, where the light was highly concentrated at Ω = 260° - 300°. Once the wavelength shifted beyond λ= 1.75 μm, as drawn in Figure 3.10 (g) and (h), there was only a bright spot found at Ω = 270° and the ring pattern corresponding to the ideal vortex beam diminished. The deformation of the uniform ring pattern at longer wavelengths was caused by the decreasing of $\Delta\varphi_{total}$.

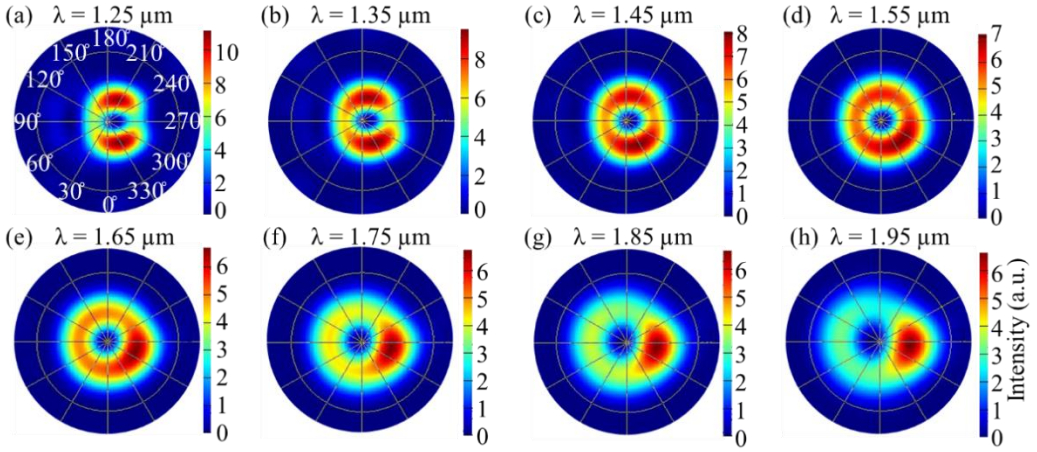

Figure 3.10 The calculated far-field intensity profiles from the micro-GRPs with N = 8, R = 10 μm, and T = 7.2 μm. (a) - (h) The wavelength was tuned from λ = 1.25 to 1.95 μm. Complete and near uniform circular intensity pattern was found at λ = 1.55 μm.

The near-field optical phase maps were calculated in the plane next to the surface of the micro-GRPs to explain the wavelength dependence on the vortex beam generation. Figure 3.11 (a) - (h) illustrate the phase maps between λ = 1.25 and 1.95 μm. Phase fronts with a discrete helical profile were clearly resolved in Figure 5 at all wavelengths. There were eight fan-like phase sections found since only eight plates were utilized in the micro-GRPs. The plots of the phase φ versus the azimuthal angle Ω at R = 5 μm were then extracted and shown in Figure 3.12 (a) - (d). The phase

φ increased monotonically with Ω. To generate an ideal vortex beam at l = 1, the annular phase difference $\Delta\varphi_{total}$ within an azimuthal angle interval of ΔΩ = 360° needed to be 2π. From Figure 3.12 (a) at λ = 1.25 μm, $\Delta\varphi_{total}$ was 2.52π. At λ = 1.55 μm, $\Delta\varphi_{total}$ approached 2π as shown in Figure 3.12 (b), which explained the observed ideal vortex pattern in Fig. 3.10 (d). When the wavelength increased to λ = 1.95 μm, $\Delta\varphi_{total}$ decreased sharply to 1.63π. The insufficient phase difference after λ = 1.55 μm justified the deficiency of vortex pattern formation in Figure 3.11 (f) - (h).

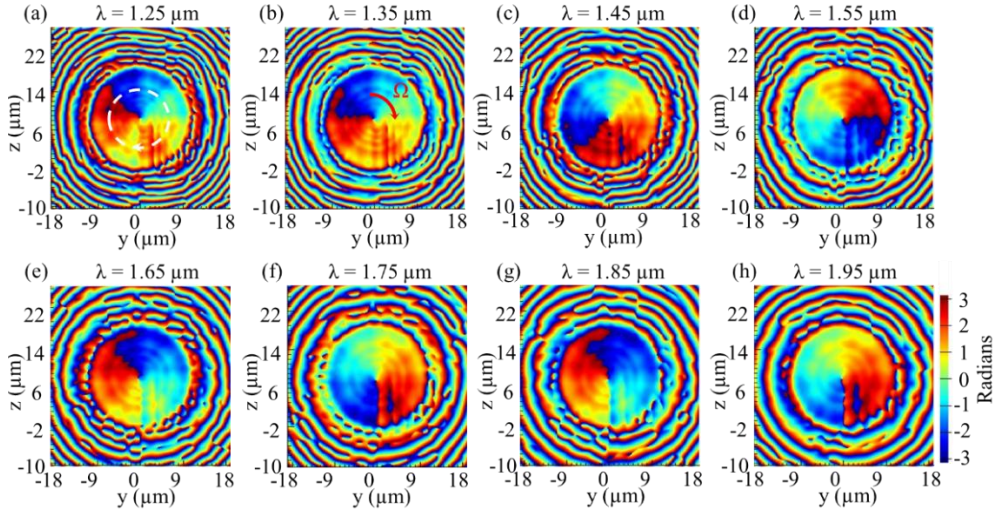

Figure 3.11 The calculated optical phase maps of the Ey field right after the light passed the R = 10 μm and T = 7.2 μm micro-GRPs. (a) – (h) The wavelength was swept from λ =1.25 to 1.95 μm.

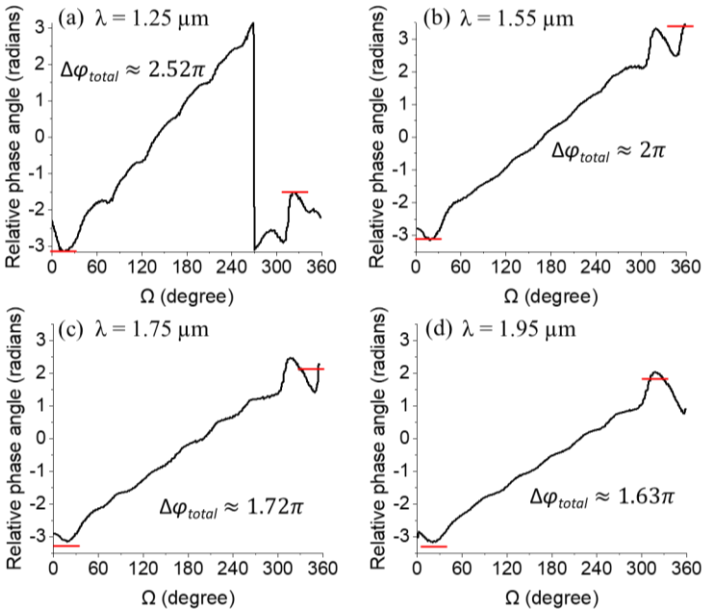

Figure 3.12 The relative optical phase vs Ω extrapolated from figure 5 (a), (d), (f), and (h) along the white dashed circles, which corresponded to λ = 1.25 μm, 1.55 μm, 1.75 μm and 1.95 μm. The annular phase difference $\Delta\varphi_{total}$ at these four wavelengths were 2.52π, 2π, 1.72π and 1.63π, respectively.

3.3.5 Segment number dependence on the vortex beam generation

An ideal GRPs that creates l = 1 vortex beam should have a continuous phase profile, instead of discrete, rising from 0 to 2π as Ω increases from 0° to 360°. Nevertheless, this would require a consistent refractive index change along Ω and an infinite number of segments, which is not practical in the device design. Thus, it is critical to design a micro-GRPs that utilizes finite phase plates while achieving high HG to LG conversion efficiency. Figure 3.13 (a) - (e) show the far-field intensity profiles projected from the micro-GRPs that were assembled by N = 4, 8, 16, 32 and 64 segments, respectively. The radius R was fixed at 10 μm and the wavelength λ was fixed at 1.55 μm. Meanwhile, the thickness T was adjusted separately at different N so the ring patterns at far-field remained the highest annular uniformity. For N = 4, the most evenly distributed intensity was found at T = 6.2 μm. Yet, the circular pattern was not uniform since most light was found at four

spots: Ω = 0°, 90°, 180°, and 270°. When N ≥ 8 segments were utilized, an intensity profile with a more uniform doughnut-shape was found. The optimized thicknesses *T* at *N* = 8, 16, 32 and 64 were 7.2 μm, 7.7 μm, 7.9 μm and 8.0 μm, respectively, as illustrated in Figure 3.13 (f). The obtained vortex beam had almost identical ring pattern when more than 8 segments were utilized. In addition, the optimized *T* slightly increased when additional segments were applied. The *N* = 8 GRPs showed an 89.7% efficiency in converting the fiber fundamental mode to the vortex beam. The efficiency increased to 89.9% at *N* = 16 and 90% at *N* = 32. Our result is better than the conventional spatial light modulator with an efficiency of 44% [47], cylindrical lens method with an efficiency of 75% [48], and transmissive metasurface with an efficiency of 83% [49]. Furthermore, our small footprint GRPs provide a flat top surface that allows further integration with other optical components, which can't be achieved by the micro-SPPs or micro-fabricated wedges with an uneven top surface [50,51].

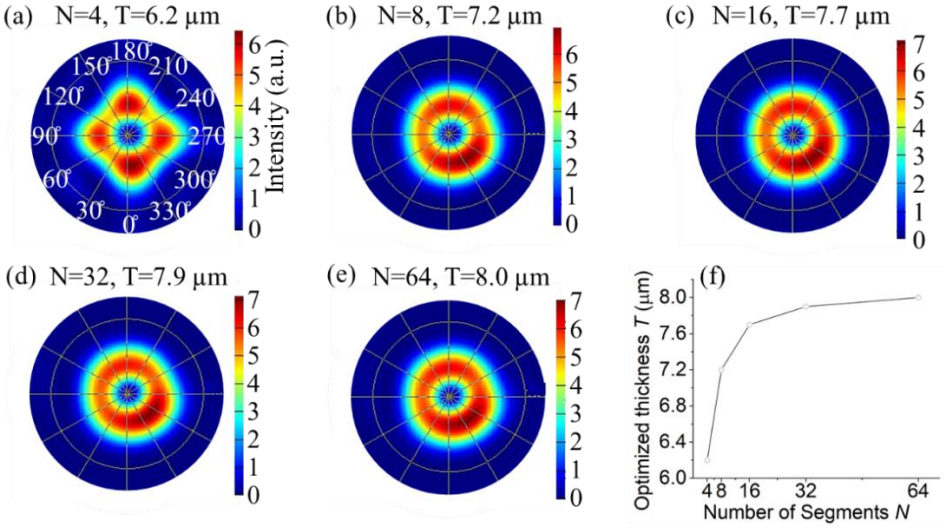

Figure 3.13 The calculated far-field intensity profiles from the *R* = 10 μm micro-GRPs consisting of different number of segments as *N* = (a) 4, (b) 8, (c) 16, (d) 32, and (e) 64, respectively. *T* was optimized for each micro-GRPs to create more uniform vortex beam profile. A sharp and uniform ring pattern was achieved at *N* ≥ 8. (f) The optimized thickness associated with each *N*.

Figure 3.14 shows the optical phase maps of the near-fields corresponding to the intensity patterns shown in figure 3.13 (a) - (e). For GRPs consisting of only 4 plates, the 2D phase map in the near-field is discrete and is clearly separated into 4 sections. The phase variation for the four segment GRPs is not continuously helical thus no ring shape was obtained in the far-field pattern. When 8 segments were used for the GRPs, a near continuous phase change from 0 to 2π was obtained so better uniformity in the far- field pattern was achieved. When use more than 8 segments for the GRPs, the phase maps were not improved as much, and the phase maps for the 32 and 64 segment GRPs are almost identical.

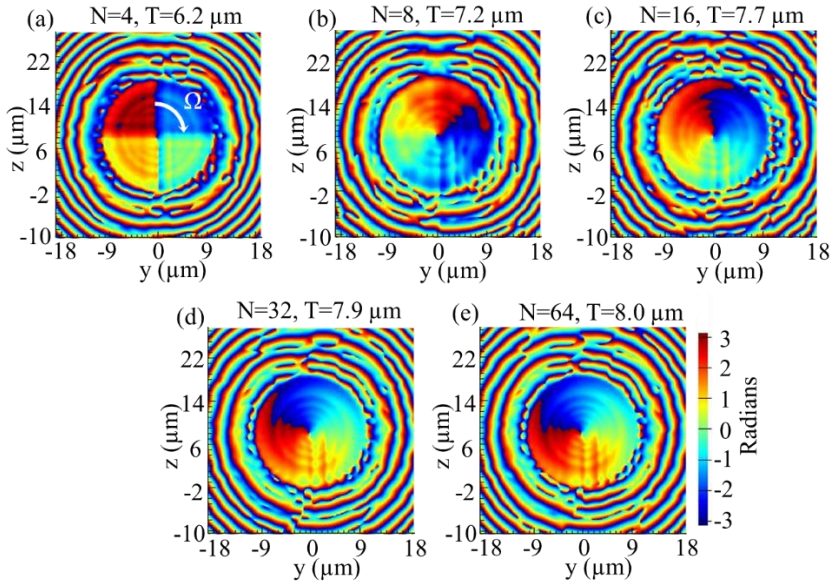

Figure 3.14 The optical phase maps of the Ey field right after the light passed the micro-GRPs with (a) N = 4, T = 6.2 μm; (b) N = 8, T = 7.2 μm; (c) N = 16, T = 7.7 μm; (d) N = 32, T = 7.9 μm, and (e) N = 64, T = 8.0 μm. A consistent phase change was resolved for GRPs at $N \geq 8$.

3.3.6 Higher order vortex beam generation

To generate a higher order $l = 2$ vortex beam, the optical phase of the GRPs needs to increase by 4π from Ω = 0° to 360° According to Eq. (1), the phase change can be achieved by increasing the GRPs thickness while the refractive indexes remain the same. The optimized thickness for l = 1 and N = 32 was T = 7.9 μm according to figure 7 (d). Thus, for l = 2 and N = 32, the micro-GRPs thickness was determined to be T = 15.8 μm. Figure 3.15 (a) displayed the calculated far-field intensity profile where a dark center was found in the projected beam center indicating the formation of the vortex beam. The optical phase maps corresponding to the l = 2 vortex beams are illustrated in Figure 3.15 (b). A 4π phase change was revealed within Ω = 0° and 360°, which was twice of the phase change comparing to the l = 1 phase maps displayed in Figure 3.11. The results validated that the GRPs was able to convert a HG beam to a higher order LG beam efficiently by increasing their thickness.

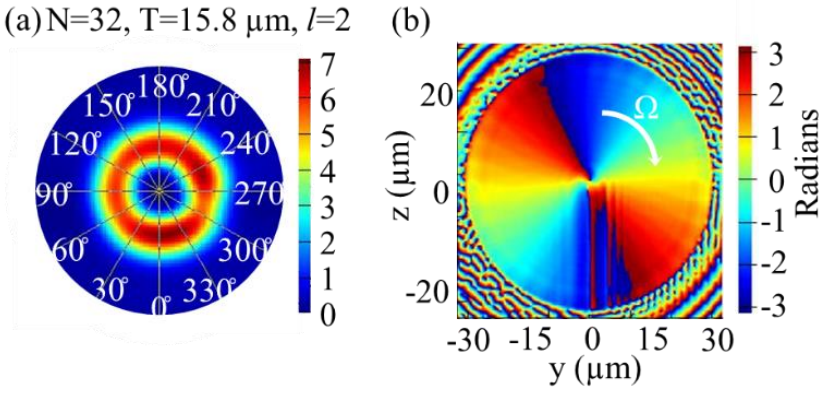

Figure 3.15 (a) The calculated far-field intensity profile for the higher order vortex beams (l = 2) projected from a micro-GRPs at N = 32 and T = 15.8 μm. A ring pattern with a dark central spot was resolved. (b) The optical phase map at l = 2. A 4π phase change was resolved from Ω = 0° to 360°.

3.3.6 Conclusions

Simulation of vortex beams were shown through an optical fiber that had AlON micro-GRPs patterned on its facet. The GRPs created spiral phase profile by varying the AlON refractive index, which was determined by the Al_2O_3 and AlN composition ratio. From spectrum scanning, a uniform $l = 1$ vortex beam was synthesized at $\lambda = 1.55$ μm using $T = 7.2$ μm and $R \geq 10.0$ μm GRPs. An ideal 2π phase change at $\Omega = 0° - 360°$ was observed from the near-field optical phase map. In addition, $N = 8$ segments effectively converted the fiber HG mode to a LG vortex beam. A higher order $l = 2$ vortex beam was achieved by increasing the GRPs thickness to reach 4π optical phase change. The small-footprint and surface-smooth micro-GRPs enables efficient OAM generation, thus becoming a critical component for optical communication requiring large data transmission capacity.

3.4 Mid-IR vortex beam generation by 3D printed spiral phase plates

3.4.1 Motivation

In this study, we fabricated SPP made of mid-IR transparent polymer using 3D patterning method. The 3D patterning method has been utilized to fabricate SPPs in the visible range [52]. However, it is not applied in mid-IR yet. Unlike the planar sub-wavelength components requiring nanoscale fabrication resolution, our SPP can be created by direct laser writing on diacrylate based polymer resins. The developed SPP showed an ideal helical optical phase profile capable of converting a Gaussian-shaped laser beam into a vortex beam. The SPP structure was designed by the 3D FDTD method, where both the near-field phase profiles and the far-field intensity patterns were calculated. The constructed vortex beam was experimentally characterized over a broad mid-IR region to investigate its spectral dependent beam profile.

3.4.2 Fabrication and characterization of the mid-IR SPP

The mid-IR SPP was fabricated using a laser lithography system (Photonic Professional GT2 from Nanoscribe GmbH) with a femtosecond laser at $\lambda = 780$ nm. Figure 3.16 (a) shows the direct laser writing system used to create the polymer SPP. The system utilizes two-photon polymerization (2PP) to create 3D structures with sub-micron hight resolution. The resin is consisting of 60 - 80% 2-(hydroxymethyl)-2-[[(1-oxoallyl)oxy]methyl]-1,3-propanediyl diacrylate [26]. To start with, the substrate was cleaned by acetone and isopropanol and then rinsed with deionized water to remove the organic contamination and to improve the adhesion between the substrate and the sample. Next, a drop of the diacrylate resin was cast onto the top surface of the substrate. The refractive index of the resin is 1.51 before polymerization and 1.53 after polymerization, while the substrate is 1.454. The 3D lithography system was operated in the dip-

in mode, where a 63x immersion objective lens was in direct contact with the resin. The liquid resin was polymerized at the laser focal spot only when the spot intensity was higher than the polymerization threshold. The SPP structure has a diameter of 120 μm and a total height of several microns. The vertical writing resolution, or the step size of vertical stage movement, was chosen to be 200 nm since it is considerable smaller than the total SPP height. After the patterning process, the samplewas developed in propylene glycol monomethyl ether acetate (PGMEA) to remove the uncured resins and then rinsed with isopropanol. Figure 3.16 (b) illustrates the schematic 3D structure of the mid-IR SPP. The segments become thicker counterclockwise around the center axis so the optical phase along the azimuthal angle Ω consistently increases. The dependence between the Ω and the segment thickness, h, is described by the equation $h = \alpha\Omega + h0$, where α is the step thickness per unit azimuthal angle and h0 is the base height of the device. A Gaussian laser beam at wavelength λ is converted to an ideal vortex beam when the segment thickness difference, H, satisfied $H = l\lambda/(n-n0)$ between Ω = 0° and Ω= 360°. Here, n and n0 are the refractive indices of the SPP and the air, respectively, and l is a positive integer defined the topological charge. Nevertheless, it is difficult to fabricate SPP whose thicknesses is constantly increasing with Ω. In practice, discrete SPP with staircase-like structures was utilized. For a discrete SPP consisting of M plates, the thickness of the m^{th} segment, h_m, is defined as following:

$$h_m(\Omega) = h_s \cdot m + h_0 \quad (1)$$

where $2\pi(m-1)/(M-1) < \Omega < 2\pi m/(m-1)$ and $h_s = l\lambda/[(n-n_0) \cdot (M-1)]$ is the height difference between the neighboring segments. When there are sufficient number of segments, the vortex beam created from the staircase-like SPP will be similar to the beam created by a continuous SPP.

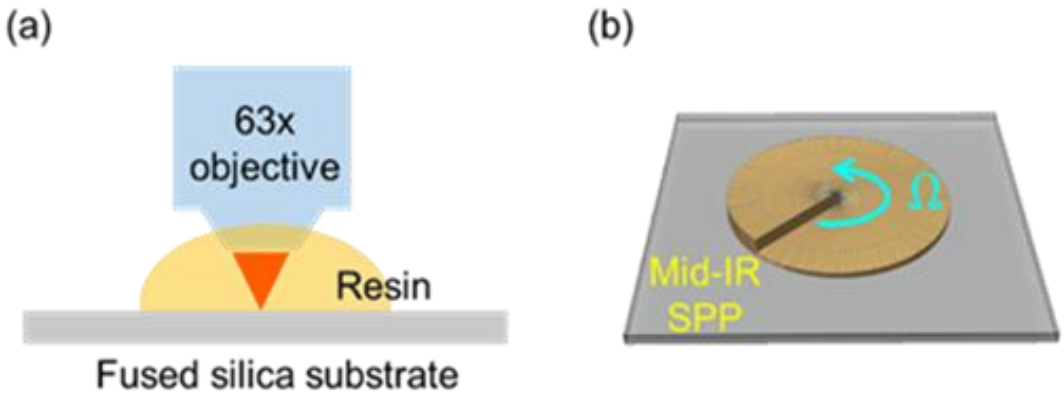

Figure 3.16 (a) Schematic of the mid-IR SPP fabrication by the 3D direct laser writing. (b) The segment becomes thicker counter-clockwise so the optical phase increases along the azimuthal angle Ω.

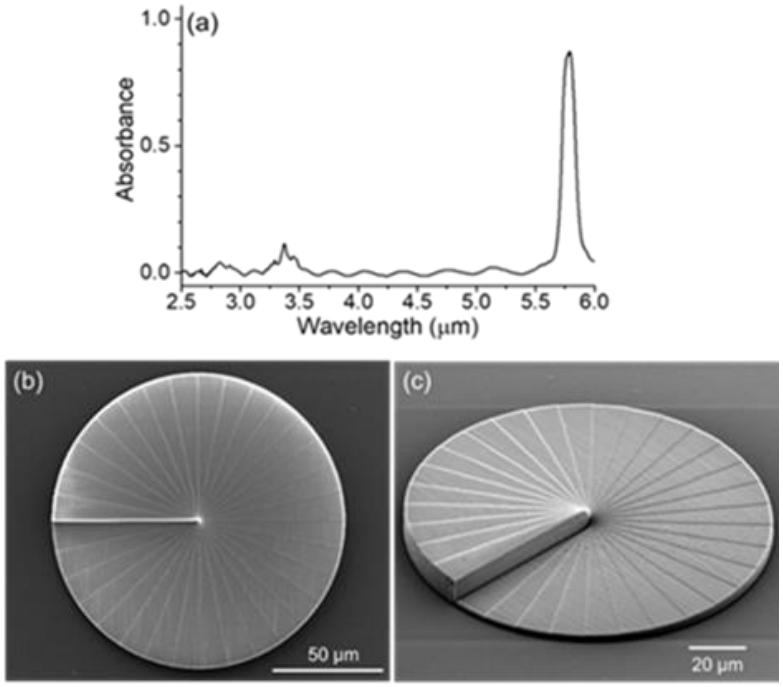

Figure 3.17 (a) The transmission spectrum of the diacrylate polymer film. The film is transparent before λ = 5.5 μm. (b) The top and (c) 52° tilted SEM images of a 32 segments SPP. It has a diameter of 120 μm and a total height difference H of 6.2 μm.

For the infrared absorption measurement, the polymer resin was spin-coated on a double-side polished Si substrate at 3000 rpm and then measured by Fourier transform infrared spectroscopy (FTIR). As shown in Figure 3.17 (a), the polymer film used for SPP patterning is transparent at λ = 2.5 - 5.5 μm with an absorbance less than 0.1. For structure characterization, the fabricated

polymer SPP was coated with a 10 nm thick gold film and then inspected by a scanning electron microscope (SEM). Figure 3.17 (b) and (c) are the SEM images of the SPP captured from the top and at a tilted angle of 52°, respectively. The SPP has a diameter of 120 μm and it is consisted of 32 well defined segments. The segment height increases counterclockwise until it reaches its maximum height difference H of 6.2 μm measured by a stylus profilometer.

3.4.3 FDTD modeling of the mid-IR SPP

The simulation of the vortex beam generation was performed by the 3D FDTD method as illustrated in Figure 3.18 (a). A 32 segments SPP with a diameter of 50 μm was placed next a fiber light source that has a fundamental Gaussian mode profile. An electrical-magnetic (EM) field monitor was placed 1 μm after the SPP to record the intensity and phase information of the transmitted light. The far-field pattern was then calculated by Fourier transform of the collected EM field. The height difference between the first and the last segments, H, is 6.1 μm. The step height between the neighboring segments, h_s, is 190 nm. Considering the refractive index of polymer is 1.54, the wavelength of ideal vortex beam is $\lambda = 3.3$ μm. Figure 3.18 (b) shows the map of calculated near-field optical phase at $\lambda = 3.3$ μm. A helical phase change from $-\pi$ to π was found when Ω increased from 0^o to 360^o, which is a critical to form an ideal a vortex beam. Figure 3.18 (c) - (f) displays the calculated far-field intensity patterns from the SPP at $\lambda = 2.9$, 3.1, 3.3 and 3.5 μm, respectively. Though a dark center corresponding to a vortex beam was found between $\lambda =$ 2.9 and 3.5 μm, the ring pattern changed with the incident light wavelength. At $\lambda = 2.9$ μm, there were bright arcs above and below the beam center. The ring pattern was not completed because the wavelength was away from the ideal $\lambda = 3.3$ μm. On the other hand, a clear ring profile was observed at $\lambda = 3.1$ and 3.3 μm since the azimuthal phase change over a circle approached to 2π.

At λ = 3.5 μm, the ring pattern deformed again and its intensity became ununiformed around the beam center.

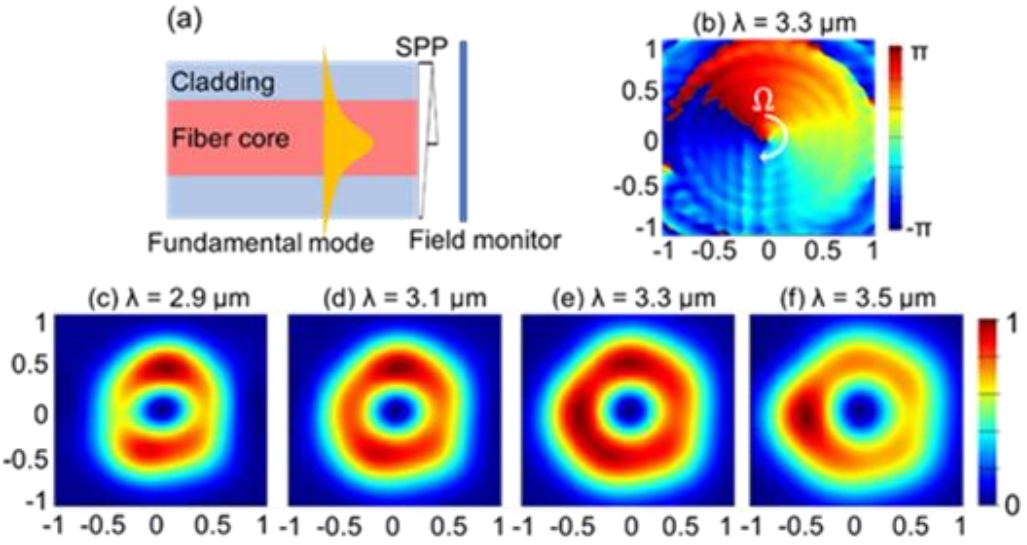

Figure 3.18 (a) The schematic of the FDTD simulation. A SPP was placed next to the fiber facet. After the SPP is a field monitor to calculate the transmitted light intensity and the optical phase. (b) The phase diagram after SPP shows a 2π helical phase change. (c) - (f) The calculated far-field intensity pattern at λ = 2.9, 3.1, 3.3, and 3.5 μm, respectively. A doughnut shape intensity profile indicating a vortex beam was found between λ = 3.1 and 3.3 μm.

3.4.4 Characterization of mid-IR vortex beams

Figure 3.19 (a) is the schematic of the imaging system to characterize the mid-IR vortex beam, and Figure 3.19 (b) illustrates the experimental set-up. The light source is an optical-parametric-oscillator (OPO) pulsed laser (Firefly IR, M-Squared Lasers) with a linewidth of 3 cm^{-1} and a tunable wavelength range from $\lambda = 2.5$ to $\lambda = 3.7$ μm. It has an average output power of 150 mW. The pulse repetition rate is 150 kHz and the pulse duration is 10 ns. The laser beam was first coupled into a single mode fluoride fiber (Thorlabs). The beam from the fiber was first collimated by a mid-IR objective lens and then projected to the 120 μm diameter mid-IR SPP. The light transmitted through the SPP was captured by a 640 x 512 pixels and liquid-nitrogen-cooled InSb IR-camera (IRC800, IRCameras LLC) with a spectral window from $\lambda = 1.0$ to 5.3 μm.

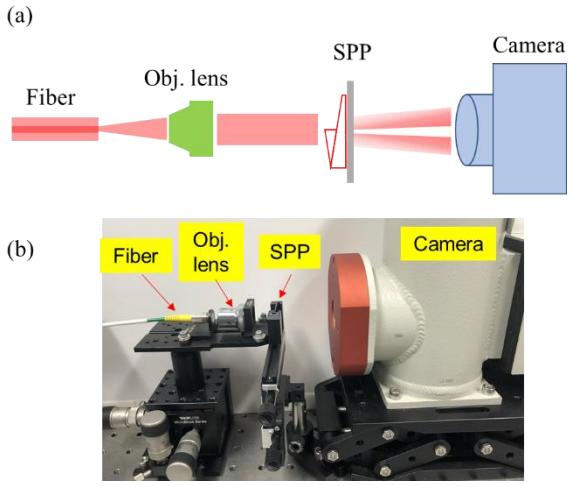

Figure 3.19 (a) The schematic of the imaging system used to characterize the vortex beam created by the mid-IR SPP. (b) The mid-IR light from the fiber passed through the SPP. The vortex beam was imaged by a mid-IR camera.

Figure 3.20 (a)-(e) shows the captured images of vortex beam created by the mid-IR SPP between $\lambda = 2.9$ and 3.7 μm. At $\lambda = 2.9$ μm shown in Figure 3.20 (a), there were two bright speckles above and below the center of the beam. On the other hand, from $\lambda = 3.1$ to 3.3 μm displayed in Figure 3.20 (b) and (c), a bright and uniform circle was gradually formed with a sharp dark spot

in the beam center. The captured doughnut shape profile is similar to the characteristic vortex beam displayed in Figure 3.18 (d) and (e). This is because the azimuthal phase difference over $\Delta\Omega$ = 360° was approaching to 2π at λ = 3.1 - 3.3 μm. As λ increased to 3.7 μm shown in Figure 3.20 (f), the ring pattern became less uniformed and a bright speckle appeared on the left and right of the center dark spot because the azimuthal phase difference deviated from 2π. Figure 3.20 (f) plots the cross-sectional intensity profile of the vortex beam in Figure 3.20 (c). A symmetric pattern was found and there was a strong intensity contrast between the bright rim and the center dark spot, indicating a high efficiency in the formation of mid-IR vortex beam. For comparison, Figure 3.20 (g) shows the cross-sectional intensity profile and the image of the collimated beam from the fiber without passing throught the SPP. A Gaussian shape clearly distinct from the vortex bam was observed.

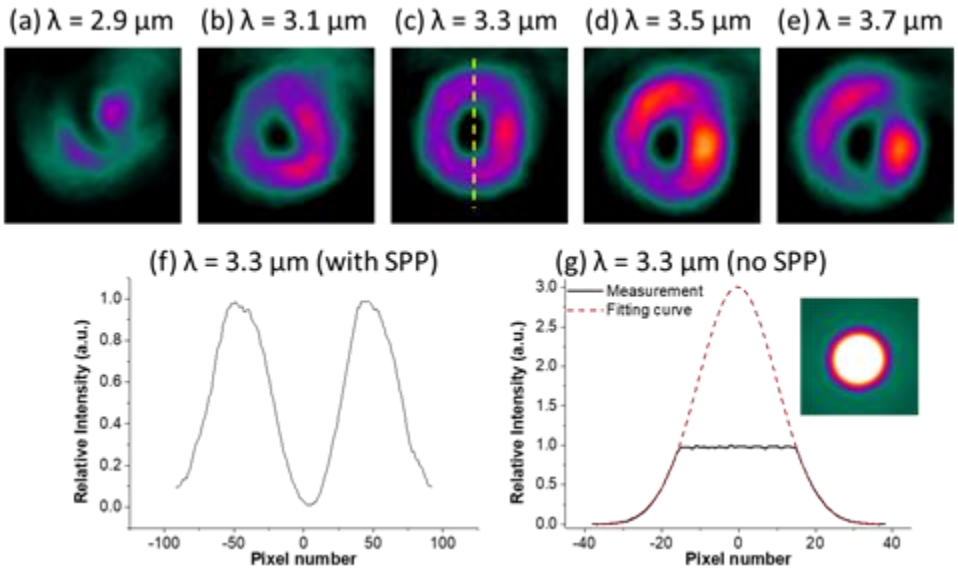

Figure 3.20 The images of the mid-IR vortex beam created by the SPP at λ = (a) 2.9, (b) 3.1, (c) 3.3, (d) 3.5 μm (e) 3.7 μm, respectively. A sharp doughnut shape with a uniform ring was found at λ = 3.3 μm. (f) The cross-sectional intensity profile extracted from (c) shows a high contrast between the centric dark spot and the rim. (g) The intensity profile and image from the collimated beam without SPP.

3.4.5 Conclusions

Mid-IR vortex beams were generated by a polymer SPP through the 3D direct laser writing. The multilayer SPP was formed by a diacrylate based thin resin, which has a broad mid-IR transparency between $\lambda = 2.5$ and 5.5 μm. Applying FDTD modeling, the designed SPP created a gradient optical phase diagram with a helical 2π phase change at $\lambda = 3.1$ - 3.3 μm, thus forming an ideal vortex beam projected in the far-field. Characteristic vortex beams were experimentally observed from a 32 segments mid-IR SPP. The 3D writing platform provides a compact mid-IR OAM component that can accelerate the development of quantum signal processing and high-speed optical datalink.

3.5 References

[1] Darwin C G 1932 Notes on the theory of radiation, in *Proceedings of the Royal Society of London A*, 36-52.

[2] Padgett M J 2002 Orbital angular momentum 25 years on *Optics Express* **25** 11265-74.

[3] Allen L, Beijersbergen M W, Spreeuw R and Woerdman J 1992 Orbital angular momentum of light and the transformation of Laguerre-Gaussian laser modes *Physical Review A* **45** 8185.

[4] Tabosa J and Petrov D 1999 Optical pumping of orbital angular momentum of light in cold cesium atoms *Physical Review Letters* **83** 4967.

[5] Wang J, Yang J-Y, Fazal I M, Ahmed N, Yan Y, Huang H, Ren Y, Yue Y, Dolinar S and Tur M 2012 Terabit free-space data transmission employing orbital angular momentum multiplexing *Nature Photonics* **6** 488.

[6] Bozinovic N, Yue Y, Ren Y, Tur M, Kristensen P, Huang H, Willner A E and Ramachandran S 2013 Terabit-scale orbital angular momentum mode division multiplexing in fibers *Science* **340** 1545-48.

[7] Neshev D N, Alexander T J, Ostrovskaya E A, Kivshar Y S, Martin H, Makasyuk I and Chen Z 2004 Observation of discrete vortex solitons in optically induced photonic lattices *Physical Review Letters* **92** 123903.

[8] Andersen M, Ryu C, Cladé P, Natarajan V, Vaziri A, Helmerson K and Phillips W D 2006 Quantized rotation of atoms from photons with orbital angular momentum *Physical Review Letters* **97** 170406.

[9] Barreiro S and Tabosa J 2003 Generation of light carrying orbital angular momentum via induced coherence grating in cold atoms *Physical Review Letters* **90** 133001.

[10] Mair A, Vaziri A, Weihs G, Zeilinger A 2001 Entanglement of the orbital angular momentum states of photons *Nature* **412** 313-316.

[11] He H, Friese M E J, Heckenberg N R, Rubinsztein-Dunlop H 1995 Direct observation of transfer of angular momentum to absorptive particles from a laser beam with a phase singularity *Physical Review Letters* **75** 826-829.

[12] Grier D G 2003 A revolution in optical manipulation Nature **424** 810-816.

[13] Mazilu M, Baumgartl J, Čižmár T, Dholakia K 2009 Accelerating vortices in Airy beams Proc. SPIE 7430, Laser Beam Shaping X, 74300C.

[14] X Chu 2002 Propagation of an Airy beam with a spiral phase *Optics Letters* **37** 5202-04.

[15] Y Zhang, X Liu, M R Belić, W Zhong, F Wen and Y Zhang 2002 Anharmonic propagation of two-dimensional beams carrying orbital angular momentum in a harmonic potential *Optics Letters* **40** 3786-89.

[16] Z-X Fang, Y Chen, Y-X Ren, L Gong, R-D Lu, A-Q Zhang, H-Z Zhao and P Wang 2002 Interplay between topological phase and self-acceleration in a vortex symmetric Airy beam *Optics Express* **26** 7324-35.

[17] Karimi E, Schulz S A, De Leon I, Qassim H, Upham J and Boyd R W 2014 Generating optical orbital angular momentum at visible wavelengths using a plasmonic metasurface *Light: Science & Applications* **3** e167.

[18] Simpson N, Dholakia K, Allen L and Padgett M 1997 Mechanical equivalence of spin and orbital angular momentum of light: an optical spanner *Optics Letters* **22** 52-54.

[19] Yan Y, Xie G, Lavery M P, Huang H, Ahmed N, Bao C, Ren Y, Cao Y, Li L and Zhao Z 2014 High-capacity millimetre-wave communications with orbital angular momentum multiplexing *Nature Communications* **5** 4876.

[20] Capasso F, Paiella R, Martini R, Colombelli R, Gmachl C, Myers T L, Taubman M S, Williams R M, Bethea C G and Unterrainer K 2002 Quantum cascade lasers: ultrahigh-speed operation, optical wireless communication, narrow linewidth, and far-infrared emission *IEEE Journal of Quantum Electronics* **38** 511-32.

[21] Jin T, Li L, Zhang B, Lin H-Y G, Wang H and P T Lin 2017 Monolithic mid-infrared integrated photonics using silicon-on-epitaxial barium titanate thin films *ACS Applied Materials & Interfaces* **9** 21848-55.

[22] Lin P T, Jung H, Kimerling L C, Agarwal A and Tang H X 2014 Low-loss aluminium nitride thin film for mid-infrared microphotonics *Laser & Photonics Reviews* **8** L23-L28.

[23] Lin P T, Lin H Y G, Han Z, Jin T, Millender R, Kimerling L C and Agarwal A 2016 Label-Free Glucose Sensing Using Chip-Scale Mid-Infrared Integrated Photonics *Advanced Optical Materials* **4** 1755-59.

[24] P T Lin, S W Kwok, H-Y G Lin, V Singh, L C Kimerling, G M Whitesides and A Agarwal 2014 Mid-infrared spectrometer using opto-nanofluidic slot-waveguide for label-free on-chip chemical sensing *Nano Letters* **14** 231-38.

[25] Farrah D, Bernard-Salas J, Spoon H W W, Soifer B T, Armus L, Brandl B, Charmandaris V, Desai V, Higdon S, Devost D and Houck J 2007 High-resolution mid-infrared spectroscopy of ultraluminous infrared galaxies *The Astrophysical Journal* **667**, 149-169.

[26] Christensen P R, Jakosky B M, Kieffer H H, Malin M C, McSween H Y, Nealson K, Mehall G L, Silverman S H, Ferry S and Caplinger M 2004 The thermal emission imaging system (THEMIS) for the Mars 2001 Odyssey Mission *Space Science Reviews* **110** 85-130.

[27] Beijersbergen M W, Allen L, Van der Veen H and Woerdman J 1993 Astigmatic laser mode converters and transfer of orbital angular momentum *Optics Communications* **96** 123-32.

[28] Thirugnanasambandam M, Senatsky Y and Ueda K 2010 Generation of very-high order Laguerre-Gaussian modes in Yb: YAG ceramic laser *Laser Physics Letters* **7** 637-43.

[29] Ito A, Kozawa Y and Sato S 2010 Generation of hollow scalar and vector beams using a spot-defect mirror *JOSA A* **27** 2072-77.

[30] Kim J and Clarkson W 2013 Selective generation of Laguerre–Gaussian (LG0n) mode output in a diode-laser pumped Nd: YAG laser *Optics Communications* **296** 109-12.

[31] Ostrovsky A S, Rickenstorff-Parrao C and Arrizón V 2013 Generation of the "perfect" optical vortex using a liquid-crystal spatial light modulator *Optics Letters* **38** 534-36.

[32] Heckenberg N, McDuff R, Smith C and White A 1992 Generation of optical phase singularities by computer-generated holograms *Optics Letters* **17** 221-23.

[33] Yao A M and Padgett M J 2011 Orbital angular momentum: origins, behavior and applications Advances in Optics and Photonics 3 161-204.

[34] Longman A and Fedosejevs R 2017 Mode conversion efficiency to Laguerre-Gaussian OAM modes using spiral phase optics Optics Express 25 17382-92.

[35] Sephton B, Dudley A and Forbes A 2016 Revealing the radial modes in vortex beams Applied Optics 55 7830-35.

[36] Demchenko Y A, Bilenko I and Gorodetsky M L 2017 Optimisation of the prism coupling of optical whispering-gallery-mode microcavities Quantum Electronics 47 743.

[37] Flueraru C and Grover C P 2003 Overlap integral analysis for second-harmonic generation within inverted waveguide using mode dispersion phase match IEEE Photonics Technolgy Letters 15 697-699.

[38] Oemrawsingh S S R, Van Houwelingen J A W, Eliel E R, Woerdman J P, Verstegen E J K, Kloosterboer J G and't. Hooft G W 2004 Production and characterization of spiral phase plates for optical wavelengths Applied Optics 43 688-694.

[39] K. Switkowski, A. Anuszkiewicz, A. Filipkowski, D. Pysz, R. Stepien, W. Krolikowski, and R. Buczynski, "Formation of optical vortices with all-glass nanostructured gradient index masks," *Opt. Express* 25, 31443-31450 (2017).

[40] H. T. Nguyen, A. Anuszkiewicz, J. Lisowska, A. Filipkowski, R. Kasztelanic, R. Buczynski, and W. Krolikowski, "Numerical analysis of optical vortices generation with nanostructured phase masks," *Opt. Express* 28, 21143-21154 (2020).

[41] T. Sakai, "Hot-pressing of the AlN-Al2O3 system," *J. Ceram. Assoc. Japan* **86**(991), 125-130 (1978).

[42] N. D. Corbin, “Aluminum oxynitride spinel: a review,” *J. Euro. Ceram. Soc.* **5**(3), 143-154 (1989).

[43] A. V. Carpentier, H. Michinel, J. R. Salgueiro, and D. Olivieri, "Making optical vortices with computer-generated holograms," Am. J. Phys. 76, 916-921 (2008).

[44] S. Li, and Z. Wang, "Generation of optical vortex based on computer-generated holographic gratings by photolithography," Appl. Phys. Lett. 103, 141110 (2013).

[45] J. M. Andersen, S. N. Alperin, A. A. Voitiv, W. G. Holtzmann, J. T. Gopinath, and M. E. Siemens, "Characterizing vortex beams from a spatial light modulator with collinear phase-shifting holography," Appl. Opt. 58, 404-409 (2019).

[46] T. W. Clark, R. F. Offer, S. Franke-Arnold, A. S. Arnold, and N. Radwell, “Comparison of beam generation techniques using a phase only spatial light modulator,” Opt. Express 24, 6249–6264 (2016).

[47] M.-Q. Cai, Z.-X. Wang, J. Liang, Y.-K. Wang, X.-Z. Gao, Y. Li, C. Tu, and H.-T. Wang, "High-efficiency and flexible generation of vector vortex optical fields by a reflective phase-only spatial light modulator," Appl. Opt. 56, 6175-6180 (2017).

[48] V. G. Shvedov, C. Hnatovsky, W. Krolikowski, and A. V. Rode, "Efficient beam converter for the generation of high-power femtosecond vortices," Opt. Lett. 35, 2660-2662 (2010).

[49] S. Tang, X. Li, W. Pan, J. Zhou, T. Jiang, and F. Ding, "High-efficiency broadband vortex beam generator based on transmissive metasurface," Opt. Express 27, 4281-4291 (2019).

[50] Z.-Y. Hu, Z.-N. Tian, J.-G. Hua, Q.-D. Chen, and H.-B. Sun, "Axially controllable multiple orbital angular momentum beam generator," Appl. Phys. Lett. 117, 021101 (2020).

[51] E. Brasselet, M. Malinauskas, A. Žukauskas, and S. Juodkazis, "Photopolymerized microscopic vortex beam generators: Precise delivery of optical orbital angular momentum," Appl. Phys. Lett., vol. 97, no. 21, p. 211108, Nov. 2010.

[52] X.-C. Yuan, B. Ahluwalia, S. Tao, W. Cheong, L. Zhang, J. Lin, J. Bu, and R. Burge, "Wavelength-scalable micro-fabricated wedge for generation of optical vortex beam in optical manipulation," Appl. Phys. B 86, 209-213 (2007).

CHAPTER IV

MID-IR NONLINEAR LIGHT GENERATION OF $BATIO_3$ THIN FILMS TOWARDS ON-CHIP LIGHT SOURCES*

4.1 Introduction

Complex metal oxides including $LiNbO_3$, $LaTiO_3$, and $BaTiO_3$ with a perovskite crystal structure is critical in nonlinear photonics because of their large second order optical nonlinearity. The ferroelectricity and the optical nonlinearity of perovskite oxides are attributed to their non-centrosymmetric structure and transition-metal B cations [1]. The nonlinear response from the spontaneous dipole moment within a perovskite unit cell can result in photons that carry an energy different from the exciting laser.

The general form of the polarization *P*, induced by external electric fields, is given by

$$P = \epsilon_0\left(\chi^{(1)}E + \chi^{(2)}E^2 + \chi^{(3)}E^3 + \cdots\right)$$

where $\chi^{(2)}$, $\chi^{(3)}$…. Are the higher-order nonlinear susceptibility. Since the higher-order nonlinear susceptibility is small, high optical intensities are required for generation of such optical nonlinear process with observable intensity. For the second-order nonlinear process, the nonlinear polarization is given by

$$P^{(2)} = \epsilon_0\chi^{(2)}E^2$$

where the second-order nonlinear susceptibility, $\chi^{(2)} = \chi^{(2)}_{ijk}$, is a tensor of rand 3. The indices *i*, *j*, *k* refer to the Cartesian components of the field and represent the polarization directions. If we consider an optical field consisting of two distinct frequency components, ω_1 and ω_2, represented by

* Reprinted with permission from "Mid-infrared frequency doubling using strip-loaded silicon nitride on epitaxial barium titanate thin film waveguides." By Junchao Zhou, Mingzhao Liu, Ming Lu, and Pao-Tai Lin, 2020. *Optics Letters* 45, no. 23, 6358-6361, Copyright @ 2020 Optica Publishing Group.

$$E(t) = E_1(t)e^{-i\omega_1 t} + E_2(t)e^{-i\omega_2 t} + c.c.$$

When the above electric field is incident upon a nonlinear medium, the second-order nonlinear polarization is induced with the form of

$$P^{(2)} = \epsilon_0\chi^{(2)}\left[E_1^2e^{-2i\omega_1 t} + E_2^2e^{-2i\omega_2 t} + 2E_1E_2e^{-i(\omega_1+\omega_2)t} + 2E_1E_2^*e^{-i(\omega_1-\omega_2)t} + c.c\right]E^2$$
$$+ 2\epsilon_0\chi^{(2)}[E_1E_1^* + E_2E_2^*]$$

By mixing or splitting the energies from the incoming photons, coherent light wave with specific wavelengths is created through various mechanisms, such as SHG, sum- frequency generation (SFG) and difference- frequency generation (DFG) corresponding to the terms on the right-hand-side of the above equation. Bulk perovskite oxide single crystals have been utilized in various nonlinear photonic systems, including $LiNbO_3$ and $LaTiO_3$ based OPO and optical parametric amplification (OPA) [2,3]. Applying quasi-phase matching on these perovskite oxide crystals, nonlinear frequency conversion becomes more efficient and provides coherent light sources over a broad spectrum [4-6]. In addition, the nonlinear optical method can generate entangled a photon-pair through parametric down-conversion, which is critical for the development of quantum communication and networking [7,8].

Nevertheless, compact devices desire perovskite oxides thin films over conventional bulk crystals for numerous chip-scale applications, such as electro-optic modulators [9], gas sensors [10], and non-volatile memory devices [11]. Deposition methods like atomic layer deposition (ALD), molecule-beam epitaxy (MBE), and chemical vapor deposition (CVD) have been explored to grow crystalline perovskite oxide thin films [12-15]. Among various candidates of nonlinear optical thin films, BTO has received significant attention for the applications in the integrated photonic circuits. BTO has the advantages of wide spectral transparency [16,17], strong Pockels effect [18,19], and high second-order optical nonlinearity [20]. To monolithically integrate BTO

with present Si photonics, growth of epitaxial BTO thin films on Si substrates has been investigated through different deposition techniques [21,22]. For instance, thin TiN and MgO buffer layers were applied to reduce the large lattice mismatch between the BTO and the Si to enable monolithic BTO-on-Si platforms [23,24].

4.2 Mid-IR pumped second harmonic generation using barium titanate thin films

4.2.1 Epitaxial BTO thin film growth and XRD characterization

The BTO thin film was deposited onto a single-crystal STO (001) substrate by PLD at 600°C and 20 mTorr of O_2. The PLD used a KrF excimer laser (λ = 248 nm) with a fluence of 1.5 J/cm^2 and a repetition rate of 5 Hz. The BTO target was prepared by a conventional ceramic sintering method. The crystalline structure of the BTO thin film was characterized by x-ray diffraction (XRD). From the θ-2θ scan in Figure 4.1 (a), only BTO (00*l*) was found, indicating that the BTO thin film is a single crystalline film and mainly grew along the (00*l*) direction. The φ scans of BTO (113) and STO (113) in Figure 4.1 (b) indicate that the BTO thin film exhibited cube-on-cube growth on the STO substrate without experiencing in-plane rotations.

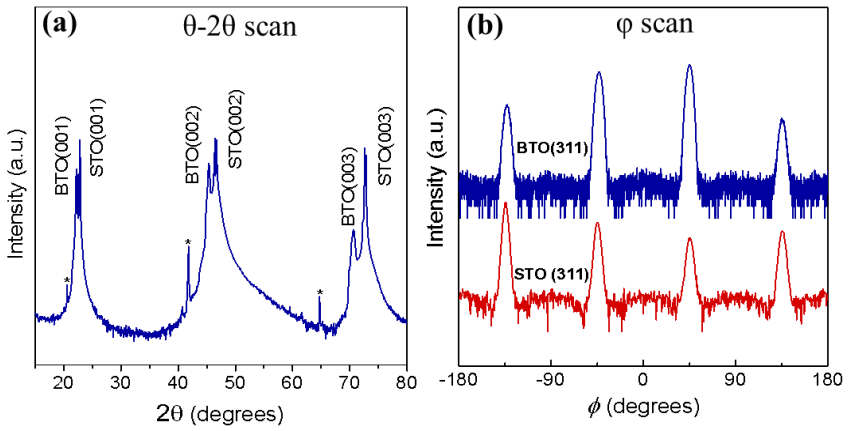

Figure 4.1 The XRD results of the BTO thin film deposited on the (001) STO substrate by PLD. (a) A θ-2θ scan of the BTO thin film. The BTO was epitaxially grown along the (00*l*) direction. (b) A φ scan of the BTO thin film indicated a cube-on-cube growth on the STO substrate.

4.2.2 Modeling of the Mid-IR SHG from BTO thin films

A BTO crystal possesses different crystal symmetries at different temperatures due to its phase transitions. Upon increasing the temperature, the phase of the BTO crystal changes sequentially from rhombohedral to orthorhombic, tetragonal (at 0 - 120 ^{o}C), and paraelectric cubic phase. The space group of tetragonal BTO is P4mm and its unit cell is slightly elongated along the c-direction, which is the fourfold axis as shown in Figure 4.2 (a). The distance from the center Ti atom to the O atoms along the c-axis can be greater or smaller than the other O atoms along the a-axis, leading to a spontaneous polarization P_s parallel to the c-axis.[35] For an epitaxial BTO thin film, the coordinate axes were defined by the crystal axes of the STO substrate. As shown in Figure 4.2 (b), the [001], [100], and [010] axes of the STO are defined as the $+\vec{X}$, $+\vec{Y}$, and $+\vec{Z}$ axes, respectively. A BTO thin film can have six different ferroelectric domain variants with their polarizations parallel to the $+\vec{X}$, $-\vec{X}$, $+\vec{Y}$, $-\vec{Y}$, $+\vec{Z}$, and $-\vec{Z}$ directions, which are labeled as the *X*+, *X*-, *Y*+, *Y*-, *Z*+, and *Z*- domains, respectively. To study the polarimetric SHG, Figure 3 illustrates that the **x**, **y**, and **z** axes of the lab coordination are initially aligned to the $+\vec{X}$, $+\vec{Y}$, and $+\vec{Z}$ axes defined by the crystal coordination of the STO substrate.[36] In other words, a light beam E^{ω} propagating along the **x**-axis is normally incident to the (001) surface of the STO substrate and its polarization is in the **y**-**z** plane. At azimuth φ = 0, the polarization direction is coincident with the **y**-axis. To analyze the polarimetric SHG from a multi-domain BTO thin film, a polarizer was placed before the photodetector to differentiate the **y** and **z** polarized SHG signals, where the intensities are denoted

as $I_y^{2\omega}$ and $I_z^{2\omega}$, respectively. For E^{ω} propagating in the **x**-direction, the *X*+ and *X*- domain variants will not create an SHG polarized in the **y**-**z** plane.

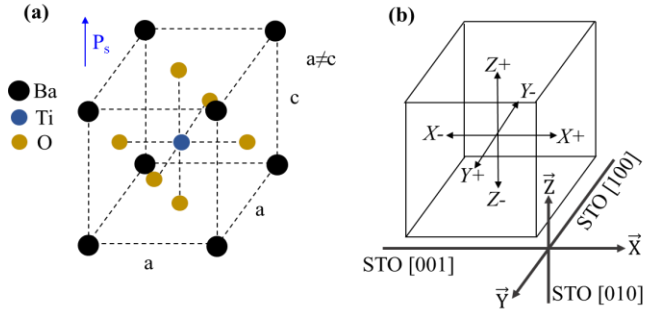

Figure 4.2 (a) The structure of a tetragonal BTO unit cell with one Ti atom in the cell center, eight Ba atoms in the corners, and six O atoms in the center of the facets. (b) The six possible ferroelectric domain variants, *X*+, *X*-, *Y*+, *Y*-, *Z*+, and *Z*-, in the +$\vec{X}$, +$\vec{Y}$, and +$\vec{Z}$ lab-based coordinate system.

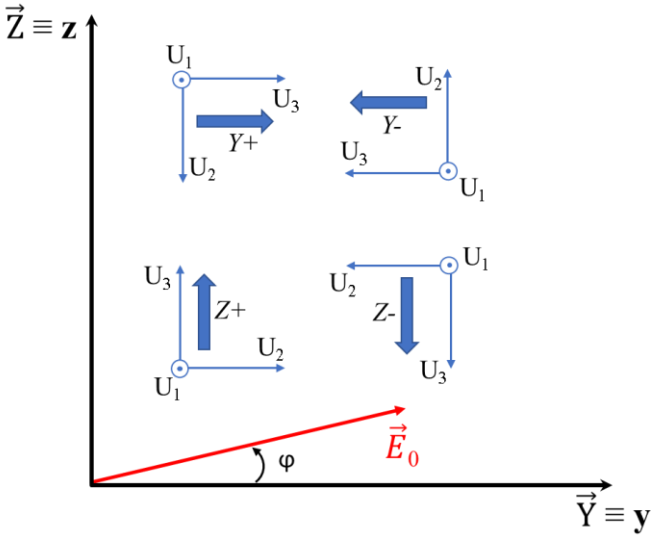

Figure 4.3 The four possible domain variants in the **y**-**z** plane, *Y*+, *Y*-, *Z*+, and *Z*-, and the crystal axes (U_1, U_2, U_3) associated with each of the four domain variants. The incident light $\vec{E}_0$ is linearly polarized and the azimuthal angle between the incident light and the **y**-axis is noted as φ.

The SHG collected from a multi-domain BTO thin film was considered as a combination of the SHG signals attributed by each domain variant. To use the nonlinear optical tensor matrix, the components of the incident electric field (E_x, E_y, E_z) were transformed and interpreted by the

orthogonal crystal coordination (U_1, U_2, U_3) corresponding to each domain variant. Here, the optic axis of the crystal U_3 is parallel to the direction of P_s and equivalent to the c-axis indicated in Figure 4.2 (a). Figure 4.3 displays the new coordinations (U_1, U_2, U_3) and the P_s direction associated with the *Y*+, *Y*-, *Z*+, and *Z*- domain variants, separately. The second order nonlinear polarization for the tetragonal BTO is then described as

$$P_s = \begin{pmatrix} P_1 \\ P_2 \\ P_3 \end{pmatrix} = \begin{pmatrix} 0 & 0 & 0 & 0 & d_{15} & 0 \\ 0 & 0 & 0 & d_{15} & 0 & 0 \\ d_{31} & d_{31} & d_{33} & 0 & 0 & 0 \end{pmatrix} \begin{pmatrix} E_1^2 \\ E_2^2 \\ E_3^2 \\ 2E_2E_3 \\ 2E_1E_3 \\ 2E_1E_2 \end{pmatrix}. \quad \textbf{(1)}$$

E_1, E_2, and E_3 are the components of the electrical fields along the U_1, U_2, and U_3 axes, and d_{ij} is the tensor element of the 2nd order optical nonlinear coefficients. The electric field of the light propagating along the **x**-direction has $E_x = 0$, $E_y = E_0 \cos\varphi$, and $E_z = E_0 \sin\varphi$. Considering the Y+ domain, the electric fields represented by the domain coordination became $E_1 = E_x = 0$, $E_2 = -E_z = -E_0 \sin\varphi$, and $E_3 = E_y = E_0 \cos\varphi$. Hence, by applying this to Eq. (1), the nonlinear polarizations from the *Y*+ domain are expressed as:

$$P_1^{Y+} = 2d_{15}E_1E_3 = 0. \quad \textbf{(2)}$$

$$P_2^{Y+} = 2d_{15}E_2E_3 = -E_0^2 d_{15} \sin 2\varphi. \quad \textbf{(3)}$$

$$P_3^{Y+} = d_{31}E_1^2 + d_{31}E_2^2 + d_{33}E_3^2 = E_0^2 d_{31} \sin^2\varphi + E_0^2 d_{33} \cos^2\varphi. \quad \textbf{(4)}$$

In addition, the SHG intensity, I, is proportional to $P \times P^*$, and, for the *Y*+ domain, **y** and **z** are parallel to U_3 and U_2, respectively. Therefore, it follows that:

$$I_y^{2\omega} \propto P_3^2 = (E_0^2 d_{31} \sin^2\varphi + E_0^2 d_{33} \cos^2\varphi)^2 \quad \textbf{(5)}$$

$$I_z^{2\omega} \propto P_2^2 = (E_0^2 d_{15} \sin 2\varphi)^2 \quad \textbf{(6)}$$

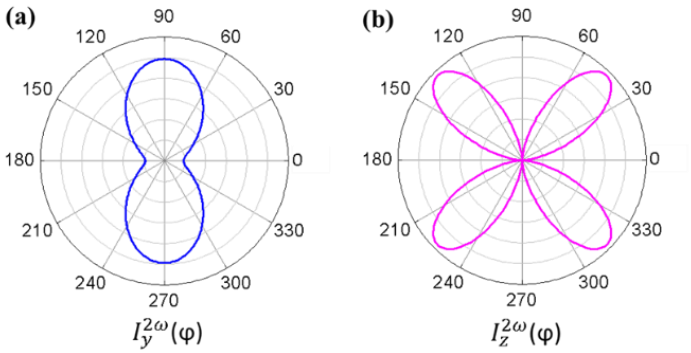

Figure 4.4 The calculated azimuthal-dependent polarized SHG, $I_y^{2\omega}(\varphi)$ and $I_z^{2\omega}(\varphi)$, of a single *Y*+ domain BTO thin film. The tensors d_{ij} from a bulk a BTO crystal were used: d_{15} = 17 pm/V, d_{31} = 15.7 pm/V, and d_{33} = 6.8 pm/V. The thickness of the BTO crystal was 500 nm. $I_y^{2\omega}(\varphi)$ and $I_z^{2\omega}(\varphi)$ showed distinct two-lobed and four-lobed SHG patterns, respectively.

The reported SHG coefficients of bulk BTO crystal at λ = 1060 nm are d_{15} = 17 pm/V, d_{31} = 15.7 pm/V, and d_{33} = 6.8 pm/V.[23] Figure 4.4 plots the **y** and **z** polarized SHG signals created from the *Y*+ domain when the incident light polarization was rotated along φ on the **y**-**z** plane. $I_y^{2\omega}$ exhibited a two-lobed intensity profile while $I_z^{2\omega}$ had a distinguishable four-lobed profile. Similarly, the nonlinear polarizations contributed by the *Y*+, *Y*-, *Z*+, and *Z*- domains were calculated and represented by the domain coordinates, which are summarized as:

$$P_1^{Y+} = P_1^{Y-} = P_1^{Z+} = P_1^{Z-} = 0 \quad \textbf{(7)}$$

$$P_2^{Y+} = P_2^{Y-} = -P_2^{Z+} = -P_2^{Z-} = -E_0^2 d_{15} \sin 2\varphi \quad \textbf{(8)}$$

$$P_3^{Y+} = P_3^{Y-} = E_0^2 d_{31} \sin^2 \varphi + E_0^2 d_{33} \cos^2 \varphi \quad \textbf{(9)}$$

$$P_3^{Z+} = P_3^{Z-} = E_0^2 d_{31} \cos^2 \varphi + E_0^2 d_{33} \sin^2 \varphi \quad \textbf{(10)}$$

When the pump light passed through a BTO thin film containing different ferroelectric domains, the SHG contributed by each of these domains needs to be considered. The area fractions

of each domain are defined as A^{Y+}, A^{Y-}, A^{Z+}, and A^{Z-}, where the sum of all the area fractions is 1. From the transformation between the domain variants and the lab coordinates shown in Figure 4.2, it was concluded that $P_y^{Y+} = P_3^{Y+}$, $P_y^{Y-} = -P_3^{Y-}$, $P_y^{Z+} = P_2^{Z+}$, and $P_y^{Z-} = -P_2^{Z-}$. Using Eq. (7) - (10), the total nonlinear polarization $P_y^{2\omega}$ created by the four domains, *Y*+, *Y*-, *Z*+, and *Z*-, is:

$$P_y^{2\omega} = A^{Y+}P_y^{Y+} + A^{Y-}P_y^{Y-} + \left(A^{Z+}P_y^{Z+} + A^{Z-}P_y^{Z-}\right)e^{i\Gamma}$$
$$= A^{Y+}P_3^{Y+} - A^{Y-}P_3^{Y-} + (A^{Z+}P_2^{Z+} - A^{Z-}P_2^{Z-})e^{i\Gamma}$$
$$= \delta A_Y P_3^{Y+} + \delta A_Z P_2^{Z+} e^{i\Gamma}. \quad \textbf{(11)}$$

δA_Y and δA_Z are defined as $\delta A_Y = (A^{Y+} - A^{Y-})$ and $\delta A_z = (A^{Z+} - A^{Z-})$, which present the difference in the area fractions between the domain pairs, such as (*Y*+, *Y*-) and (*Z*+, *Z*-), oriented along the opposite directions. From Eq. (11), $P_y^{2\omega}$ is strongly correlated with the domain orientation and the domain fraction of the opposite polarization. Due to the difference of the refractive indexes along the c and a axes of the BTO, a phase term $\Gamma = (2\pi l/\lambda)(n_c^{2\omega} - n_a^{2\omega})$ was added to Eq. (11) to account for the birefringence between the c and a axes. Here, l is the thickness of the thin film sample, and $n_c^{2\omega}$ and $n_a^{2\omega}$ are the refractive indexes at the second harmonic frequency 2ω along the c and a axes of BTO, respectively. If these four domains have equal areas, no SHG signal will be observed because δA_Y and δA_z become zero in Eq. (11). Since $I_y^{2\omega} \propto P_y^{2\omega}\left(P_y^{2\omega}\right)^*$, the SHG intensity of the **y**-polarization is:

$$I_y^{2\omega} \propto \delta A_Y^2 (P_3^{Y+})^2 + \delta A_z^2 (P_2^{Z+})^2 \pm 2\delta A_Y \delta A_Z P_3^{Y+} P_2^{Z+} \cos(\Gamma)$$
$$= \delta A_Y^2 (d_{31}\sin^2\varphi + d_{33}\cos^2\varphi)^2 + \delta A_z^2 (d_{15}\sin 2\varphi)^2 + 2\delta A_Y \delta A_Z (d_{31}\sin^2\varphi + d_{33}\cos^2\varphi) d_{15}\sin 2\varphi \cos(\Gamma). \quad \textbf{(12)}$$

For convenience, the value of E_0 was set to 1. The expression of **y**-polarized SHG is then rewritten as:

$$I_y^{2\omega} = K_{1,y}(\cos^2\varphi + K_{2,y}\sin^2\varphi)^2 + K_{3,y}\sin^2 2\varphi + K_{4,y}\left(\cos^2\varphi + K_{2,y}\sin^2\varphi\right)\sin\ 2\varphi. \quad \textbf{(13)}$$

where $K_{1,y} = \delta A_Y^2 d_{33}^2$, $K_{2,y} = d_{31}/d_{33}$, $K_{3,y} = \delta A_Z^2 d_{15}^2$, and $K_{4,y} = 2\delta A_Y \delta A_Z d_{15} d_{33} \cos(\Gamma)$.

Using the same approach, the intensity of the **z**-polarized SHG $I_z^{2\omega}$ is:

$$I_z^{2\omega} = K_{1,z}(\cos^2\varphi + K_{2,z}\sin^2\varphi)^2 + K_{3,z}\sin^2 2\varphi + K_{4,z}\left(\cos^2\varphi + K_{2,z}\sin^2\varphi\right)\sin\ 2\varphi. \quad \textbf{(14)}$$

where $K_{1,z} = \delta A_Z^2 d_{31}^2$, $K_{2,z} = d_{33}/d_{31}$, $K_{3,z} = \delta A_Y^2 d_{15}^2$, and $K_{4,z} = 2\delta A_Y \delta A_Z d_{15} d_{31} \cos(\Gamma)$. The parameters $K_{i,j}$ derived from the **x** and **y** polarizations have the following relations:

$$\cos^2(\Gamma) = \frac{K_{4,y}^2}{4K_{1,y}K_{3,y}} = \frac{K_{4,z}^2}{4K_{1,z}K_{3,z}}. \quad \textbf{(15)}$$

and

$$\frac{d_{33}}{d_{31}} = K_{2,z} = \frac{1}{K_{2,y}} \quad \textbf{(16)}$$

The SHG intensity can be calculated by Eq. (13) and (14) when all the $K_{i,j}$ are known. On the other hand, $K_{i,j}$ and the associated material parameters, including the domain fraction difference δA and nonlinear coefficient d_{ij}, can be extrapolated by fitting the experimentally obtained SHG. In parallel, Eq. (15) and (16) establish the relationship between the eight $K_{i,j}$ identities and validate the model used to interpret the domain orientation and the optical nonlinearity.

Hence, the polarimetric response of the SHG is determined by the domain fraction ratio $\delta A_Y/\delta A_Z$ and the optical nonlinearity d_{ij}. To examine the effect of $\delta A_Y/\delta A_Z$, Figure 4.5 (a), (b), and (c) show thecalculated angular-dependent $I_y^{2\omega}(\varphi)$ and $I_z^{2\omega}(\varphi)$ by applying Eq. (13) and (14) at $\delta A_Y/\delta A_Z$ = 10, 1, and 0.1, respectively. The values of the optical nonlinear coefficients, d_{15} =

17 pm/V, d_{31} = 15.7 pm/V, and d_{33} = 6.8 pm/V, were obtained from a bulk BTO crystal. As shown in Figure 5 (a), at $\delta A_Y/\delta A_Z$ = 10, the Y domains were the dominant factor for the polarimetric SHG pattern, resulting in a two-lobed $I_y^{2\omega}$ profile and a four-lobed $I_z^{2\omega}$ profile. The two-lobed $I_y^{2\omega}$ had its maximum SHG intensity at φ = 80° and 260°. On the other hand, the four-lobed $I_z^{2\omega}$ had its maximum SHG intensity at φ = 45° and 235° and its other two peaks had maximum SHG intensities at φ = 135° and 315°. The SHG patterns at $\delta A_Y/\delta A_Z$ = 10 were similar to the SHG patterns in Figure 4.4, which were created from a single *Y*+ domain BTO, except that the two lobes of the $I_y^{2\omega}(\varphi)$ were slightly tilted away from the vertical axis and the maximum SHG intensities from those four lobes in $I_y^{2\omega}(\varphi)$ were different. When $\delta A_Y/\delta A_Z$ was decreased to 1, the *Y* and *Z* domains had comparable contributions to the SHG, thus creating $I_y^{2\omega}$ and $I_z^{2\omega}$ patterns with similar profiles as shown in Figure 4.5 (b). Both $I_y^{2\omega}(\varphi)$ and $I_z^{2\omega}(\varphi)$ have two lobes and these lobes are approximately 45° away from the horizontal axis. Once $\delta A_Y/\delta A_Z$ was further decreased to 0.1, the Z domains became the dominant factor for the polarimetric SHG pattern. As result, a four-lobed $I_y^{2\omega}$ profile and a two-lobed $I_z^{2\omega}$ profile were found and are illustrated in Figure 4.5 (c). Unlike Figure 4.5 (a) where the two lobes from $I_y^{2\omega}(\varphi)$ were closely aligned to the vertical axis, the other two lobes from $I_z^{2\omega}(\varphi)$ in Figure 4.5 (c) were almost aligned with the horizontal axis. Therefore, the symmetry and the angular dependence of the polarimetric SHG patterns are highly dependent to the domain fraction ratio. In other words, $\delta A_Y/\delta A_Z$ can be resolved by examining the variation of the $I_{y,z}^{2\omega}(\varphi)$ profiles.

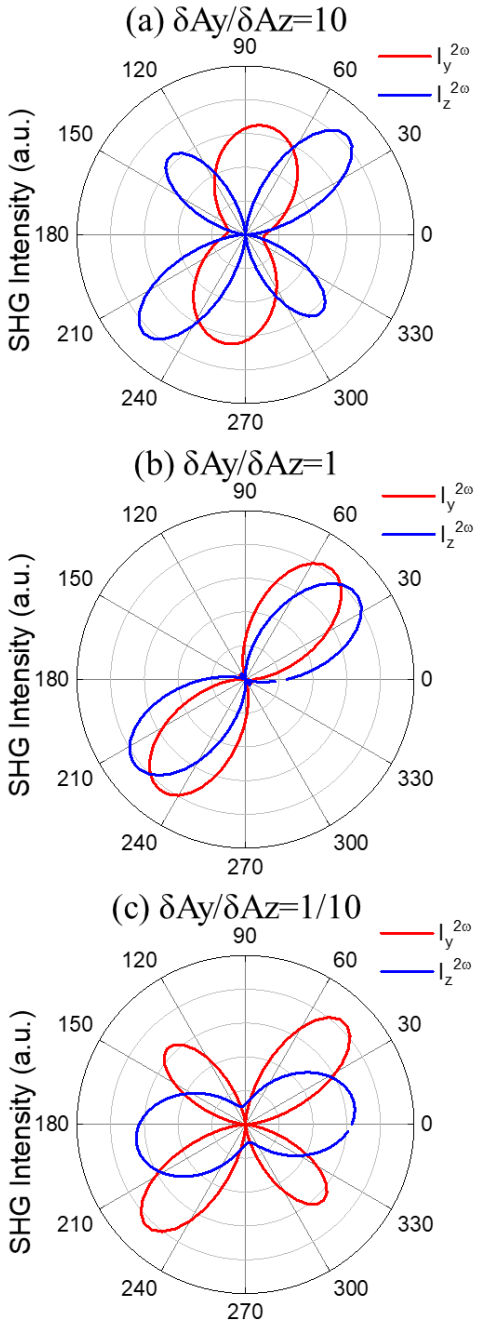

Figure 4.5 The $I_y^{2\omega}(\varphi)$ and $I_z^{2\omega}(\varphi)$ were calculated when the ferroelectric domain fraction ratio, $\delta A_Y/\delta A_Z$, was set equal to (a) 10, (b) 1, and (c) 0.1. The d_{ij} values were from bulk a BTO crystal. At $\delta A_Y/\delta A_Z$ = 10, $I_y^{2\omega}(\varphi)$ had a two-lobed profile and $I_z^{2\omega}(\varphi)$ had a four-lobed profile. As $A_Y/\delta A_Z$ decreased to 0.1, $I_y^{2\omega}(\varphi)$ became four-lobed and $I_z^{2\omega}(\varphi)$ became two-lobed. In addition, the axis of the two-lobes rotated as $\delta A_Y/\delta A_Z$ changed.

4.2.3 Polarimetric mid-IR SHG measurements

Experimental setup

Figure 4.6 shows the schematic of the experimental setup for measuring the polarimetric SHG from a BTO thin film. A wavelength-tunable OPO pulsed laser was used as the mid-IR light source. The pulse repetition rate was 1 kHz and the linewidth was smaller than 10 cm^{-1}. A bandpass filter with a transmission window from $\lambda = 3.25$ μm to 3.75 μm was placed after the laser. The maximum transmission was 80 % at $\lambda = 3.50$ μm. This filter was used to block the light frequencies other than the laser beam that had pumping frequency of ω. After the 1st bandpass filter, the laser beam was focused onto the sample surface through a mid-IR objective lens to maximize the incident light intensity. The focusing length and the numerical aperture of the mid-IR objective lens was 6 mm and 0.25, respectively. The incident laser beam was projected along the **x**-direction. By rotating the half-wave plate, the polarization of the laser beam was also rotated by an azimuth angle φ along the **x**-axis. The half-wave plate had a 100% transmission and 1.5 wave retardance at $\lambda = 3.5$ μm. The BTO thin film sample was initially placed on a rotating stage to align the sample axes with the lab axes, so that $\mathbf{x} \,//\, [001]_{STO}$, $\mathbf{y} \,//\, [100]_{STO}$, and $\mathbf{z} \,//\, [010]_{STO}$. Otherwise, there will be an angle α between the principal c-axis of the $BaTiO_3$ sample and the lab coordinate **y**-axis. The angle between lab coordinate **y**-axis and the direction normal to the BTO thin film surface is $\theta = 90°$ so that the input light was normally incident to the sample. To effectively collect all of the SHG signal, the light emitted from the BTO sample was collected and then refocused into a detector by two separate objective lenses. An ultra-broadband wire grid polarizer operational between $\lambda = 0.25 – 4$ μm was placed after the objective lens as an analyzer to differentiate the polarized SHG, $I_y^{2\omega}$ or $I_z^{2\omega}$. The extinction ratio of the wire-grid polarizer was 10:1. A second bandpass filter with a transmission window from $\lambda = 1.5$ to 2.0 μm was placed in front of the

detector to remove the remaining incident laser beam at frequency ω. Thus, only the generated SHG signal at 2ω was collected. The detector was a PbSe fixed gain photodetector sensitive from λ = 1.5 to 4.8 μm with a bandwidth range from 0.2 Hz to 10 kHz. The detector was connected to an oscilloscope and the SHG signal at various φ was recorded from the amplitude of the pulse displayed on the oscilloscope.

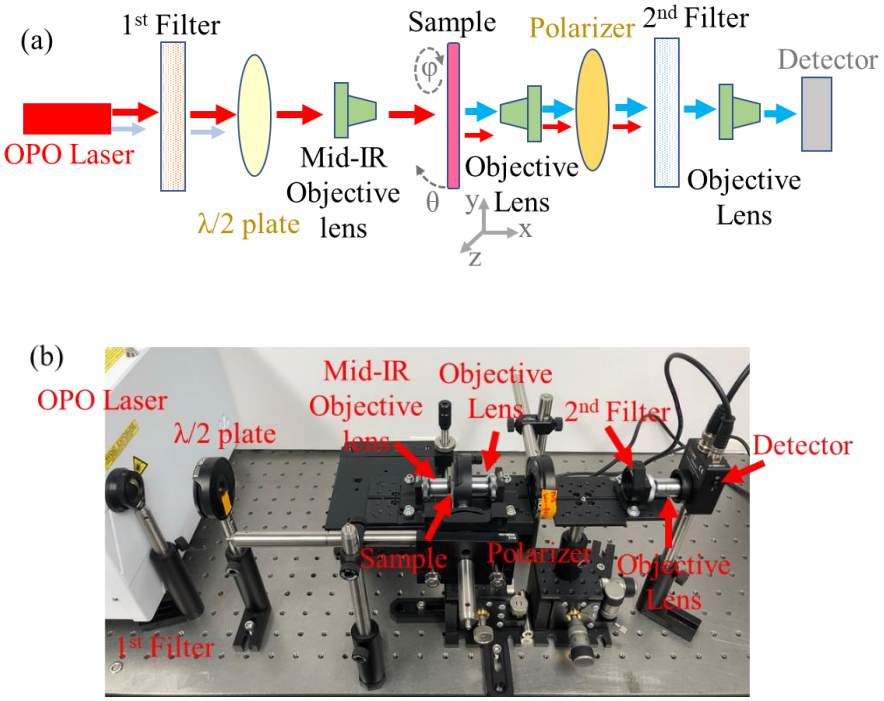

Figure 4.6 (a) A schematic of the experimental setup for measuring the azimuthal-dependent polarized SHG from a BTO thin film; (b) measurement setup. The pumping laser was a tunable ns pulsed laser and the 1st filter removed the light that was not at the pumping wavelength λ. The polarization of the light was rotated by the λ/2 phase plate. The mid-IR light was focused on the BTO thin film using the front objective lens and the SHG was collected by another objective lens in the back. The polarizer selected the polarization of the SHG signals, and the 2nd filter removed the residual mid-IR pumping light. The SHG at the NIR region was measured by a photodetector or a spectrometer.

Mid-IR second-order optical nonlinearity and ferroelectric domain fractions

To investigate the optical nonlinearity and the ferroelectric domains of the BTO thin film, the azimuth-dependent SHG signals along the **y** and **z** polarizations, $I_y^{2\omega}(\varphi)$ and $I_z^{2\omega}(\varphi)$, were

measured and displayed in Figure 4.7 (a) and (b), respectively. The substrate STO had no second-order nonlinearity due to its crystal symmetry. Both **y** and **z** polarized SHG patterns show a dominant two-lobed profile with a pair of smaller lobes. For $I_y^{2\omega}(\varphi)$, the maximum SHG signal was found at a relative φ = 45° and 135°. The smaller lobes were found to be normal to the larger lobes. Similar profiles were observed for $I_z^{2\omega}(\varphi)$, where a pair of larger lobes and another pair of secondary lobes were found. A minor difference between the $I_y^{2\omega}(\varphi)$ and $I_z^{2\omega}(\varphi)$ is that the intensities of the secondary lobes were comparatively weaker in $I_z^{2\omega}(\varphi)$ than in $I_y^{2\omega}(\varphi)$. The SHG profiles shown in Figure 4.7 were fitted by Eq. (13) and (14). Accordingly, d_{15} = 12.5 pm/V, d_{31} = 9.0 pm/V, d_{33} = 10.0 pm/V, and $\delta A_Y/\delta A_Z$ = 1 were obtained. The fitting results were consistent with the observation shown in Figure 4, where $I_z^{2\omega}(\varphi)$ and $I_y^{2\omega}(\varphi)$ revealed a two-lobed dominant pattern when $A_Y/\delta A_Z$ approached 1.

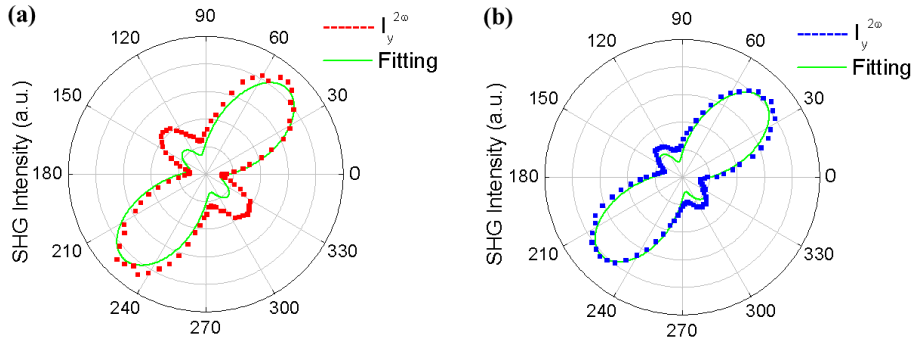

Figure 4.7 The (a) $I_y^{2\omega}(\varphi)$ and (b) $I_z^{2\omega}(\varphi)$ obtained from the BTO thin film deposited by PLD. The dashed lines represent the measured data and the solid green lines represent the modeling results. From the fitting, the values d_{15} = 12.5 pm/V, d_{31} = 9.0 pm/V, d_{33} = 10.0 pm/V, and $\delta A_Y/\delta A_Z$ = 1 were resolved.

Mid-IR SHG dependence on the pumping light intensity

The variation of the SHG at different pumping light intensities were investigated. During the measurement, the laser power I_{laser} was gradually increased from 16 mW to 92 mW. The laser wavelength was λ = 3.5 μm and the azimuth angle φ was fixed at 45° because $I_y^{2\omega}(\varphi)$ reached its

maximum at 45° according to Figure 4.7 (a). Figure 4.8 displays the SHG intensity vs. the square of the pumping light intensity, $(I_{laser})^2$, where I_{laser} was measured by a digital optical power meter (Thorlabs PM100D). The SHG intensity increased proportionally to $(I_{laser})^2$ when I_{laser}gradually increased from 16 mW to 92 mW. The linear dependence obtained between $I_y^{2\omega}$and $(I_{laser})^2$agrees with the derivation illustrated in Eq. (5) and (6).

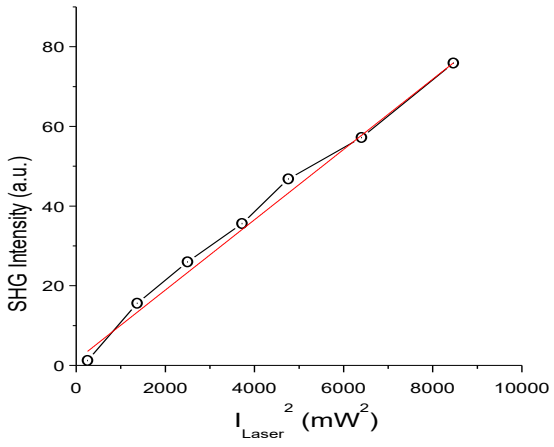

Figure 4.8 The SHG intensity, $I_y^{2\omega}$, versus the square of the input mid-IR laser power, $(I^{\omega})^2$, measured at λ = 3.5 μm. The black circles indicate the measured data and the red line represents the fitted curve. A linear relationship between $I_y^{2\omega}$ and $(I^{\omega})^2$ was found.

Mid-IR SHG spectral characterization

The SHG spectrum from the BTO thin film was measured when the wavelength of the pumping laser was tuned over a range between λ^{ω} = 3.0 and 3.6 μm. The SHG signal was collected by a 400 μm core diameter fiber and analyzed by a spectrometer that had a thermoelectric cooling InGaAs linear array. The azimuthal angle φ and the position of the BTO sample were fixed when the input wavelength was tuned. As drawn in Figure 4.9, the center wavelength of the SHG spectrum increased from $\lambda^{2\omega}$ = 1.5 to 1.8 μm when the laser pumping wavelength increased from

λ^{ω} = 3.0 to 3.6 μm. The slight broadening of the SHG spectrum at $\lambda^{2\omega}$ < 1.65 μm was due to variation in the pumping laser linewidth. The spectral scanning of the SHG signals demonstrate that the deposited BTO thin film can convert mid-IR signals over a wide spectrum efficiently into the NIR region, thus enabling on-chip and broadband nonlinear frequency conversion.

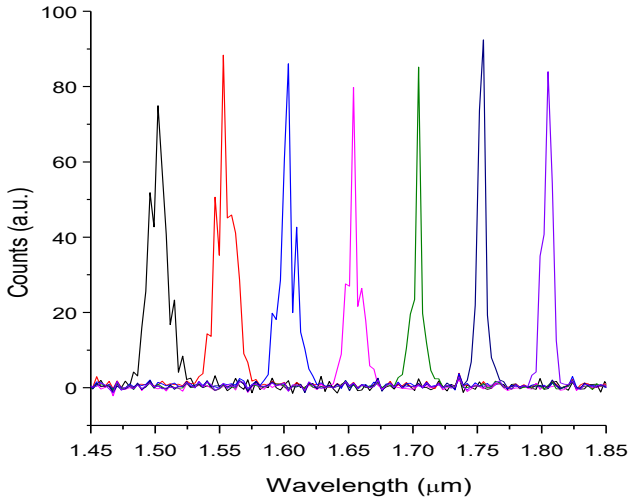

Figure 4.9 The SHG spectrum of the BTO thin film when the mid-IR pumping wavelength was tuned from λ^{ω} = 3.0 to 3.6 μm. Strong SHG signals between $\lambda^{2\omega}$ = 1.5 and 1.8 μm were found, indicating that BTO has a broadband second order optical nonlinearity.

4.2.4 Conclusions

Broadband mid-IR SHG was demonstrated by an epitaxial BTO thin film on an (001) STO substrate using PLD. From XRD characterization, the BTO film had cube-on-cube growth mainly along the (00l) direction. The mid-IR optical nonlinearity and the ferroelectric domain property were characterized by azimuthal-dependent polarized SHG measurements. Two-lobed dominant $I_{x,y}^{2\omega}(\varphi)$ patterns were found in both polarizations. High nonlinear coefficients of d_{15} = 12.5 pm/V, d_{31} = 9.0 pm/V, and d_{33} = 10.0 pm/V, and a uniform domain fraction ratio of $\delta A_Y/\delta A_Z$ = 1 were resolved. In addition, the characteristic SHG response, $I^{2\omega} \propto (I^{\omega})^2$, and broadband SHG signals were observed at pumping wavelengths λ^{ω} = 3.0 - 3.6 μm. The efficient nonlinear thin film paves the way for developing efficient on-chip light sources and integrated quantum photonics.

4.3 Mid-IR pumped second harmonic generation from $BaTiO_3$ thin film waveguides

4.3.1 Introduction

We developed a mid-IR nonlinear microphotonic device built on an epitaxial BTO thin film. Our previous work has shown that PLD grown BTO films revealed strong mid-IR SHG and the SHG intensity was determined by the ferroelectric domain structure and tensorial $\chi^{(2)}$ property of the film [24]. To further improve the nonlinear process, it requires a higher coupling efficiency and a longer interaction distance between the light and the BTO, which can be achieved by applying microphotonic components like directional couplers and optical waveguides. Nevertheless, creating device structures on BTO is difficult due to its hardness and chemical inertness. An alternative approach is to add a lower refractive index film on the BTO layer forming a strip-loaded structure. In our case, a SiN grating coupler and a SiN strip waveguide were developed above the BTO layer that can efficiently couple the mid-IR pumping light into the BTO thin film and guide the light propagation. Simulations from the finite element method (FEM) show both the mid-IR pumping light and the excited NIR SHG were effectively guided in the BTO layer because of the large refractive-index difference between the SiN and the BTO layers. The intensity and the spectrum of the SHG were experimentally measured when the pumping wavelength was tuned from $\lambda = 3.30$ to 3.45 μm to evaluate the mid-IR nonlinear response of the device.

4.3.2 Device design and simulation

The structure of the two-layer strip-loaded waveguide is shown in Figure 4.10 (a). The top SiN layer has a strip waveguide in the center where the strip is used to guide the light propagation of the pumping mid-IR and the NIR SHG. Adjacent to the strip is the grating components used to couple the mid-IR pumping light into the device. The second layer of the device is the epitaxial BTO thin film that confines the mid-IR light and the NIR SHG. Below the BTO layer is the STO substrate. The waveguide modes were calculated by FEM where the structure used in the modeling is shown in Figure 4.10 (b). The SiN strip has a thickness of 0.7 μm and a width of 5 μm, and the thickness of the BTO layer is 0.5 μm. The refractive indexes of the SiN, BTO, and STO are 1.93, 2.34, and 2.22, respectively. The structure parameters of the device chosen here match the fabricated device shown in Fig. 3. Figure 4.10 (c) and (d) displayed the calculated 2-D mode profile and its 1-D intensity distribution along the z direction at $\lambda = 3.40$ μm. The mid-IR waveguide mode was clearly confined in the BTO layer since the refractive index of the BTO is larger than the SiN and STO. In addition, the top SiN strip effectively confine the waveguide mode along the x direction. Figure 4.10 (e) and (f) illustrated the mode profile and intensity distribution at $\lambda = 1.70$ μm corresponding to the frequency doubling from $\lambda = 3.40$ μm. Similar mode pattern and intensity distribution were obtained at the NIR region demonstrated that our strip-loaded waveguide can effectively guide both the mid-IR pumping light and the excited NIR SHG.

Grating couplers were used in the device to couple the free space pumping mid-IR into the waveguide device. The design of the grating component applied the following equation:

$$n_1 \sin(\theta) = n_{eff} - \frac{m\lambda}{a} \quad (1)$$

Where θ is the diffraction angle, m is the diffraction order, n_1 is the refractive index of air, n_{eff} is the effective refractive index of the SiN strip loaded waveguide, a is the grating period, and λ is

the mid-IR wavelength. From the equation, the grating periodicity was chosen to be 4 μm to couple the light at λ = 3.4 μm with m = 2 and θ = 30°.

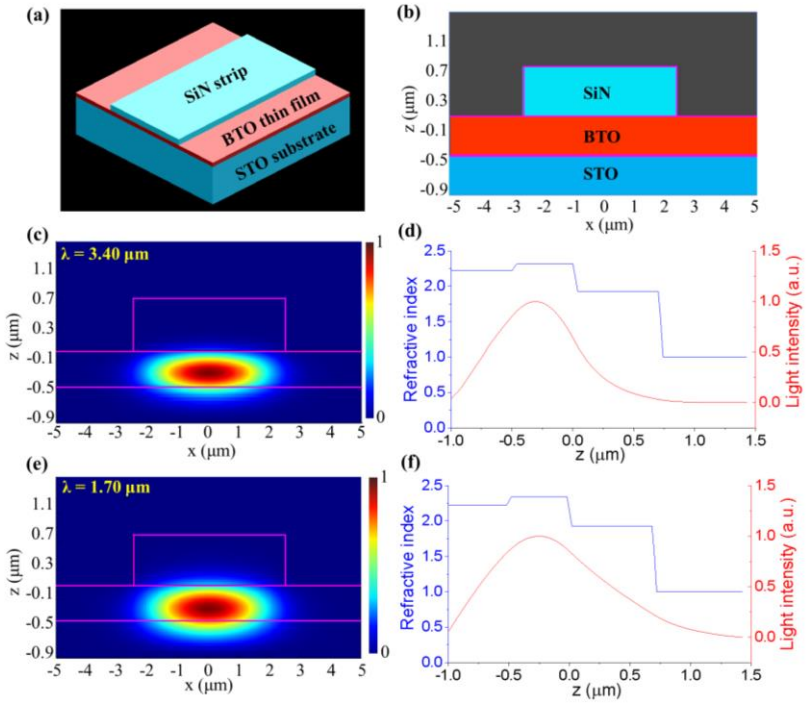

Figure 4.10 (a) The structure of the two-layer SiN on BTO strip-loaded waveguide. (b) The cross-section of the waveguide structure consists of the SiN strip and the nonlinear BTO layer. (c) The calculated 2-D mode profile and (d) the 1-D intensity distribution along the z direction at pumping λ = 3.40 μm. (e) The calculated 2-D mode profile and (f) the 1-D intensity distribution along the z direction at SHG λ = 1.70 μm.

4.3.3 Device fabrication and characterization

The device fabrication scheme is displayed in Figure 4.11 that includes the depositions of the BTO and the SiN thin films, then followed by the photolithography and the waveguide pattern transferring through selective etching. The BTO thin films were grown on single-crystal STO substrates by PLD. STO was selected as the substrate material because its lattice parameter of a = 3.905 Å is close to the BTO of a = 3.992 Å with tetragonal symmetry. During the deposition, a BTO target was exposed to a λ = 248 nm KrF excimer laser that has a fluence of 1.5 J/cm^2 and a repetition rate of 5 Hz. The STO substrate was heated to 600 °C and the pressure of O_2 was maintained at 20 mTorr. The subsequent fabrications of the SiN strip waveguides and the grating couplers were completed by the standard CMOS fabrication process. A 700 nm thick SiN film was deposited on the BTO layer using the plasma-enhanced chemical vapor deposition (PECVD). The grating and the strip structures were defined by the photolithography. A positive photoresist S1818 was spin-coated on the device at 3000 rpm, then baked at 115 °C. A photomask with patterns of waveguides and grating couplers was applied. After the exposure, the photoresist was developed in the developer MF-319 and then hard-baked at 130 °C for 5 min. Reactive-ion etching (RIE) with 40 sccm CHF_3 and 5 sccm O_2 was used to selectively etch the SiN layer and stop at the BTO layer. The RIE pressure was 60 mTorr and the power applied was 200 W. A SiN etching rate of 30 nm/min was obtained. The developed fabrication processes created the device structures, including the grating and the strip, in the top SiN layer instead of the BTO thin film. BTO is a mechanically hard and chemically inert material, thus being difficult to apply etching process.

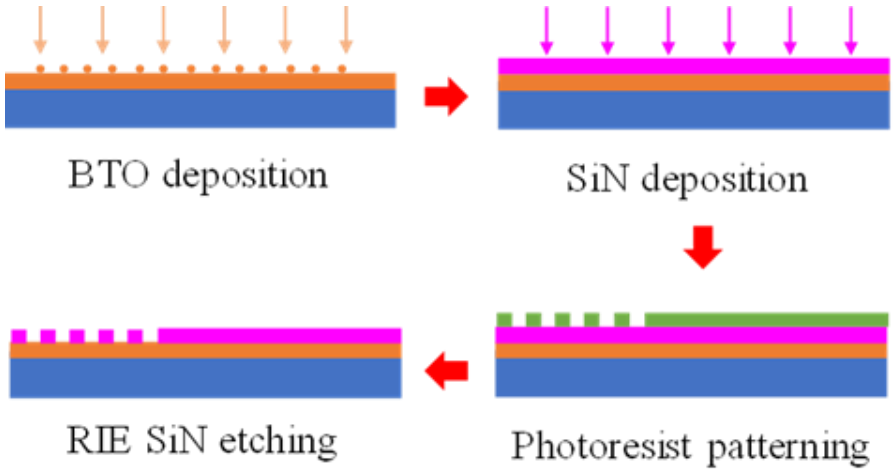

Figure 4.11 The device fabrication processes to create the SiN on BTO strip-loaded waveguides. The BTO thin film was deposited on the STO substrate by PLD and the SiN was prepared by PECVD. CHF_3 and O_2 were used for selective SiN etching.

The structure of the fabricated strip-loaded waveguides was characterized by the optical microscopy and the scanning electron microscopy (SEM). From the optical image in Figure 4.12 (a), the grating coupler in the SiN layer is 2 mm wide and 2 mm long. There is a 2 mm long taper structure connecting the grating coupler and the waveguide. Figure 4.12 (b) is the enlarged SEM image from the gating showing the grating period is 4.5 μm and the filling factor is 0.56. Figure 4.12 (c) is the SEM image of the 5 μm wide SiN strip waveguide. The grating and the strip waveguide both have sharp and well-defined structures, which are required to achieve low optical propagation loss and efficient nonlinear optical conversion. The crystalline structure of the BTO thin film was characterized by the x-ray diffraction (XRD). From the θ-2θ scan in Figure 4.13, only the BTO (00*l*) and the STO substrate (00*l*) diffraction peaks were found, indicating that the BTO thin film is a crystalline film and grew along the (00*l*) direction.

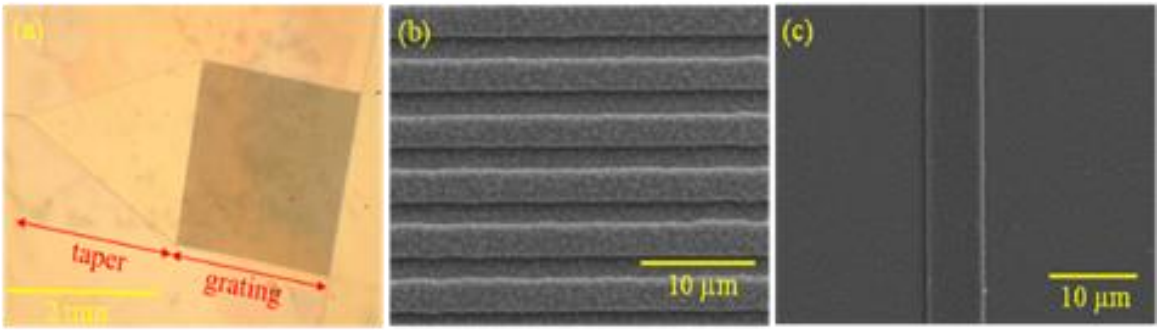

Figure 4.12 (a) The optical image of the grating coupler connected with the taper and the waveguide. The SEM images of (b) the grating structure and (c) the SiN strip waveguide.

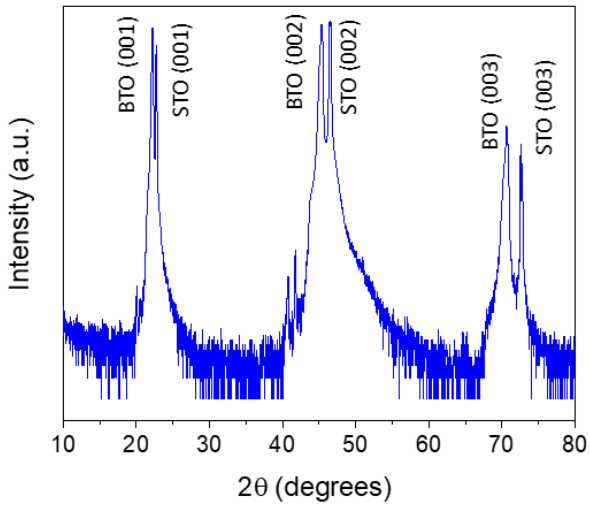

Figure 4.13 XRD θ-2θ scan of the BTO thin film deposited on STO (100) substrate. Only (00*l*) diffraction peaks were found.

4.3.4 Experimental setup and measurement of the mid-IR SHG

The schematic and the experimental setup to measure the frequency doubling from the waveguide devices are shown in Figure 4.14 (a) and (b). The mid-IR pumping light source is an optical parametric oscillator (OPO) tunable pulsed laser with a wavelength scanning range at λ = 2.5 - 12 μm, maximum output of 200 μJ, linewidth $<$ 10 cm^{-1}, repetition rate of 1 kHz, and pulse duration $<$ 12 ns. An optical band-pass filter was placed after the OPO laser to block all the light frequencies except the mid-IR pumping light. The center wavelength of the band-pass filter is λ = 3.25 μm and the full width at half maximum (FWHM) is 0.50 μm. A mid-IR objective lens was used to focus the mid-IR light onto the grating coupler. The waveguide device was mounted on a rotating stage so the coupling angle between the mid-IR pumping light and the grating coupler can be adjusted to optimize the coupling efficiency.

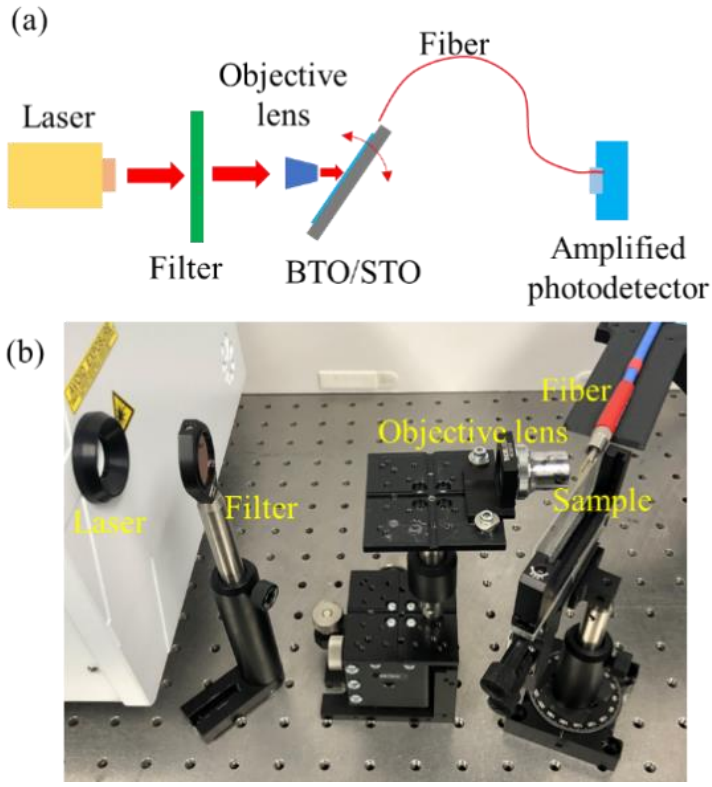

Figure 4.14 (a) Schematic and (b) experimental setup for measuring the SHG signals from the SiN on BTO strip-loaded waveguides. The photodetector was replaced by an InGaAs linear array detector during the SHG spectrum characterization.

An As_2Se_3 chalcogenide fiber was used to collect the SHG signal. One end of the fiber was pointed to the waveguide edge and the other end of the fiber was connected to an InGaAs single pixel photodetector. The As_2Se_3 fiber has a 300 μm core diameter and it is transparent between λ = 1.5 and 10 μm. The amplified photodetector has a variable-gain option and a detection window between λ = 0.9 and 1.7 μm. The photodetector was connected to an oscilloscope to read the SHG intensity. During the SHG spectrum characterization, a 400 μm core diameter fiber was placed after the waveguide device and connected to a spectrometer that consists of a thermoelectric cooling InGaAs linear array detector operating between λ = 0.9 and 2.5 μm.

The dependence between the SHG intensity and the mid-IR pumping power is plotted in Figure 4.15. The laser output power was measured by using a digital optical power meter (Thorlabs PM100D) placed in front of the mid-IR OPO laser. During the measurement, the laser wavelength was tuned to λ = 3.3 μm and its power was gradually decreased from 110 to 96, 82, 69, 58, and 45 mW. From Figure 4.15, a near linear dependence between the SHG intensity and the square of mid-IR pumping power was found. This result is consistent with characteristic SHG response since the relationship between the SHG intensity $I(2\omega)$ and the pumping intensity $I(\omega)$ can be derived as following

$$I(2\omega) \propto E^2(2\omega) \tag{2}$$

$$E(2\omega) \propto P^{(2)}(2\omega) = \chi^{(2)}E(\omega)E(\omega) = \chi^{(2)}I(\omega) \tag{3}$$

where ω is light frequency, E is the electric field, and $P^{(2)}$ is the induced second-harmonic polarization.

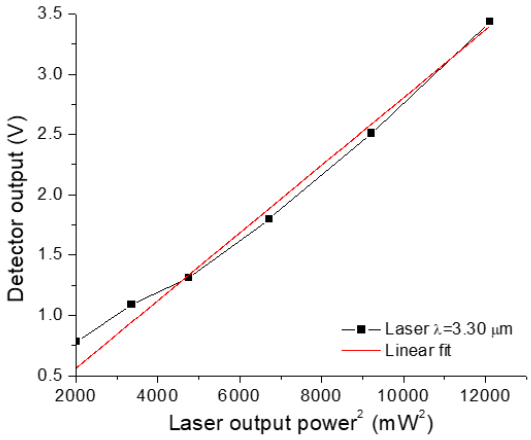

Figure 4.15 The measured SHG intensity at different laser power that increased from 45 to 110 mW. The wavelength of the mid-IR pumping laser is λ = 3.30 μm.

The SHG spectrum from the waveguide device was measured when the mid-IR pumping wavelength was consequently tuned from λ = 3.30, 3.35, 3.40, to 3.45 μm. As shown in Figure

4.16, the center wavelength of the SHG spectrum gradually shifted from λ = 1.65, 1.675, 1.70, to 1.725 μm as the mid-IR pumping wavelength increased. The results indicate the doubling frequency remained efficient over a spectrum of 150 nm wide in the mid-IR region, which is critical in the development of broadband mid-IR nonlinear photonic devices.

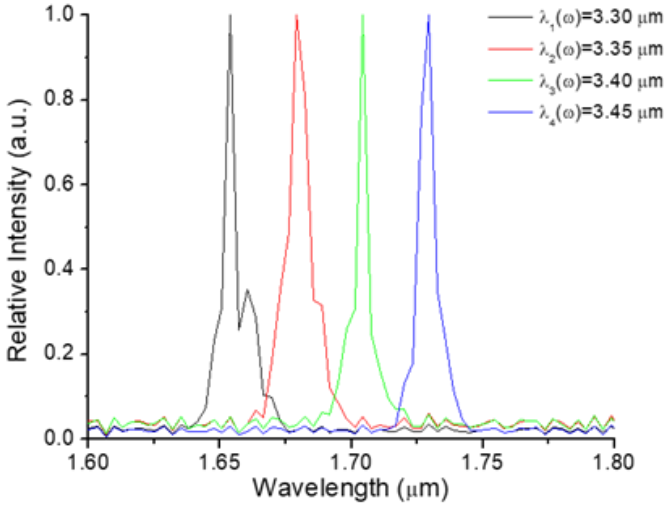

Figure 4.16 SHG spectrum for the laser pumping wavelength at λ = 3.30, 3.35, 3.40, to 3.45 μm.

4.3.5 Conclusion

Nonlinear mid-IR integrated photonics were demonstrated using SiN strip-loaded BTO thin film waveguides. The epitaxial BTO film was deposited on a STO substrate using PLD. By using the SiN grating coupler, the mid-IR pumping light was coupled into the nonlinear BTO layer. The mid-IR pumping light and the SHG at NIR were both effectively confined in the BTO because of its higher refractive index comparing to SiN and STO substrate. In addition, SHG was achieved over a broad mid-IR pumping range at λ = 3.30 - 3.45 μm, where characteristic SHG response $I(2\omega) \propto I^2(\omega)$ was observed. The nonlinear BTO waveguide offers a platform for integrated quantum photonics and all-optical switching.

4.4 Mid-infrared nonlinear frequency conversion using epitaxial barium titanate on silicon-on-insulator

4.4.1 Introduction

Complex metal oxides including $LiNbO_3$, $LaTiO_3$, and $BaTiO_3$ with a perovskite crystal structure is critical in nonlinear photonics because of their large second order optical nonlinearity. The ferroelectricity and the optical nonlinearity of perovskite oxides are attributed to their non-centrosymmetric structure and transition-metal B cations [25]. The nonlinear response from the spontaneous dipole moment within a perovskite unit cell can result in photons that carry an energy different from the exciting laser. By mixing or splitting the energies from the incoming photons, coherent lightwave with specific wavelengths is created through various mechanisms, such as SHG, sum-and difference- frequency generation (SFG and DFG), and optical parametric oscillation (OPO). Bulk perovskite oxide single crystals have been utilized in various nonlinear photonic systems, including $LiNbO_3$ and $LaTiO_3$ based OPO and optical parametric amplification (OPA) [26,27]. Applying quasi-phase matching on these perovskite oxide crystals, nonlinear frequency conversion becomes more efficient and provides coherent light sources over a broad spectrum [28-30]. In addition, the nonlinear optical method can generate entangled a photon-pair through parametric down-conversion, which is critical for the development of quantum communication and networking [31,32].

Nevertheless, compact devices desire perovskite oxides thin films over conventional bulk crystals for numerous chip-scale applications, such as electro-optic modulators [33], gas sensors [34], and non-volatile memory devices [35]. Deposition methods like atomic layer deposition (ALD), molecule-beam epitaxy (MBE), and chemical vapor deposition (CVD) have been explored to grow crystalline perovskite oxide thin films [36-39]. Among various candidates of nonlinear

optical thin films, BTO has received significant attention for the applications in the integrated photonic circuits. BTO has the advantages of wide spectral transparency [40,41], strong Pockels effect [42,43], and high second-order optical nonlinearity [44]. To monolithically integrate BTO with present Si photonics, growth of epitaxial BTO thin films on Si substrates has been investigated through different deposition techniques [45,46]. For instance, thin TiN and MgO buffer layers were applied to reduce the large lattice mismatch between the BTO and the Si to enable monolithic BTO-on-Si platforms [47,48].

Though the visible and near-IR nonlinear coefficients d_{ij} of BTO-on-Si have been measured [49-51], their mid-IR optical nonlinearity remains unknown. Mid-IR is critical because it overlaps with characteristic absorptions of numerous chemical functional groups, thus enabling label-free biomolecule sensing and non-destructive chemical detection [52-56]. In addition, the wide spectral range of mid-IR provides additional bandwidth for optical network and data transmission [57]. In this work, epitaxial BTO films was grown on a SOI substrate with a strontium titanate (STO) buffer layer to reduce the lattice mismatch between the BTO and Si. Azimuthal-dependent SHG was measured to resolve the tensorial 2^{nd} optical nonlinearity and the ferroelectric domain structures. Our epitaxial BTO-on-Si provides a critical component to develop nonlinear mid-IR devices.

4.4.2 Model of the BTO azimuthal mid-IR SHG pattern

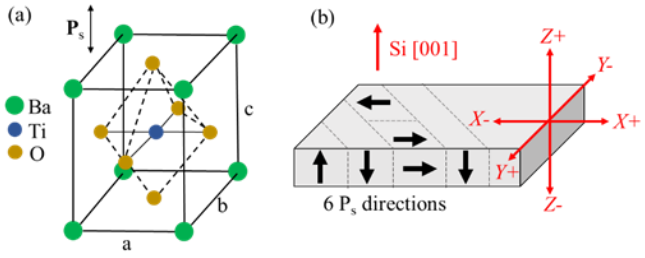

Figure 4.17 (a) The BTO unit cell with Ti in the center, Ba in the corners, and O in the facet centers. The spontaneous polarization $\mathbf{P_s}$ is parallel to the c-axis. (b) The six ferroelectric domain orientations along the *X*+, *X*-, *Y*+, *Y*-, *Z*+, and *Z*- directions.

BTO crystal has a non-centrosymmetric tetragonal phase at the temperature between 0 to 120 °C. Fig. 4.17 (a) illustrates the structure of a BTO crystal unit cell, where the O atoms are placed in the face-centered position and surround a Ti atom. A spontaneous polarization $\mathbf{P_s} \parallel$ c-axis is introduced when the Ti atom is deviated from the center of the unit cell along the c-axis [58,59]. Fig. 4.17 (b) is an illustration of the possible domain structure of a BTO thin film deposited on the Si (001) layer. The tetragonal BTO belongs to the 4mm point group. It has six domain variants, including $X+$, $X-$, $Y+$, $Y-$, $Z+$, and $Z-$, where the corresponding polarization $\mathbf{P}_s$ points into different directions. The tensor product between the 2nd order nonlinear coefficient d_{ij} and the column associated with electric field component **E** determines the 2nd order nonlinear polarization ***P*** in (1):

$$\boldsymbol{P} = \begin{pmatrix} P_1 \\ P_2 \\ P_3 \end{pmatrix} = \begin{pmatrix} 0 & 0 & 0 & 0 & d_{15} & 0 \\ 0 & 0 & 0 & d_{15} & 0 & 0 \\ d_{31} & d_{31} & d_{33} & 0 & 0 & 0 \end{pmatrix} \begin{pmatrix} E_1^2 \\ E_2^2 \\ E_3^2 \\ 2E_2E_3 \\ 2E_1E_3 \\ 2E_1E_2 \end{pmatrix} \quad (1)$$

E_1, E_2, and E_3 are the electrical fields in V_1, V_2, and V_3 directions that define the coordination

system of the ferroelectric domains. In addition, the V_3 axis is always along the dipole polarization direction. The SHG intensity $I^{2\omega}$ of a multi-domain BTO thin film can be modelled by its tensorial component d_{ij} and the domain fraction factor $\Delta D^Y/\Delta D^X$, where ΔD is the difference of the area ratio between a domain pair. For instance, $\Delta D^Y = D^{Y+} - D^{Y-}$, whereas D^{Y+} and D^{Y-} are the domain area ratios oriented along the $Y+$ and $Y-$ directions, respectively. The SHG intensity at the frequency of 2ω along the *X*-polarization, $I_X^{2\omega}$, is proportional to $P_X^{2\omega}(P_X^{2\omega})^*$ and can be found by (2):

$$I_X^{2\omega} \propto (\Delta D^X)^2(d_{31}\sin^2\theta + d_{33}\cos^2\theta)^2 + (\Delta D^Y)^2(d_{15}\sin 2\theta)^2 + 2\Delta D^X \Delta D^Y(d_{31}\sin^2\theta + d_{33}\cos^2\theta)d_{15}\sin 2\theta\cos(\Gamma) \quad (2)$$

θ is the azimuthal angle between the linearly polarized incident light and the *X*-axis, $\Gamma = (2\pi L/\lambda)(n_c^{2\omega} - n_a^{2\omega})$, L is the BTO thickness, and $n_c^{2\omega}$ and $n_a^{2\omega}$ are the refractive indexes along the c- and a- axises. The *Y*-polarized SHG intensity, $I_Y^{2\omega}$, can also be calculated through the same method. From Eq. (2), the SHG intensity is determined by the domain fraction difference ΔD and the coefficient d_{ij}, thus creating azimuthally symmetric SHG profiles. To illustrate the effect from the domain structure and the optical nonlinearity on mid-IR SHG, azimuthal $I_X^{2\omega}(\theta)$ and $I_Y^{2\omega}(\theta)$ at the different domain fraction and the ratio between the tensorial nonlinearity were calculated and plotted in in Fig. 2 Here, the parameter associated with the domain orientation is defined as $\alpha = \Delta D^X/\Delta D^Y$, and the ratios between the tensorial nonlinear coefficients are $\beta_1 = d_{33}/d_{31}$ and $\beta_2 = d_{15}/d_{31}$. In the initial condition $\alpha = 1$, $\beta_1 = 1$, and $\beta_2 = 1$, $I_X^{2\omega}(\theta)$ and $I_Y^{2\omega}(\theta)$ drawn in Fig. 4.18 (a) are overlapped and both show a symmetric two-lobed pattern because of the identical domain fraction along the *X* and *Y* orientations. In Fig. 4.18 (b), as α increases and the domain distribution between those two orientations is unequal, the center of $I_X^{2\omega}(\theta)$ plot becomes broader

and additional two lobes are found in $I_Y^{2\omega}(\theta)$. At $\alpha = 10$, the $I_X^{2\omega}(\theta)$ shows an elliptic profile instead of a two-lobed pattern. Meanwhile, the deviation of β_1 from one rotates the two-lobed $I_x^{2\omega}(\theta)$ and $I_y^{2\omega}(\theta)$ in opposite directions. As displayed in Fig. 4.18 (c), $I_X^{2\omega}(\theta)$ rotates clockwise while $I_Y^{2\omega}(\theta)$ rotates counterclockwise as β_1 increases. The pattern of $I_X^{2\omega}(\theta)$ turns into perpendicular to $I_Y^{2\omega}(\theta)$ when β_1 reaches 10. Hence, the ratio between the tensorial coefficient d_{ij} is critical in forming the angle dependent SHG profile. On the other hand, the increase of β_2 illustrated in Fig. 4.18 (d) converts the two-lobed $I_X^{2\omega}(\theta)$ and $I_Y^{2\omega}(\theta)$ to a four-lobed profile without rotating the SHG patterns. In addition, $I_X^{2\omega}(\theta)$ and $I_Y^{2\omega}(\theta)$ remains overlapped as β_2 changes. Therefore, the domain fraction factors and the tensorial nonlinear coefficients can be extrapolated by analyzing the azimuthal dependent SHG patterns.

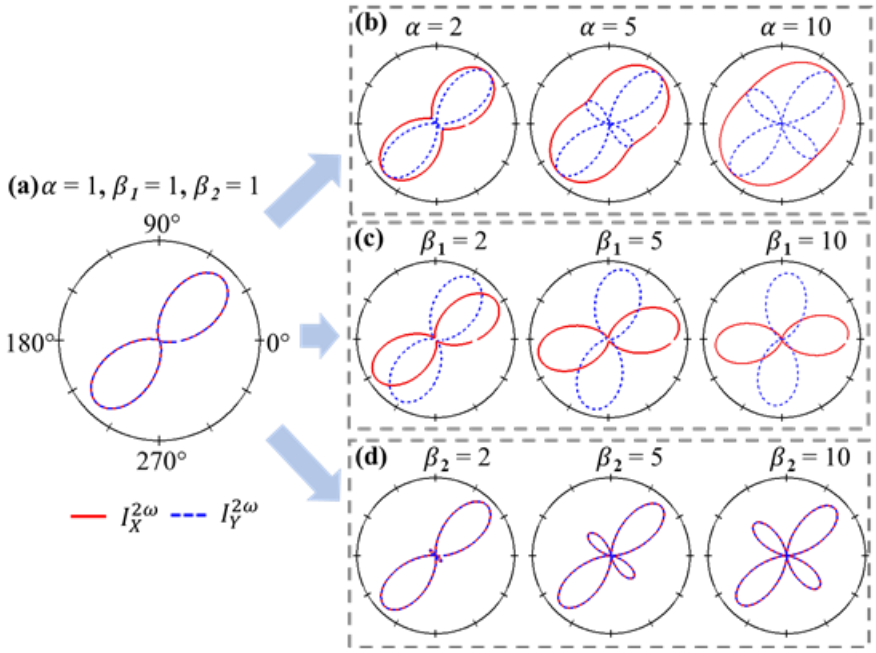

Figure 4.18. The calculated azimuthal $I_X^{2\omega}(\theta)$ and $I_Y^{2\omega}(\theta)$. α is the domain fraction factor; β_1 and β_2 are the ratios between the nonlinear coefficients. (a) $\alpha = 1$, $\beta_1 = 1$, and $\beta_2 = 1$. (b) α increases from 2 to 10. $\beta_1 = 1$ and $\beta_2 = 1$. (c) β_1 increases from 2 to 10. $\alpha = 1$ and $\beta_2 = 1$. (d) β_2 increases from 2 to 10. $\alpha = 1$ and $\beta_1 = 1$.

4.4.3 Experimental results and discussion

4.4.3.1 Epitaxial BTO-on-Si Thin Film Deposition

A 100 nm thick STO buffer layer was first deposited on a SOI substrate by PLD and then followed by the BTO deposition. The SOI substrate has a 70 nm thick Si device layer and a 2000 nm thick SiO_2 layer. The deposition was carried out at 20 mTorr O_2 and the substrate was heated at 700°C. The PLD was equipped with a λ = 248 nm KrF excimer laser with a 1.5 J/cm^2 fluence and a 5 Hz repetition rate.

4.4.3.2 Experimental Setup for Mid-IR SHG Characterization

The setup to characterize the SHG profile of a BTO-on-Si sample is illustrated in Fig. 4.19. The excitation light was from an optical parametric oscillators (OPO) laser with a 1 KHz pulse repetition rate and 10 cm^{-1} laser linewidths. A half-wave plate was placed right after the laser to control the polarization of the laser light. A filter transmitted light between λ = 3.25 and 3.75 μm was used to remove unwanted near-IR light from the OPO laser and also used as a beam splitter. After the filter, an objective lens was used to focus the incident light onto the BTO surface and also to collect the SHG signal from the sample. The laser light propagated in the *Z*-direction. The BTO-on-Si device was held onto a rotatable plate with an initial geometry of $X \,//\, [100]_{Si}$, $Y \,//\, [010]_{Si}$, and $Z \,//\, [001]_{Si}$, then rotated by an angle θ. A broadband polarizer was placed next to the filter that separated the two orthogonally polarized SHG, $I_X^{2\omega}$ and $I_Y^{2\omega}$. The extinction ratio of the wire-grid polarizer was 10:1. Another filter transmitted light at λ = 1.5 - 2.0 μm was placed between the lens and the detector to block the residual excitation laser light. The SHG signal collected at different azimuthal angle θ was monitored by the detector connected with an oscilloscope for analysis.

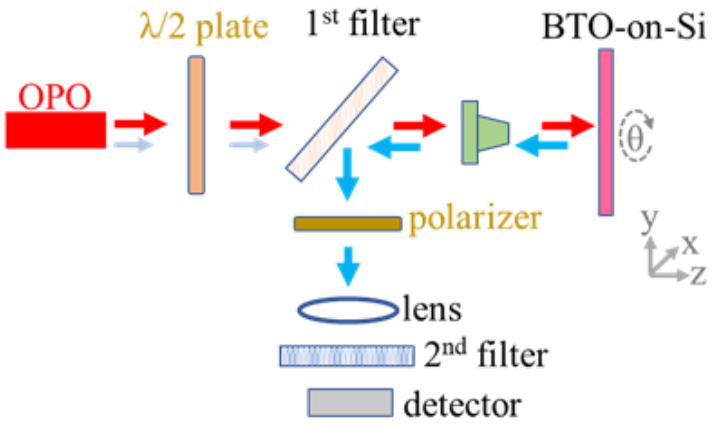

Fig. 4.19 The experimental setup to measure the azimuthal $I_X^{2\omega}(\theta)$ and $I_Y^{2\omega}(\theta)$ from the BTO-on-Si sample.

4.4.3.3 Measurement of Mid-IR Optical Nonlinearity and Domain Fraction Factor

Fig. 4 displays the azimuthal dependent SHG by rotating the BTO-on-Si sample with an angle θ, where $I_X^{2\omega}(\theta)$ and $I_Y^{2\omega}(\theta)$ present the SHG signals collected upon *X*-polarized and *Y*-polarized mid-IR excitation, respectively. For $I_X^{2\omega}(\theta)$ drawn in Fig. 4.20 (a), a four-lobed pattern with two main lobes point at θ = 45° and 225° are found. On the other hand, $I_Y^{2\omega}(\theta)$ drawn in Fig. 4.20 (b) shows a two-lobed profile. Comparing to the calculated SHG patterns in Fig. 4.18, the observed four-lobed $I_x^{2\omega}(\theta)$ and two-lobed $I_y^{2\omega}(\theta)$ indicate the BTO thin film has a large domain fraction factor. By fitting the polarimetric θ-dependent SHG, d_{15} = 9.5 pm/V, d_{31} = 5.4 pm/V, d_{33} = 15 pm/V, and $\Delta D^Y/\Delta D^X$= 24 was resolved. For bulk BTO crystal, it has optical nonlinear coefficients of d_{15} = 17 pm/V, d_{31} =15.7 pm/V, and d_{33} = 6.8 pm/V. The difference of the nonlinear coefficients between a bulk crystal and the epitaxial film is caused by the strain between the BTO and the Si layer. Other complex oxides like $BaZrO_3$ showed the same epitaxial strain during the thin film deposition [60].

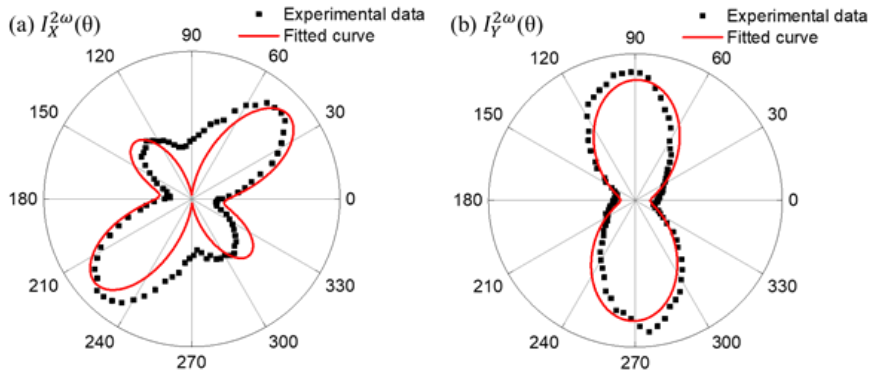

Fig. 4.20 The measured (a) $I_X^{2\omega}(\theta)$ and (b) $I_Y^{2\omega}(\theta)$ from the BTO-on-Si sample. d_{15} = 9.5 pm/V, d_{31} = 5.4 pm/V, d_{33} = 15 pm/V, and $\Delta D^Y/\Delta D^X$ = 24 were obtained from the fitting.

4.4.3.4 Mid-IR SHG vs. Excitation Laser Power and Wavelength

The SHG intensity at different excitation laser power was recorded and drawn in Fig. 4.21. The laser wavelength was fixed at λ = 3.5 μm and the power was gradually increased from 16 to 92 mW. $I_X^{2\omega}$ was measured at θ = 45° in Fig. 4.21 (a) because it reached its maximum according to Fig. 4.20 (a). Similarly, $I_Y^{2\omega}$ in Fig. 4.21 (b) was measured at its maximum at θ = 90°. Both $I_X^{2\omega}$ and $I_Y^{2\omega}$ plots show that the SHG intensity is linearly proportional to the square of the Mid-IR excitation light $(I^{\omega})^2$, which is the characteristic response from the 2nd order nonlinear optical process. Meanwhile, to measure the SHG spectrum, the detector in Fig. 4.19 was replaced by a spectrometer consisting of an InGaAs array. The excitation laser wavelength was adjusted from λ^{ω} = 3.0 to 3.6 μm, while the angle θ and the position of the BTO-on-Si remained the same. From Fig. 6, the SHG center wavelength consistently shifted from $\lambda^{2\omega}$ = 1.5 to 1.8 μm according to the excitation mid-IR wavelength. A wider SHG spectrum is found at $\lambda^{2\omega}$ < 1.6 μm because of the broadening of the excitation laser linewidth. The wide tuning range of the mid-IR SHG indicates the BTO-on-Si is a suitable platform to provide chip-scale light source.

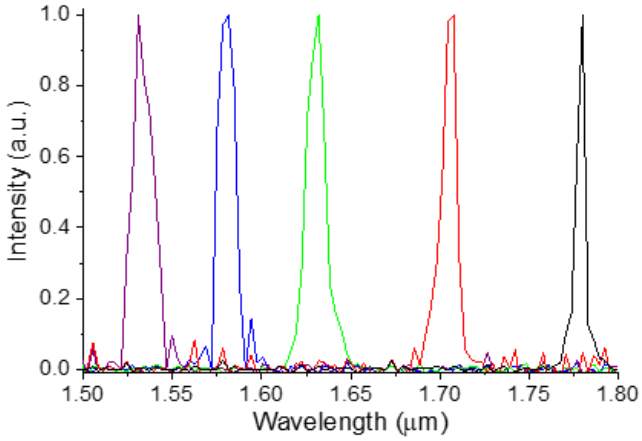

Fig. 4.21 The SHG spectrum of the BTO-on-Si sample when the pumping wavelength was shifted between λ^{ω} = 3.0 and 3.6 μm. Strong SHG was obtained over a broad spectrum.

4.4.4 Conclusions

Broadband mid-IR nonlinear light conversion was achieved by an epitaxial BTO-on-Si thin film from PLD. The azimuthal-dependent SHG patterns $I_x^{2\omega}(\theta)$ and $I_y^{2\omega}(\theta)$ were modelled at different ferroelectric domain fraction, α, and various ratio between the nonlinear coefficients, $\beta_{1,2}$. As α increases, the two-lobed $I_x^{2\omega}(\theta)$ pattern reshaped to an elliptic profile, while the two-lobed $I_y^{2\omega}(\theta)$ converted to a four-lobed profile. On the other hand, the increase of β_1 rotated the $I_x^{2\omega}(\theta)$ and $I_y^{2\omega}(\theta)$ patterns in the opposite direction. By fitting the experimental observed SHG patterns, we demonstrated that the grown BTO thin film possessed large 2nd order optical nonlinearity with d_{15} = 12.5 pm/V, d_{31} = 9.0 pm/V, and d_{33} = 10.0 pm/V, over a broad spectral range at λ = 3.0 - 3.6 μm. The monolithically integrated BTO-on-Si enables a platform for mid-IR nonlinear photonic circuits and optical quantum computing.

4.5 Preliminary study of optical parametric oscillation

4.5.1 Key elements of optical parametric oscillation

In an optical nonlinear medium, a strong pump wave at frequency ω_p may spontaneously break down into two lower-energy photons of frequency ω_1 and ω_2, that is $\omega_p = \omega_1 + \omega_2$. This three-wave mixing process is thus called the parametric down-conversion or optical parametric generation (OPG). Traditionally, among the two generated photons ω_1 and ω_2, the higher frequency (or the shorter wavelength) one is referred to as the *signal* and the lower frequency one (or the longer wavelength) is referred to as the *idler*. Spontaneous optical parametric generation is very weak if no certain frequency is emphasized. For practical applications of optical parametric generation, an optical resonance cavity is incorporated into the device to obtain a much higher output intensity and this device is called optical parametric oscillator (OPO), as shown in figure 4.22.

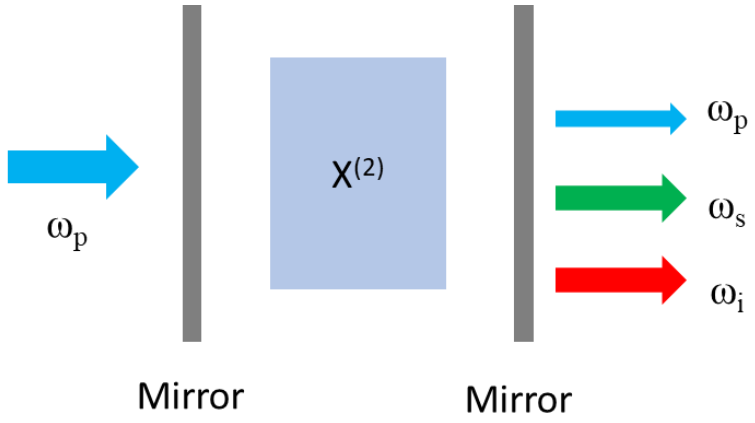

Figure 4.22 Optical parametric oscillator process

To achieve efficient OPOs, two critical conditions must also be satisfied. One is the energy conservation as shown by the break-down process $\omega_p = \omega_1 + \omega_2$. From the frequency relation equation, the frequency combination of the two generated photons is not unique. For a given ω_p, there can be a continuous range of frequency for ω_1 and ω_2, which is the fundamental of the

tunability of OPO light sources. However, in addition to the energy conservation condition, phase-matching is also required for efficient OPOs, i.e., $k_p = k_1 + k_2$, where k_p is the wavenumber of the pump wave and k_1, k_2 are the wavenumber of the two generated waves. When the phase-matching is perfectly fulfilled, the amplitude of the generated waves will grow linearly with the propagation distance because the newly generated light by ω_p is in phase with all the previous ω_1 and ω_2 as shown in Figure 4.23 (a). However, due to the dispersion of the nonlinear material, the phase velocities for different frequencies are not equal, leading to $k_p \neq k_1 + k_2$. After a coherence length $l_c = \pi / \Delta k$, $\Delta k = k_p - k_1 - k_2$, the pump and the generated waves walk out of phase with each other as shown in Figure 4. 23 (b).

To achieve phase matching for dispersive materials, there are mainly two techniques, birefringent phase-matching (BPM) and quasi-phase-matching (QPM). Briefly, BPM technique utilize the materials' birefringent characteristic to achieve the same refractive index value for the pump wave and the generated waves. As for QPM, a nonlinear crystal is periodically poled to have a periodic inversion of the sign of the nonlinear coefficient. The sign of the nonlinear coefficient is inverted after one coherence length and the pump wave would be in phase again with the generated waves every one coherence length as illustrated in Figure 4.23 (c).

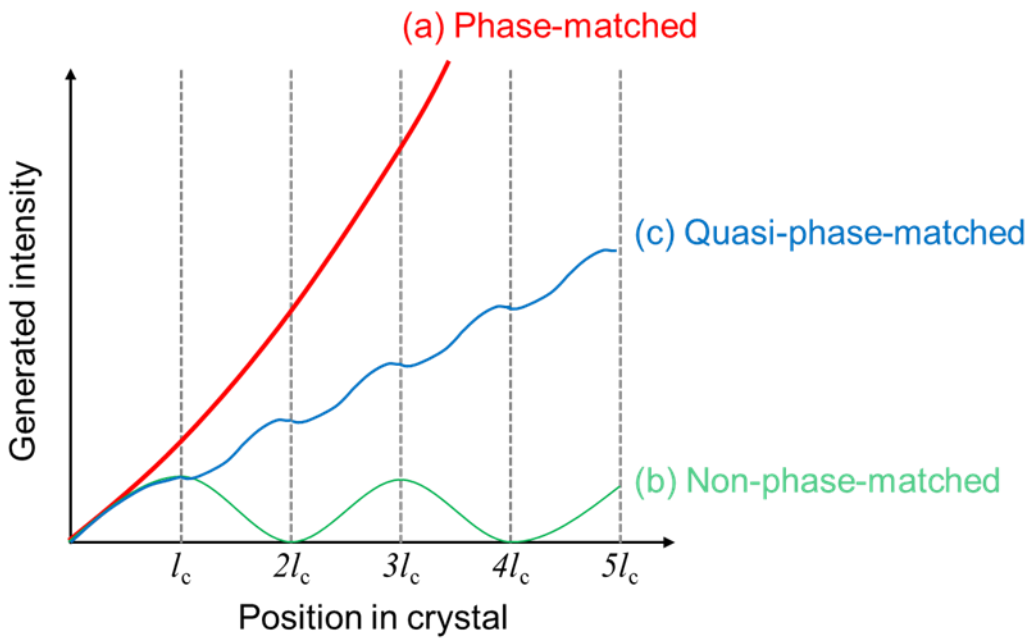

Figure 4.23 Illustration of the generated wave intensity as a function of propagation distance in a nonlinear medium for (a) perfectly phase-matched, (b) quasi-phase-matched, and (c) non-phase-matched.

4.5.2 Phase matching techniques

Birefringent phase-matching (BPM)

For a bulk nonlinear crystal, the birefringent phase-matching bis the most common technique to realize phase-matching condition. For a wave propagating through a birefringent material, the refractive index is not only dependent on the dispersion of the material but also dependent on the polarization and propagation direction of the wave. The refractive index differences between the pump wave and the generated waves can be compensated by adjusting the polarization and the propagation direction of the interacting waves.

In a nonlinear crystal, there is a special direction that governs the behavior of light, which is known as the optic axis. Any other directions perpendicular to the optic axis are all equivalent.

When the polarization of the light is perpendicular to the optic axis, the refractive index is independent of the propagation direction of the light. This refractive index is the *ordinary* refractive index, n_o. However, when the polarization of the light is parallel to the optic axis, the refractive index will be the extraordinary index n_e. Thus, the refractive index of the light will change between n_e and n_o, depending on the propagation direction. The simplest type of birefringence is the uniaxial birefringence where there is only one optic axis. The more complex type is the biaxial where there are two optic axes. To understand BPM, we can use uniaxial crystal as an example.

In a uniaxial nonlinear crystal, for a light that propagates with a relative angle θ against the optic axis, the refractive index n(θ) will change between n_e and n_o by the following equation:

$$\frac{1}{n^2(\theta)} = \frac{cos^2(\theta)}{n_o^2} + \frac{sin^2(\theta)}{n_e^2} \qquad (7.1)$$

The difference, $\Delta n(\theta) = n_e - n_o$ determines the birefringence of the material. Therefore, the refractive index not only depends on the frequency of light, but also on angle θ. It is possible to find a particular angle θ that will make $n(\omega)$ equal to $n(2\omega)$. Depends on the type of the nonlinear crystal (positive or negative), we can use ordinary wave for pump light and extraordinary wave for generated wave or vice versa. So, the pump wave is phase-matched to the generated wave. The birefringent phase matching is a low cost and efficient way to realize macroscopic output for OPOs using bulk crystals. However, the wavelength tuning range is limited by the birefringence of the material $\Delta n(\theta) = n_e - n_o$.

Quasi-phase matching

BPM, described in the previous section, is not always suitable for all circumstances although it is a very efficient way to achieve perfect phase-matching. These circumstances are when the

birefringence of the materials is small not enough to compensate for the refractive index difference due to dispersion or when the application requires to use the largest nonlinear coefficient of the material in the nonlinear interaction. BPM is also not suitable to achieve phase matching for light propagating in waveguides. Therefore, Armstrong *et al.* first suggest to use quasi-phase-matching (QPM) technique for those situations [61]. QPM is not aiming to compensate the refractive index difference due to dispersion but rather to manipulate generated waves to be in phase again with the pump waves by changing the sign of the nonlinear susceptibility tensor. Without QPM technique, the pump waves walk out of phase with the generated waves after a coherence length l_c. QPM is to reverse the sign of all the nonlinear susceptibility tensor of a nonlinear crystal after a coherence length l_c. Under this way, the induced polarization is shifted by 180° after each coherence length, making the interacting waves in phase again in the propagation direction. For materials like $LiNbO_3$, its spontaneous polarization can be easily reversed by applying an electric field. When a periodic pattern of electrode is fabricated on a LiNbO3 single crystal, periodic reversal of the ferroelectric domains of $LiNbO_3$ can be achieved. The period Λ is $2l_c$ as illustrated in figure 4.24 (a). Additionally, a fan-shaped pattern can be fabricated on the crystal allowing different poling periodicity on one crystal as shown in figure 4. 24 (b). For materials that cannot be easily poled by electric field like GaN, periodic reversal of the ferroelectric domains is achieved by growing the material with reversed polarity in a periodic pattern. Different from BPM, QPM allows the same polarization for all interacting waves, accessing the largest nonlinear coefficient of the nonlinear material. Thus, the conversion efficiency of QPM technique can be significantly higher than that by BPM technique. Because of the versatility of QPM technique, it is the most applicable way for micro-scale nonlinear devices to achieve a high nonlinear output.

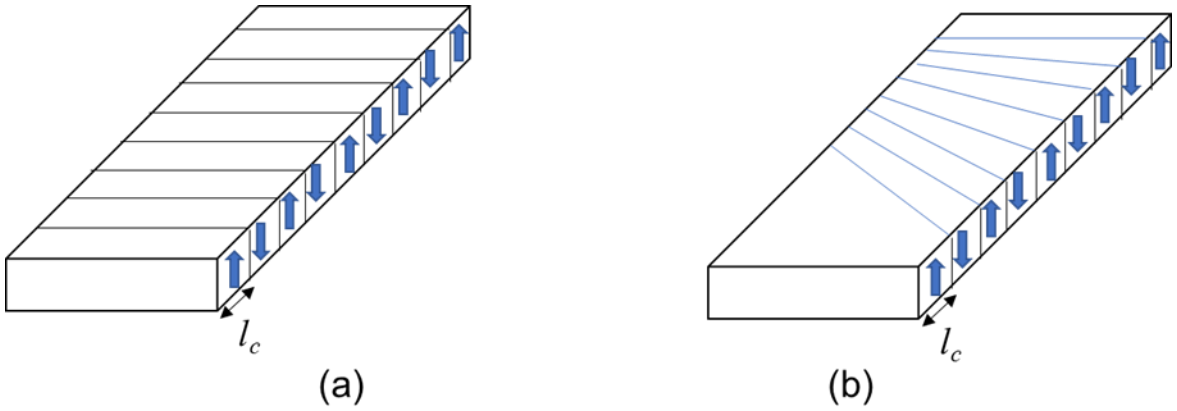

Figure 4. 24 (a) Linearly periodic poled of the nonlinear crystal, and (b) fan-shaped periodic poled of the nonlinear crystal.

Modal phase matching (waveguide or microring)

When light propagates in a waveguide, the confinement makes light form a unique distribution of the electrical and magnetic fields, i.e., waveguide mode. The effective refractive index for the waveguide mode at a certain wavelength is no longer the refractive index of the material, but will change according to the geometry of the waveguide and the mode order. Therefore, one can utilize the effective refractive index of waveguides to achieve phase-matching condition. By engineering the dimensions of the nanophotonic waveguide, phase-matching is possible between two or more wavelengths in a waveguide. This phase-matching technique is often referred to as modal phase matching. In Ref. [62], SHG was demonstrated by modal phase matching between the fundamental mode at 1550 nm and the higher-order mode at 775 nm in an AlN waveguide.

Phase matching in roto-inversion symmetry crystals

For crystals that have roto-inversion symmetry, their unit cell is inversed n times in a 360° turn for $\bar{n}$-fold symmetry. For example, GaAs has a zinc blende crystal structure which has $\bar{4}$-fold crystal symmetry, therefore its nonlinear susceptibility will be inversed after a 90° rotation. The inversion of the nonlinear susceptibility can produce quasi-phase matching in devices where light propagates around the crystal's vertical axis such as a micro-disk resonator or micro-ring resonators. The advantage of this method is the simplicity of device fabrication which doesn't require extra steps to do period poling of the crystal. However, the disadvantage is the efficiency is low since the domain is flipped only a few times for one turn.

4.5.3 Material Platform for chip-scale OPO devices

OPO is attractive for producing coherent light in Mid-IR range due to its wide tunability. A wide mid-IR spectrum provides the ability to differentiate multiple chemicals from their finger-print absorption. Current commercially available Mid-IR OPO lasers consist of a $\chi^{(2)}$ nonlinear crystal inserted in an optical cavity that is resonant for the pump wavelength as well as the generated signal and/or idler wavelengths. Depending on the property of the nonlinear crystal, OPO wavelengths tuning can be done via controlling the phase matching condition such as rotating the crystal angle[63], changing the crystal temperature[64], incorporating a fan-out periodic poling pattern[65], rotation of a diffraction grating[66], electro-optic shaping of the gain spectrum[67], or tuning the pump wavelength[68]. Although current OPO technology is mature for building widely-tunable mid-IR lasers, it relies on bulk nonlinear crystals and complex optical systems

which are not able to be miniaturized. For mid-IR molecular spectroscopy and chemical sensing applications, it is appealing to have an on-chip tunable mid-IR light source producing advantages of portability and in-situ measurement. However, it is still challenging to incorporate OPOs into integrated photonics where methods for phase-matching and resonant macroscopic output are limited.

To have OPOs in integrated photonics, nonlinear materials need to be fabricated into waveguiding structure. This requires engineering of wafer structures to have nonlinear crystal thin films on an under-cladding substrate. Nonlinear crystal thin films can then be fabricated into integrated photonic circuits by complementary metal-oxide-semiconductor (CMOS) compatible process. To have efficient OPO process, phase-matching condition is required for on-chip OPO devices. It is possible to use the effective indexes of waveguide modes to compensate the refractive indexes difference due to dispersion. Another way to realize phase-matching is to have periodic poling of the nonlinear crystal in the active region. Moreover, micro-resonant cavity is required to have practical macroscopic output for on-chip OPO devices.

When OPO devices scaled down to chip scale, bulk nonlinear crystals also need to be used of their thin film state. In addition, the nonlinear materials for chip-scale OPOs should be able to easily form waveguide devices with current nano/micro fabrication techniques. There are several nonlinear material platforms that meet these requirements such as III-V compounds and Perovskite oxides. Among III-V compounds, AlN, GaN, GaP and GaAs are potential candidates for on-chip OPOs. As for Perovskite oxides, $LiNbO_3$ and $BaTiO_3$ are the attractive materials for on-chip OPOs. A summary of the current second-order nonlinear optical photonic devices based on micro-resonators is shown in the table below:

III-V compounds

Aluminum nitride (AlN) emerged as a new material for nonlinear optics about a decade ago. Benefitted from a large bandgap (6.2 eV), AlN not only avoids two-photon absorption losses but also allows a wide transparency range from ultra-violet (UV) to mid-infrared wavelengths. AlN crystal has a non-centrosymmetric wurtzite structure thus exhibits second-order nonlinearity. M. C. Larciprete *et al.* reported a second order nonlinear coefficient d_{33} = 11 pm/V of AlN polycrystalline thin films grown by DC reactive sputtering in 2006 [69]. Later, A. W. Bruch demonstrated single-crystalline AlN waveguides with micro-ring resonators for second-harmonic generation (SHG) with high conversion efficiency in 2018 followed by OPO generation of NIR waves (around 1550nm) in 2019[70,71]. The single-crystalline AlN films deposited by metal-organic chemical vapor deposition (MOCVD) showed better performance than the polycrystalline AlN films deposited by sputtering. In such AlN micro-ring OPO devices, modal phase matching technique is applied meaning the mode of pump wave is phase matched to the mode of longer wavelengths. Tuning of wavelengths was achieved via changing the temperature.

Gallium nitride (GaN) is a wide bandgap (3.4 eV) material with a transparency window from about 365 nm to 13.6 μm, leading to a variety of applications in UV to visible to far infrared region. The second order nonlinear properties of GaN have been studied extensively since the thin film deposition of GaN in the early 1990s [72]. The second-order nonlinear susceptibility of GaN was reported to be around 16 pm/V [73]. Although photonic-circuits level demonstration of SHG by GaN micro-rings was achieved [74], OPO generation by GaN photonic circuits has not been reported yet. Lack of easily achievable phase matching technique limits the use of GaN for on-chip OPO devices. For quasi-phase matching, periodically-poled GaN is fabricated during growth process where the growth polarity can be controlled to be either Ga- (0001) or N-polar (000 $\bar{1}$) [75]. The surface roughness of the GaN thin film with periodic polarity limits the waveguide

performance due to scattering losses. Therefore, similar to AlN, modal dispersion phase-matching is a possible way for applications of GaN in integrated nonlinear photonics [76].

Gallium phosphide (GaP) and gallium arsenide (GaAs) are another two materials in III-V groups that can be used for nonlinear optics. The very high second order nonlinear coefficients of GaP (~ 100 pm/V [[77]) and GaAs (~ 200 pm/V [77]) make them very appealing for nonlinear optics. Quasi-phase matching for GaP and GaAs can be done during deposition process where inversions of the crystallographic orientation are grown into the material[78,79]. Additionally, a $\bar{4}$ symmetry structure of GaP and GaAs leads to an original quasi-phase matching condition on the orbital momentum of the fundamental and harmonic fields. In a $\bar{4}$-symmetry crystal, when light rotates around the $\bar{4}$ axis by 90°, the crystallographic orientation is also inverted, hence fields propagate around the $\bar{4}$ axis encounter four domain inversions per round trip. SHG for GaP and GaAs has been demonstrated in a whispering-gallery-mode resonator [80,81]. GaP integrated nonlinear devices with a combination of $\chi^{(2)}$ and $\chi^{(3)}$ process was demonstrated for different wavelength converters[82]. Despite the high optical nonlinearity of GaAs, the narrow bandgap (1.4 eV) of GaAs makes it suffer from two photon absorption and limits the wide-band integrated photonics.

Perovskite oxides

Because of the ferroelectric properties for most Perovskite oxides, periodic poling of the Perovskite oxide crystals can be done via applying a periodic electric field to meet quasi-phase matching condition for integrated nonlinear photonics.

Among all Perovskite oxides, Lithium niobate ($LiNbO_3$) has been deeply exploited for applications in nonlinear optics due to its high second order nonlinear coefficients (20 pm/V [83])

and low-cost crystal growth technique. Current $LiNbO_3$ thin films on insulators (LNOI) technology can provide high quality single crystalline $LiNbO_3$ thin films for integrated nonlinear photonics. Highly efficient and low pump threshold SHG and OPO device based on $LiNbO_3$ micro-rings was recently demonstrated [84,85]. Periodically poled $LiNbO_3$ micro-ring resonator was used to provide phase matching condition as well as the oscillation functionality for OPO generation. Wavelengths tuning of such micro-ring based OPO device is operated by controlling the temperature or pump wavelengths [85-88].

Barium titanate ($BaTiO_3$) is attractive for nonlinear optics due to its very high electro-optic coefficient (r_{42} ~ 1700 pm/V [89]) as well as the decent second order nonlinear susceptibility (~ 17pm/V). However, it is difficult to achieve thick high-quality $BaTiO_3$ thin films with smooth surface, limiting the waveguide performance. Direct formation of waveguide for $BaTiO_3$ is difficult since there is no efficient way to vertically etch $BaTiO_3$ thin films. A $BaTiO_3$ rib waveguide structure with a step height of 50 nm was demonstrated at 632 nm and 1550 nm for E-O modulation [90]. Another proposed geometry for $BaTiO_3$ nonlinear integrated photonics has a waveguide like Si or SiN on $BaTiO_3$ thin film, where a hybrid mode extends from the waveguide to the $BaTiO_3$ thin film [91]. However, the hybrid mode waveguide structure still suffers from high waveguide losses, which limits the efficiency for nonlinear processes.

Table 4.1 A summary of the 2nd-order nonlinear integrated photonic devices

Material	$\chi^{(2)}$ process	Device structure	Pump Wavelengths (nm)	Generated Wavelengths (nm)	References
AlN	SHG	Micro-ring	1550	775	70
	OPO	Micro-ring	780	Signal: 1480 Idler: 1650	71
GaN	SHG	Micro-ring	1560	780	74
	OPO	-	-	-	-
GaP	SHG	Micro-disk	1523	761.5	80
	OPO	Micro-ring	1550	Signal: 1540 Idler: 1580	82
GaAs	SHG	Micro-disk	1980	990	81
	OPO	-	-	-	-
LiNbO3	SHG	Micro-ring	1617	808	84
	OPO	Micro-ring	770	Signal: 1430 Idler: 1670	85
	OPO	Micro-disk	1080	Signal: 1500 - 2000 Idler: 2350 - 3800	86
	OPO	Micro-disk	532	Signal: 1010 Idler: 1120	87
	OPO	Micro-disk	488	Signal: 707 – 865 Idler: 1120 - 1575	88

4.5.4 Optical parametric amplification

As discussed in optical parametric oscillation, a resonance cavity is required to amplify the generated light intensity for macroscopic output. In integrated photonics, micro-rings are typically used as the resonant cavity. However, the fabrication of high-Q micro-rings is not that easy. A high-end electron-beam lithography system is required along with a good choice of e-beam resist to fabricate micro-rings with smooth edges. The gap between the micro-ring and the bus waveguide needs to be well chosen for the short-wavelength pump beam and longer wavelength signal and idler beams, respectively. To full-fill the phase matching condition, a periodic polling on the micro-ring is needed, which requires fabrication of electrodes aligned on the micro-rings. Due to the difficulty of micro-ring fabrication, an alternative way to demonstrate optical parametric generation into mid-infrared region is through optical parametric amplification, as shown in figure 4.25. A pump beam ω_p is focused into a nonlinear $\chi^{(2)}$ material along with a seed signal wave ω_s. Idler wave ω_i is generated through the process of difference-frequency generation:

$$\omega_i = \omega_p - \omega_s \tag{6.1}$$

$$P(\omega_p - \omega_s) = 2\chi^{(2)} E_p E_s^*$$

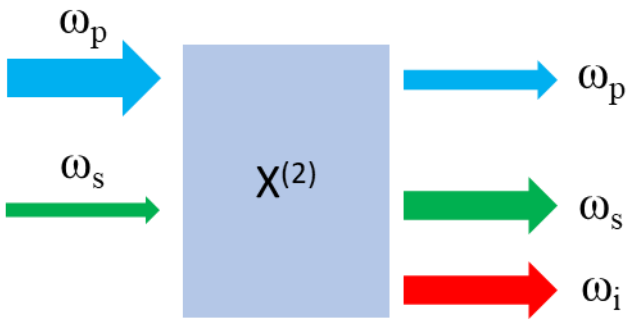

Figure 4.25 Optical parametric amplifier process

The OPA process will convert the pump wave to signal and idler waves, amplifying the signal beam and also creating a new idler beam. In an OPA device, a resonance cavity is not needed. The

light just passes straight through the nonlinear material. Phase-matching is still required for OPA to achieve efficient frequency conversion. The overall gain is dependent on the total length of the device.

4.5.5 Experimental setup for OPA from TiO_2 waveguide on periodically poled $LiNbO_3$

The experimental setup for optical parametric amplification is shown in figure 4.26. A pulsed 1064 nm laser is used as the pump and a 1550 nm CW-laser acts as the signal seed. The 1064 nm laser is first reflected by a mirror and then merged with the 1550 nm CW-laser on the 1300 nm long-pass filter (LPF), which can reflect the 1064 nm wave and let 1550 nm wave transmit through. Both the pump wave and the signal seed wave are focused to the TiO_2 waveguide on $LiNbO_3$ substrate by an objective lens. The light output from the TiO_2 waveguide is focused onto a photodetector. A filter is placed before the photodetector to filter out the 1064 nm pump beam and 1550 nm laser signal beam while only let the long wavelength idler beam to pass through.

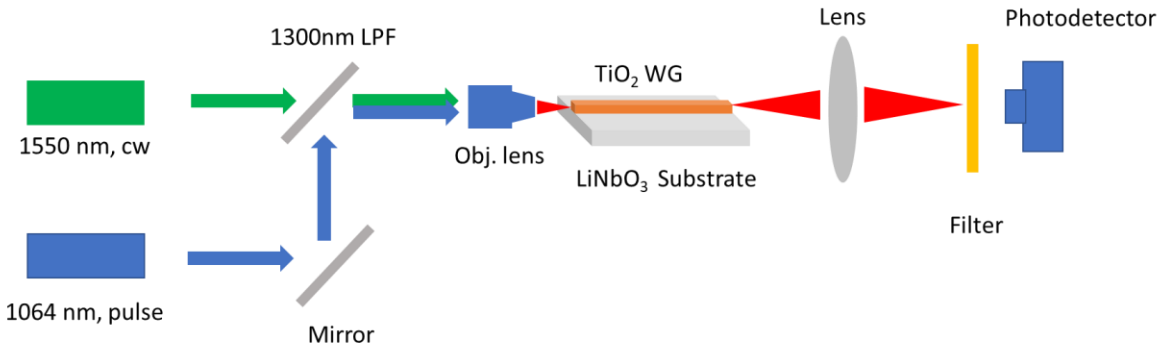

Figure 4.26 Experimental setup for OPA process

The x-cut $LiNbO_3$ substrate under the TiO_2 waveguide is periodically poled for quasi-phase matching. Figure 4.27 (a) shows a schematic for periodically poling the $LiNbO_3$ substrate. The TiO_2 waveguide is perpendicular to the Z axis of the $LiNbO_3$. The direction of the positive to negative electrode is along -Z direction of the $LiNbO_3$ substrate. Chromium positive and negative

electrode with periodic fringes were fabricated on the $LiNbO_3$ by Nanoscribe 3D patterning technique. First, a periodic fringes pattern of IP-Dip resin was written by the Nanoscribe 3D direct-writing. Then, chromium was deposited on the chip by e-beam evaporation. Last, the periodic chromium fringes electrode pattern was obtained by the IP-Dip resin lift-off. The width of the TiO_2 waveguide is about 15 μm. The gap between the positive and negative electrode fringes is 20 μm. The domain of the $LiNbO_3$ is revered by applying a voltage of 300V in the -Z direction. Figure 4.27 (b) shows an image of the periodic poling setup.

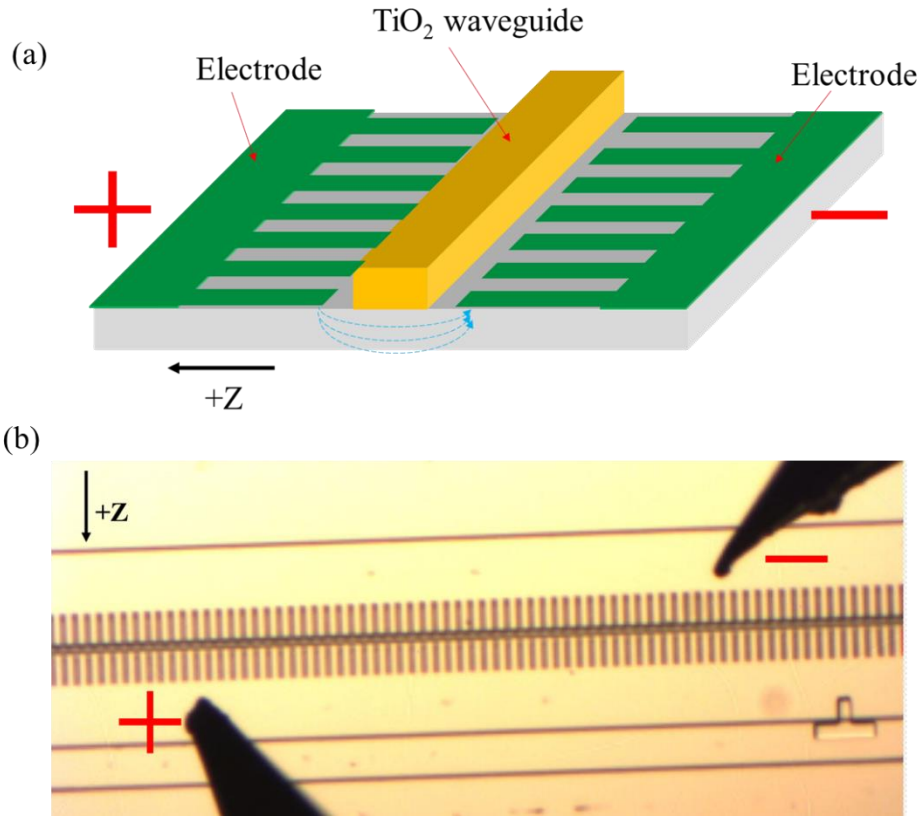

Figure 4.27 (a) A schematic of the periodic poling of the $LiNbO_3$ substrate under the TiO_2 waveguide; (b) An image of the periodic poling setup.

4.6 References

[1] R. E. Cohen, “Origin of ferroelectricity in perovskite oxides,” *Nature*, vol. 358, no. 6382, pp. 136-138, 1992.

[2] L. Arizmendi, “Photonic applications of lithium niobate crystals,” *Physica Status Solidi (a)*, vol. 201, no. 2, pp. 253-283, 2004.

[3] X. Liang *et al.*, "Compact chirped pulse optical parametric amplifier in periodically poled $LiTaO_3$," in *2005 Quantum Electronics and Laser Science Conference*, 2005, vol. 3: IEEE, pp. 1636-1638.

[4] A. Hermans *et al.*, "On the determination of $\chi(2)$ in thin films: a comparison of one-beam second-harmonic generation measurement methodologies," *Sci. Rep.*, vol. 7, no. 1, pp. 1-13, 2017.

[5] L. E. Myers *et al.*, "Quasi-phase-matched optical parametric oscillators in bulk periodically poled $LiNbO_3$," *JOSA B*, vol. 12, no. 11, pp. 2102-2116, 1995.

[6] M. A. Belkin *et al.*, "Terahertz quantum-cascade-laser source based on intracavity difference-frequency generation," *Nature Photonics*, vol. 1, no. 5, pp. 288-292, 2007.

[7] X. Lu *et al.*, "Chip-integrated visible–telecom entangled photon pair source for quantum communication," *Nature physics*, vol. 15, no. 4, pp. 373-381, 2019.

[8] I. Marinković *et al.*, "Hybrid integration of silicon photonic devices on lithium niobate for optomechanical wavelength conversion," *Nano Lett.*, vol. 21, no. 1, pp. 529-535, 2021.

[9] A. J. Mercante *et al.*, "110 GHz CMOS compatible thin film $LiNbO_3$ modulator on silicon," *Opt. Express*, vol. 24, no. 14, pp. 15590-15595, 2016.

[10] N. Setter *et al.*, “Ferroelectric thin films: Review of materials, properties, and applications,” *J. Appl. Phys.*, vol. 100, no. 5, pp. 051606, 2006.

[11] W. Lee *et al.*, “Flexible graphene–PZT ferroelectric nonvolatile memory,” *Nanotechnology*, vol. 24, no. 47, pp. 475202, 2013.

[12] J. Wang *et al.*, “Epitaxial $BiFeO_3$ multiferroic thin film heterostructures,” *Science*, vol. 299, no. 5613, pp. 1719-1722, 2003.

[13] K. Suzuki *et al.*, “Ferroelectric property of alkoxy-derived $YMnO_3$ films crystallized in argon,” *JPN J. Appl. Phys.*, vol. 42, no. 9R, pp. 5692, 2003.

[14] S. Raghavan *et al.*, “High-mobility $BaSnO_3$ grown by oxide molecular beam epitaxy,” *APL Mater.*, vol. 4, no. 1, pp. 016106, 2016.

[15] E. Østreng *et al.*, “Atomic layer deposition of ferroelectric $LiNbO_3$,” *J. Mater. Chem. C*, vol. 1, no. 27, pp. 4283-4290, 2013.

[16] Y. Garbovskiy, and A. Glushchenko, "Optical/ferroelectric characterization of $BaTiO_3$ and $PbTiO_3$ colloidal nanoparticles and their applications in hybrid materials technologies," *Appl. Opt.,* vol. 52, no. 22, pp. E34-E39, 2013.

[17] M. K. Trivedi *et al.*, "Impact of biofield treatment on atomic and structural characteristics of barium titanate powder," *Ind. Eng. Manag.,* vol. 4, no. 3, pp. 1000166, 2015.

[18] P. Lin, Z. Liu, and B. W. Wessels, "Ferroelectric thin film photonic crystal waveguide and its electro-optic properties," *J. Opt. A: Pure Appl. Opt.,* vol. 11, no. 7, pp. 075005, 2009.

[19] A. Petraru *et al.*, "Ferroelectric $BaTiO_3$ thin-film optical waveguide modulators," *Appl. Phys. Lett.,* vol. 81, no. 8, pp. 1375-1377, 2002.

[20] T. Zhao *et al.*, "Stress-induced enhancement of second-order nonlinear optical susceptibilities of barium titanate films," *J. Appl. Phys.,* vol. 87, no. 10, pp. 7448-7451, 2000.

[21] M. B. Lee *et al.*, "Heteroepitaxial growth of $BaTiO_3$ films on Si by pulsed laser deposition," *Appl. Phys. Lett.,* vol. 66, no. 11, pp. 1331-1333, 1995.

[22] M.-H. M. Hsu *et al.*, "Controlled orientation of molecular-beam-epitaxial BaTiO3 on Si (001) using thickness engineering of $BaTiO_3$ and $SrTiO_3$ buffer layers," *Appl. Phys. Express,* vol. 10, no. 6, pp. 065501, 2017.

[23] S. Vura *et al.*, "Epitaxial $BaTiO_3$ on Si (100) with In-Plane and Out-of-Plane Polarization Using a Single TiN Transition Layer," *ACS Appl. Electron. Mater.,* vol. 3, no. 2, pp. 687-695, 2021.

[24] A. Meier, F. Niu, and B. Wessels, "Integration of $BaTiO_3$ on Si (001) using MgO/STO buffer layers by molecular beam epitaxy," *J Cryst. Growth,* vol. 294, no. 2, pp. 401-406, 2006.

[25] R. E. Cohen, "Origin of ferroelectricity in perovskite oxides," Nature, vol. 358, no. 6382, pp. 136-138, 1992.

[26] L. Arizmendi, "Photonic applications of lithium niobate crystals," Physica Status Solidi (a), vol. 201, no. 2, pp. 253-283, 2004.

[27] X. Liang et al., "Compact chirped pulse optical parametric amplifier in periodically poled LiTaO3," in 2005 Quantum Electronics and Laser Science Conference, 2005, vol. 3: IEEE, pp. 1636-1638.

[28] A. Hermans et al., "On the determination of $\chi(2)$ in thin films: a comparison of one-beam second-harmonic generation measurement methodologies," Sci. Rep., vol. 7, no. 1, pp. 1-13, 2017.

[29] L. E. Myers et al., "Quasi-phase-matched optical parametric oscillators in bulk periodically poled LiNbO3," JOSA B, vol. 12, no. 11, pp. 2102-2116, 1995.

[30] M. A. Belkin et al., "Terahertz quantum-cascade-laser source based on intracavity difference-

frequency generation," Nature Photonics, vol. 1, no. 5, pp. 288-292, 2007.

[31] X. Lu et al., "Chip-integrated visible–telecom entangled photon pair source for quantum communication," Nature physics, vol. 15, no. 4, pp. 373-381, 2019.

[32] I. Marinković et al., "Hybrid integration of silicon photonic devices on lithium niobate for optomechanical wavelength conversion," Nano Lett., vol. 21, no. 1, pp. 529-535, 2021.

[33] A. J. Mercante et al., "110 GHz CMOS compatible thin film LiNbO3 modulator on silicon," Opt. Express, vol. 24, no. 14, pp. 15590-15595, 2016.

[34] N. Setter et al., "Ferroelectric thin films: Review of materials, properties, and applications," J. Appl. Phys., vol. 100, no. 5, pp. 051606, 2006.

[35] W. Lee et al., "Flexible graphene–PZT ferroelectric nonvolatile memory," Nanotechnology, vol. 24, no. 47, pp. 475202, 2013.

[36] J. Wang et al., "Epitaxial BiFeO3 multiferroic thin film heterostructures," Science, vol. 299, no. 5613, pp. 1719-1722, 2003.

[37] K. Suzuki et al., "Ferroelectric property of alkoxy-derived YMnO3 films crystallized in argon," JPN J. Appl. Phys., vol. 42, no. 9R, pp. 5692, 2003.

[38] S. Raghavan et al., "High-mobility BaSnO3 grown by oxide molecular beam epitaxy," APL Mater., vol. 4, no. 1, pp. 016106, 2016.

[39] E. Østreng et al., "Atomic layer deposition of ferroelectric LiNbO3," J. Mater. Chem. C, vol. 1, no. 27, pp. 4283-4290, 2013.

[40] Y. Garbovskiy, and A. Glushchenko, "Optical/ferroelectric characterization of BaTiO3 and PbTiO3 colloidal nanoparticles and their applications in hybrid materials technologies," Appl. Opt., vol. 52, no. 22, pp. E34-E39, 2013.

[41] M. K. Trivedi et al., "Impact of biofield treatment on atomic and structural characteristics of barium titanate powder," Ind. Eng. Manag., vol. 4, no. 3, pp. 1000166, 2015.

[42] P. Lin, Z. Liu, and B. W. Wessels, "Ferroelectric thin film photonic crystal waveguide and its electro-optic properties," J. Opt. A: Pure Appl. Opt., vol. 11, no. 7, pp. 075005, 2009.

[43] A. Petraru et al., "Ferroelectric BaTiO3 thin-film optical waveguide modulators," Appl. Phys. Lett., vol. 81, no. 8, pp. 1375-1377, 2002.

[44] T. Zhao et al., "Stress-induced enhancement of second-order nonlinear optical susceptibilities of barium titanate films," J. Appl. Phys., vol. 87, no. 10, pp. 7448-7451, 2000.

[45] M. B. Lee et al., "Heteroepitaxial growth of BaTiO3 films on Si by pulsed laser deposition," Appl. Phys. Lett., vol. 66, no. 11, pp. 1331-1333, 1995.

[46] M.-H. M. Hsu et al., "Controlled orientation of molecular-beam-epitaxial BaTiO3 on Si (001) using thickness engineering of BaTiO3 and SrTiO3 buffer layers," Appl. Phys. Express, vol. 10, no. 6, pp. 065501, 2017.

[47] S. Vura et al., "Epitaxial BaTiO3 on Si (100) with In-Plane and Out-of-Plane Polarization Using a Single TiN Transition Layer," ACS Appl. Electron. Mater., vol. 3, no. 2, pp. 687-695, 2021.

[48] A. Meier, F. Niu, and B. Wessels, "Integration of BaTiO3 on Si (001) using MgO/STO buffer layers by molecular beam epitaxy," J Cryst. Growth, vol. 294, no. 2, pp. 401-406, 2006.

[49] T. Zhao et al., "Enhancement of second-harmonic generation in BaTiO3/SrTiO3 superlattices," Phys. Rev. B, vol. 60, no. 3, pp. 1697, 1999.

[50] E. Kim et al., "Second-harmonic generation of single BaTiO3 nanoparticles down to 22 nm diameter," ACS Nano, vol. 7, no. 6, pp. 5343-5349, 2013.

[51] B. Bihari, J. Kumar, G. T. Stauf et al., "Investigation of barium titanate thin films on MgO substrates by second-harmonic generation," J. Appl. Phys., vol. 76, no. 2, pp. 1169-1174, 1994.

[52] T. Jin et al., "Mid-infrared chalcogenide waveguides for real-time and nondestructive volatile organic compound detection," Anal. Chem., vol. 91, no. 1, pp. 817-822, 2018.

[53] J. Zhou, and P. T. Lin, "Midinfrared Multispectral Detection for Real-Time and Noninvasive Analysis of the Structure and Composition of Materials," ACS Sensors, vol. 3, no. 7, pp. 1322-1328, 2018.

[54] P. T. Lin et al., "Label-free glucose sensing using chip-scale mid-infrared integrated photonics," Adv. Opt. Mater., vol. 4, no. 11, pp. 1755-1759, 2016.

[55] A. Lochbaum et al., "On-chip narrowband thermal emitter for mid-IR optical gas sensing," ACS Photonics, vol. 4, no. 6, pp. 1371-1380, 2017.

[56] S. Borri et al., "High-precision molecular spectroscopy in the mid-infrared using quantum cascade lasers," Appl. Phys. B, vol. 125, no. 1, pp. 1-9, 2019.

[57] Q. Hao et al., "Mid-infrared transmitter and receiver modules for free-space optical communication," Appl. Opt., vol. 56, no. 8, pp. 2260-2264, 2017.

[58] H. D. Megaw, "Origin of ferroelectricity in barium titanate and other perovskite-type crystals," Acta Crystallographica, vol. 5, no. 6, pp. 739-749, 1952.

[59] S. A. Denev et al., "Probing ferroelectrics using optical second harmonic generation," J. Am. Ceram. Soc., vol. 94, no. 9, pp. 2699-2727, 2011.

[60] O. Diéguez, K. M. Rabe, and D. Vanderbilt, "First-principles study of epitaxial strain in perovskites," Phys. Rev. B, vol. 72, no. 14, pp. 144101, 2005.

[61] Armstrong, J. A., N. Bloembergen, J. Ducuing, and Peter S. Pershan. "Interactions between light waves in a nonlinear dielectric." Physical review 127, no. 6 (1962): 1918.

[62] Pernice, W. H. P., C. Xiong, C. Schuck, and H. X. Tang. "Second harmonic generation in phase matched aluminum nitride waveguides and micro-ring resonators." *Applied Physics Letters* 100, no. 22 (2012): 223501.

[63] Kafka, J. D., M. L. Watts, J. W. Pieterse, and R. L. Herbst. "Mid-infrared pulse generation using a sub-picosecond OPO." Applied Physics B 60, no. 5 (1995): 449-452.

[64] Haidar, S., E. Niwa, K. Masumoto, and H. Ito. "Temperature tuning of 5–12 μm by difference frequency mixing of OPO outputs in a AgGaS2 crystal." *Journal of Physics D: Applied Physics* 36, no. 9 (2003): 1071.

[65] Powers, P. E., Thomas J. Kulp, and S. E. Bisson. "Continuous tuning of a continuous-wave periodically poled lithium niobate optical parametric oscillator by use of a fan-out grating design." *Optics letters* 23, no. 3 (1998): 159-161.

[66] Vainio, Markku, Mikael Siltanen, Jari Peltola, and Lauri Halonen. "Continuous-wave optical parametric oscillator tuned by a diffraction grating." *Optics express* 17, no. 9 (2009): 7702-7707.

[67] Gross, P., M. E. Klein, H. Ridderbusch, D-H. Lee, J-P. Meyn, R. Wallenstein, and K-J. Boller. "Wide wavelength tuning of an optical parametric oscillator through electro-optic shaping of the gain spectrum." *Optics letters* 27, no. 16 (2002): 1433-1435.

[68] Siltanen, Mikael, Markku Vainio, and Lauri Halonen. "Pump-tunable continuous-wave singly resonant optical parametric oscillator from 2.5 to 4.4 μm." *Optics express* 18, no. 13 (2010): 14087-14092.

[69] Larciprete, M. C., A. Bosco, A. Belardini, R. Li Voti, G. Leahu, C. Sibilia, E. Fazio et al. "Blue second harmonic generation from aluminum nitride films deposited onto silicon by sputtering technique." *Journal of applied physics* 100, no. 2 (2006): 023507.

[70] Bruch, Alexander W., Xianwen Liu, Xiang Guo, Joshua B. Surya, Zheng Gong, Liang Zhang, Junxi Wang, Jianchang Yan, and Hong X. Tang. "17 000%/W second-harmonic conversion efficiency in single-crystalline aluminum nitride microresonators." *Applied Physics Letters* 113, no. 13 (2018): 131102.

[71] Bruch, Alexander W., Xianwen Liu, Joshua B. Surya, Chang-Ling Zou, and Hong X. Tang. "On-chip χ (2) microring optical parametric oscillator." *Optica* 6, no. 10 (2019): 1361-1366.

[72] Miragliotta, J., D. K. Wickenden, T. J. Kistenmacher, and W. A. Bryden. "Linear-and nonlinear-optical properties of GaN thin films." *JOSA B* 10, no. 8 (1993): 1447-1456.

[73] Zhang, H. Y., X. H. He, Y. H. Shih, M. Schurman, Z. C. Feng, and R. A. Stall. "Study of nonlinear optical effects in GaN: Mg epitaxial film." *Applied physics letters* 69, no. 20 (1996): 2953-2955.

[74] Xiong, Chi, Wolfram Pernice, Kevin K. Ryu, Carsten Schuck, King Y. Fong, Tomas Palacios, and Hong X. Tang. "Integrated GaN photonic circuits on silicon (100) for second harmonic generation." *Optics express* 19, no. 11 (2011): 10462-10470.

[75] Chowdhury, Aref, Hock M. Ng, Manish Bhardwaj, and Nils G. Weimann. "Second-harmonic generation in periodically poled GaN." *Applied physics letters* 83, no. 6 (2003): 1077-1079.

[76] Hahn, D. N., G. T. Kiehne, J. B. Ketterson, G. K. L. Wong, P. Kung, A. Saxler, and M. Razeghi. "Phase-matched optical second-harmonic generation in GaN and AlN slab waveguides." *Journal of applied physics* 85, no. 5 (1999): 2497-2501.

[77] Dal Corso, Andrea, Francesco Mauri, and Angel Rubio. "Density-functional theory of the nonlinear optical susceptibility: Application to cubic semiconductors." *Physical Review B* 53, no. 23 (1996): 15638.

[78] Vodopyanov, K. L., M. M. Fejer, X. Yu, J. S. Harris, Y-S. Lee, Walter C. Hurlbut, V. G. Kozlov, D. Bliss, and C. Lynch. "Terahertz-wave generation in quasi-phase-matched GaAs." *Applied Physics Letters* 89, no. 14 (2006): 141119.

[79] Maidment, Luke, Oguzhan Kara, Peter G. Schunemann, Jonathon Piper, Kenneth McEwan, and Derryck T. Reid. "Long-wave infrared generation from femtosecond and picosecond optical parametric oscillators based on orientation-patterned gallium phosphide." *Applied Physics B* 124, no. 7 (2018): 1-8.

[80] Guillemé, Pierre, Yannick Dumeige, Julien Stodolna, Maxime Vallet, Tony Rohel, Antoine Létoublon, Charles Cornet, Anne Ponchet, Olivier Durand, and Yoan Léger. "Second harmonic generation in gallium phosphide microdisks on silicon: from strict to random quasi-phase matching." *Semiconductor Science and Technology* 32, no. 6 (2017): 065004.

[81] Kuo, Paulina S., Jorge Bravo-Abad, and Glenn S. Solomon. "Second-harmonic generation using-quasi-phasematching in a GaAs whispering-gallery-mode microcavity." *Nature communications* 5, no. 1 (2014): 1-7.

[82] Wilson, Dalziel J., Katharina Schneider, Simon Hönl, Miles Anderson, Yannick Baumgartner, Lukas Czornomaz, Tobias J. Kippenberg, and Paul Seidler. "Integrated gallium phosphide nonlinear photonics." *Nature Photonics* 14, no. 1 (2020): 57-62.

[83] Schiek, Roland, and Thomas Pertsch. "Absolute measurement of the quadratic nonlinear susceptibility of lithium niobate in waveguides." *Optical Materials Express* 2, no. 2 (2012): 126-139.

[84] Lu, Juanjuan, Joshua B. Surya, Xianwen Liu, Alexander W. Bruch, Zheng Gong, Yuntao Xu, and Hong X. Tang. "Periodically poled thin-film lithium niobate microring resonators with a second-harmonic generation efficiency of 250,000%/W." *Optica* 6, no. 12 (2019): 1455-1460.

[85] Lu, Juanjuan, Ayed Al Sayem, Zheng Gong, Joshua B. Surya, Chang-Ling Zou, and Hong X. Tang. "Ultralow-threshold thin-film lithium niobate optical parametric oscillator." *Optica* 8, no. 4 (2021): 539-544.

[86] Herr, Simon J., Christoph S. Werner, Karsten Buse, and Ingo Breunig. "Quasi-phase-matched self-pumped optical parametric oscillation in a micro-resonator." Optics express 26, no. 8 (2018): 10813-10819.

[87] Fürst, J. U., D. V. Strekalov, D. Elser, A. Aiello, Ulrik Lund Andersen, Ch Marquardt, and G. Leuchs. "Low-threshold optical parametric oscillations in a whispering gallery mode resonator." Physical review letters 105, no. 26 (2010): 263904.

[88] Werner, Christoph Sebastian, Tobias Beckmann, Karsten Buse, and Ingo Breunig. "Blue-pumped whispering gallery optical parametric oscillator." Optics letters 37, no. 20 (2012): 4224-4226.

[89] Johnston, Alan R., and J. M. Weingart. "Determination of the low-frequency linear electro-optic effect in tetragonal BaTiO 3." *JOSA* 55, no. 7 (1965): 828-834.

[90] Petraru, A., J. Schubert, M. Schmid, and Ch Buchal. "Ferroelectric BaTiO 3 thin-film optical waveguide modulators." *Applied Physics Letters* 81, no. 8 (2002): 1375-1377.

[91] Eltes, Felix, Daniele Caimi, Florian Fallegger, Marilyne Sousa, Eamon O'Connor, Marta D. Rossell, Bert Offrein, Jean Fompeyrine, and Stefan Abel. "Low-loss BaTiO3–Si waveguides for nonlinear integrated photonics." *Acs Photonics*3, no. 9 (2016): 1698-1703.

CHAPTER V

MID-IR DETECTION OF VOLATILE ORGANIC COMPOUNDS BASED ON SILICON AND SILICON NITRIDE WAVEGUIDES

5.1 Introduction

Detection of VOC gases has attracted significant attention because it is critical for applications of non-invasive health monitoring, plant disease diagnostics, industrial leak detection, etc [1-5]. Two general approaches have been used for VOC analysis, analytical techniques such as gas chromatography mass spectrometry (GC-MS) [6,7], and solid-state sensors, such as metal-oxide semiconductors (MOS) sensors [8-10], electrochemical (EC) sensors [11], and photoionization detectors (PID) [12]. GC-MS can provide accurate gas analysis, but the system is bulky and is thus unsuitable for POU and real-time applications. Solid state chemical sensors like MOS, EC, and PID have shown high sensitivity and portability but have low selectivity to differentiate among VOCs. As an alternative to conventional solid-state sensors, mid-IR sensing can provide high selectivity by measuring absorption in the characteristic and finger-print vibrational features of VOCs. However, mid-IR absorption spectroscopy requires bench-top optical equipment such as Fourier-transform infrared spectroscopy (FTIR), which are unpractical for POU applications [13,14]. To address this issue, miniaturized photonic circuits consisting of optical waveguides and other chip-scale photonic components have been explored [15-17]. However, prior approaches have used waveguide materials that have high refractive indices, such as Si and Ge [18,19], which lead to a weak evanescent wave [20,21] and therefore poor sensitivity. Chalcogenide materials have also been used [22], and they provide stronger evanescent fields, but they are prone to degradation upon exposure to moisture, thus requiring storage under dry N_2 or high vacuum condition. To address this issue, the present study examines the use of SiN as the waveguide

material. SiN has a low refractive index ($\mathbf{n_{SiN}}$ = 1.94) compared to Si ($\mathbf{n_{Si}}$ = 3.4) or Ge ($\mathbf{n_{Ge}}$ = 4.0), which leads to a strong evanescent wave and therefore higher sensitivity, and also possesses exceptional chemical stability and can be repeatedly used in ambient humidity conditions [23,24] Further, SiN has a broad infrared transparency window, low optical loss, and high compatibility with complementary metal-oxide-semiconductor (CMOS) processes [25,26]. These properties make SiN an ideal material for waveguide sensors to enable repeatable, reproducible VOCs detection over long-term sensing operation. To our knowledge, however, prior work on SiN as a waveguide material has been primarily theoretical or has focused on wavelength sensing in the visible range, rather than the far more informative mid-IR range [27-29].

To demonstrate the potential of SiN waveguide sensing for mid-IR detection of gaseous analytes, here we focused on three VOCs (acetone, ethanol, and isoprene) that are potential biomarkers for breath analysis. For instance, exhaled acetone has been studied to monitor diabetic ketoacidosis [30,31], ethanol for alcohol abstinence [32], and isoprene for lung cancer and high blood cholesterol [33,34]. Further, these VOCs have strong mid-IR absorption signatures at wavelengths between 3.0 - 3.6 μm, which are detectable using the proposed SiN photonic circuits. Being compatible with CMOS fabrication processes, the proposed SiN mid-IR waveguide sensor offers the potential for a compact device platform to realize real-time gas analysis.

5.2 Basic concept of waveguide sensing

The light is guided in a waveguide by total internal reflection. At the interface, the light is reflected back into the waveguide and on the other side of the interface, there is an electro magnetic field that decays exponentially away from the interface. The decay waves outside of the waveguide is called evanescent waves. Figure 5.1 shows a schematic of the evanescent wave surrounding the waveguide. When the medium surrounding the waveguide is lossy, the propagating light in the waveguide will lose some energy each time it bounces back at the interface. The absorbance of the waveguide will obey Beer-Lambert law, which relates the attenuation of light to the propagation distance and the property of absorbing materials. Since the light attenuation depends on the absorption wavelengths of the surrounding medium, waveguide sensing can differentiate materials adhering to the waveguide boundary by absorption spectroscopy. The sensitivity of the waveguide depends on the amount of evanescent field extending to the medium. For a single-mode waveguide, the strengths of evanescent fields depend on the waveguide geometry, refractive index, wavelengths and light polarization.

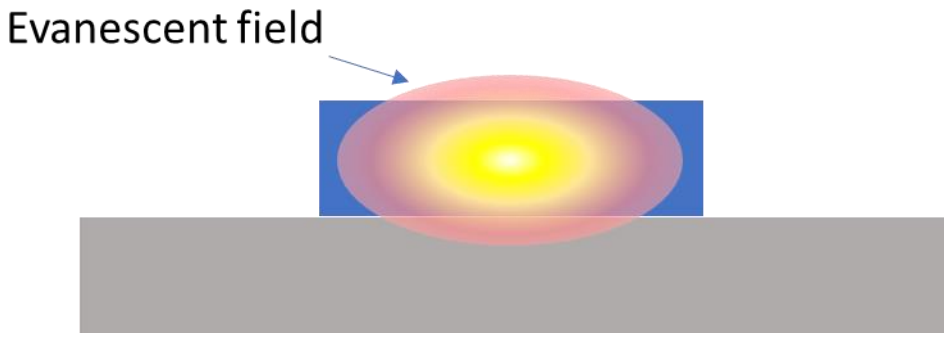

Figure 5.1 A waveguide mode with evanescent fields extending to the surrounding medium

5.3 Experimental methods

5.3.1 Fabrication of SiN waveguide sensor and gas chamber

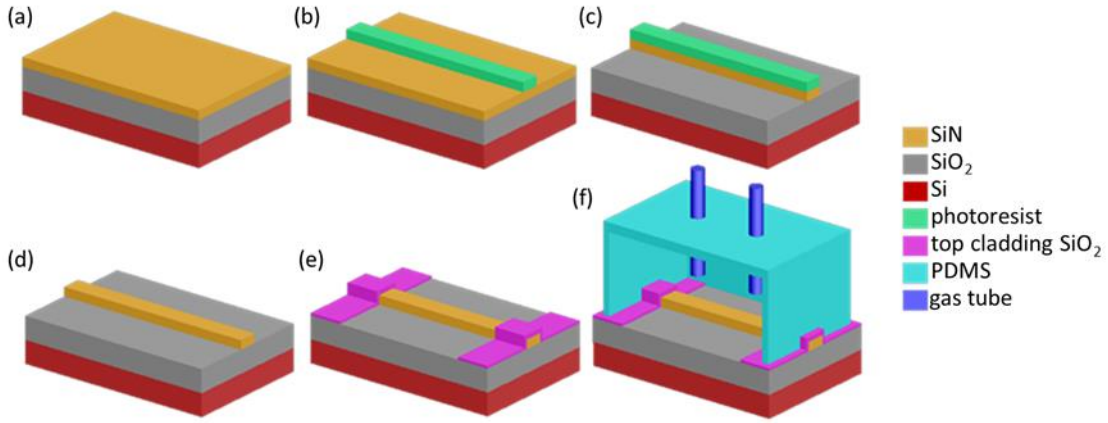

Figure 5.2 Fabrication process of the SiN waveguide and its assembly with a PDMS chamber. (a) Deposition of SiN thin film by LPCVD. (b) Creation of waveguide patterns by photolithography. (c) Transfer of the waveguide pattern to the SiN layer by RIE. (d) Removal of photoresist. (e) Deposition of the top SiO_2 cladding layer. (f) Bonding of the PDMS chamber to the waveguide sensor.

Figure 5.2 (a) - (f) illustrates the fabrication of mid-IR SiN waveguides and a polydimethylsiloxane (PDMS) chamber developed for VOC detection. In step (a), a low-stress SiN thin film with thickness T = 1 μm was deposited on a Si wafer by LPCVD. Between the SiN and the Si is a 3 μm thick thermo-oxide acting as the low-refractive-index under-cladding layer. In step (b), the pattern of waveguides was generated on top of the SiN thin film via photolithography. The waveguide pattern was then transferred into the SiN thin film layer in step (c) using reactive ion etching (RIE). After removing the photoresist in step (d), a 3 μm thick SiO_2 layer was deposited on both sides of the SiN waveguide by plasma-enhanced chemical vapor deposition (PECVD). The center of the waveguide was left open for VOC detection as shown in step (e). The length of the waveguide sensing region, where the mid-IR evanescent wave interacted with the VOCs, is 8 mm long. A PDMS (Dow Corning Sylgard 184) chamber was prepared by

dropping the PDMS precursor into a customized mold. In step (f), the molded PDMS was bonded to the SiN waveguide device to form a sealed gas chamber. The top SiO_2 layer patterned in step (e) prevented direct contact between the PDMS and the SiN waveguides to prevent absorption of the PDMS chamber material from interfering with the sensing measurement.

5.3.2 Setup for SiN waveguide characterization and VOC absorption measurement

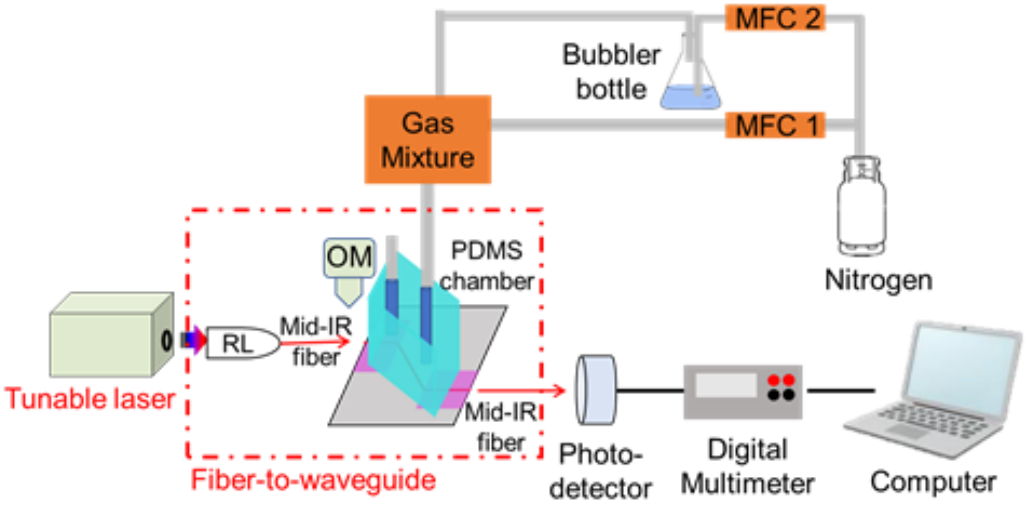

Figure 5.3 Experimental setup of the VOC detection measurement. Mid-IR probe light from the laser was coupled into the waveguide using a butt-coupling method. The guided light was collected by another fiber after the waveguide end-facet. VOC vapor was carried by N2. The flow rate the VOC concentration were controlled by the MFCs.

Figure 5.3 shows a schematic of the experimental set-up for waveguide characterization and VOC detection via a fiber-waveguide-fiber configuration. A tunable mid-IR laser (M Squared Firefly) with 150 kHz pulse repetition rate, 10 ns pulse duration, and 150 mW average power, was used as the light source. The wavelength tuning range of the laser is from 2.5 μm to 3.7 μm. The laser light was coupled into a single mode ZrF_4 fiber (Thorlabs) through a reflective lens collimator (RL) and then butt-coupled to the SiN waveguide. The fine position adjustment between the fiber

and the waveguide was monitored with an optical microscope. The coupling loss was 5.2 dB and the waveguide loss was 2.1 dB/cm at 3.5 μm wavelength.

Three VOCs (acetone, ethanol, and isoprene) were used as the analytes. VOC vapors were prepared by flowing nitrogen gas through bottles with VOCs in liquid form. The flow rates of the VOC vapors and the nitrogen carrier gas were regulated by mass flow controllers (MFCs). The gas phase analyte was delivered into the sealed PDMS chamber with the waveguide sensor inside. The gas pressure into the PDMS chamber was monitored by the mass flow controllers and pressure regulators. The temperature of the system and the PDMS was maintained at room temperature 20 °C. The intensity of the waveguide light was attenuated according to the mid-IR absorption spectra of the VOCs. Light propagated through the waveguide was collected by a multimode ZrF_4 fiber with a 400 μm core diameter (Thorlabs). The fiber was connected to a photodetector and the light intensity was read by a digital multimeter and recorded in a computer.

5.4 Results and discussion

5.4.1 Characterization of SiN waveguides and VOCs absorption measurement

Figure 5.4 (a) shows the fabricated SiN waveguide sensor with the attached PDMS gas chamber. The input and output waveguides were offset by 5 mm to minimize contributions from background light that was not coupled into the waveguide. Figure 5.4 (b) is an SEM image of the SiN waveguide array, where the waveguide width is 10 μm. Figure 5.4 (c) shows the waveguide mode of the SiN waveguide captured at $\lambda = 3.3$ μm by a liquid-nitrogen cooled mid-IR camera (IRC 800 series, IRcameras). A sharp spot corresponding to a fundamental waveguide mode was observed, and no scattering was found in the entire field of view. This indicates that the input light was well confined within the SiN waveguide, and that the background light in the substrate layer was minimized by the off-set design.

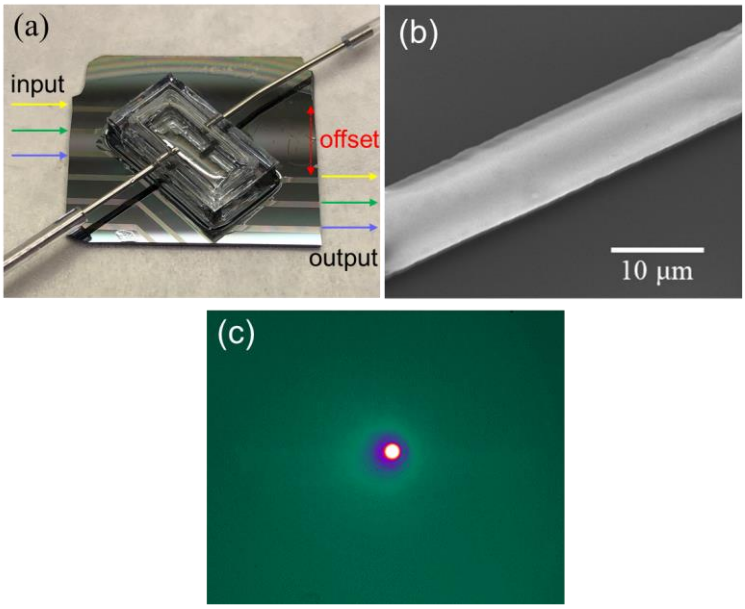

Figure 5.4 (a) The sensor device with SiN waveguides and a PDMS chamber. The input and output waveguides were offset by 5 mm. (b) Image of an array of SiN waveguides. (c) The mode image from a single SiN waveguide.

5.4.2 FDTD analysis of waveguide modes and mid-IR sensitivity

Mode profiles of the SiN and Si waveguides and their sensitivities were calculated using FDTD. FDTD modeling was used to evaluate the correlation between the sensitivity of mid-IR waveguides made by different materials and structures. Figure 5.5 (a) - (d) shows the 2-D waveguide modes for various waveguide structures at $\lambda = 3.3$ μm, and Figure 5.5 (e) - (h) displays the corresponding 1-D light intensity and refractive indexes distributions along the z-axis at $x = 0$ μm. The waveguides have the same width of 10 μm. Two different waveguide heights of $T = 1$ μm and 2 μm were considered for the transverse magnetic (TM) polarization. The waveguide sensing performance was evaluated by comparing the evanescent field intensity distribution for the two waveguides. The $T = 1$ μm Si waveguide showed a weak evanescent field extending to the outer medium ($z > 1$ μm), while the $T = 1$ μm SiN waveguides showed a strong evanescent field outside of the waveguide. Theintensity profile remained the same in the x direction. As the height of the waveguide was increased to $T = 2$ μm, the intensity of the evanescent field significantly decreased for both the SiN and Si waveguides, as illustrated in Figure 5.5 (c) and (d), respectively. However, the SiN waveguide still showed a stronger field than the Si waveguide.

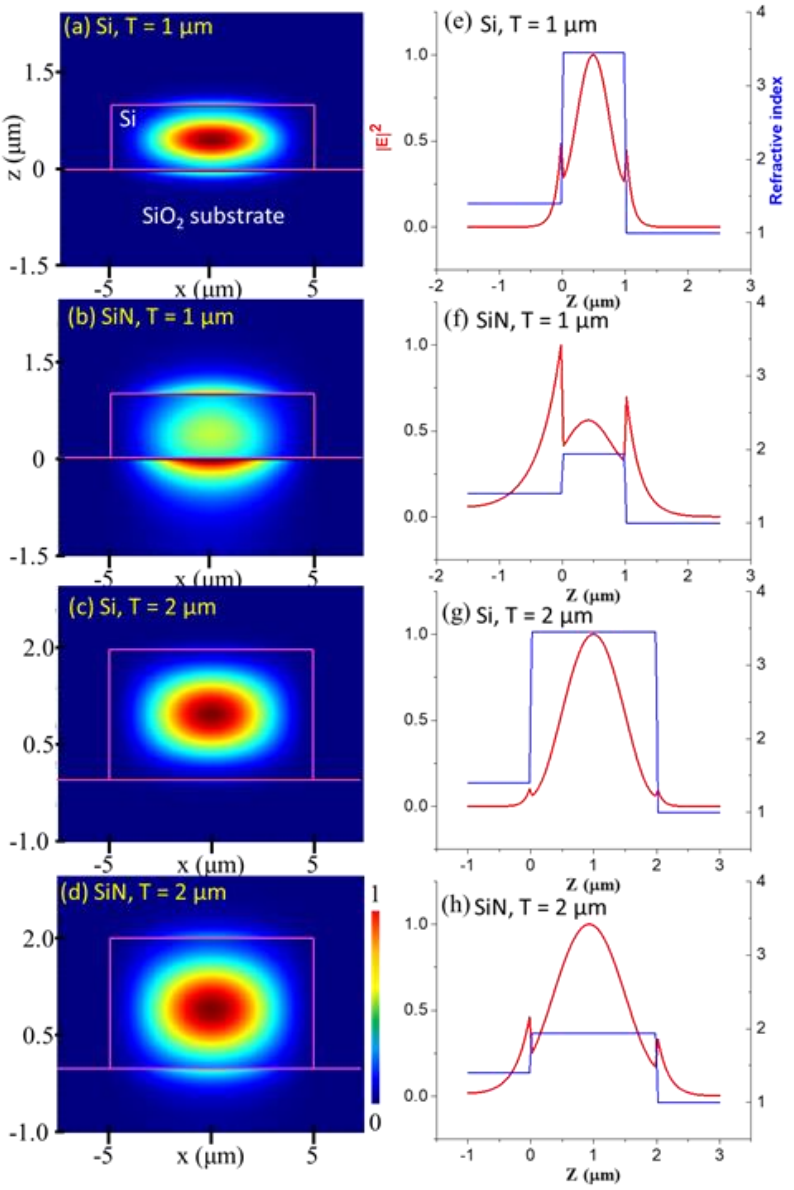

Figure 5.5 (a) - (d) Simulated 2-D waveguide modes and (e) - (h) 1-D intensity profiles along the z-axis for heights T = 1 and 2 µm for the Si and SiN waveguides, respectively. TM polarization was selected for the waveguide modes.

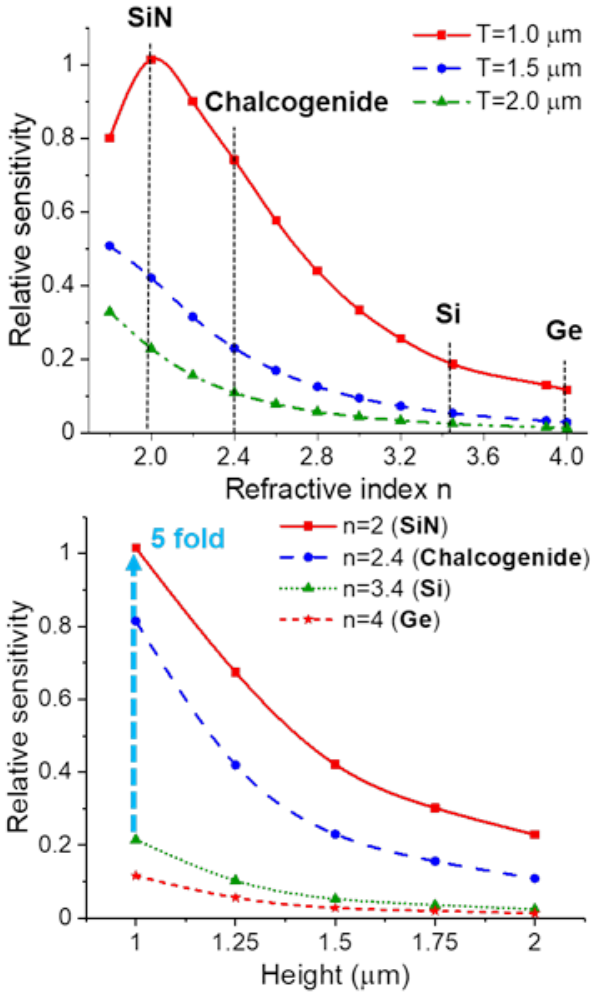

Figure 5.6 (a) Sensitivity vs refractive index, **n,** at heights of T = 1, 1.5, and 2 μm. (b) Sensitivity vs waveguide height T at **n** = 2, 2.4, 3.45 and 4, corresponding to SiN, chalcogenide, Si and Ge materials, respectively.

The FDTD method was also used to analyze the sensitivity of the mid-IR waveguides. The sensitivity of the waveguide was first defined as the attenuation of the waveguide intensity, which is equivalent to the waveguide propagation loss per unit length, upon exposure to an external medium. The relative sensitivity was then calculated by comparing its value with the sensitivity from the T =1 SiN waveguide. Figure 5.6 (a) shows the variation in sensitivity when the waveguide materials are Ge, Si, chalcogenides, and SiN, at heights T = 1.0, 1.5, and 2.0 μm. The refractive indexes corresponding to the materials are labeled on the figure. The waveguide sensitivity decreased monotonically at T = 1.5 and 2.0 μm when n increased. At T = 1 μm, the SiN showed a 10x, 5x, and 1.25x higher sensitivity than Ge, Si, and chalcogenide because of its lower refractive index, which led to a stronger evanescent field. An exception was found at n=1.8, where the waveguide mode was pushing into the undercladding layer so the evanescent field above the waveguide surface decreased. Similar sensitivity enhancement was also found for the T = 1.5 and 2 μm waveguides. The sensitivity variation due to the waveguide height is shown in Figure 5.6 (b). As depicted, the SiN waveguide sensitivity was significantly higher than the Si sensitivity, regardless of the height. As the height T decreased from 2 μm to 1 μm, we observed a three-fold improvement for both SiN and Si waveguides. The sensitivity vs. wavelength was also investigated and illustrated in Figure 5.7. Again, the sensitivity was systematically higher for the SiN waveguide, but the change of sensitivity was almost negligible for both waveguide materials across the 3.2 to 3.5 μm wavelength range, indicating the waveguide sensors have uniform performance over a broad spectrum, which is critical for mid-IR VOCs analysis.

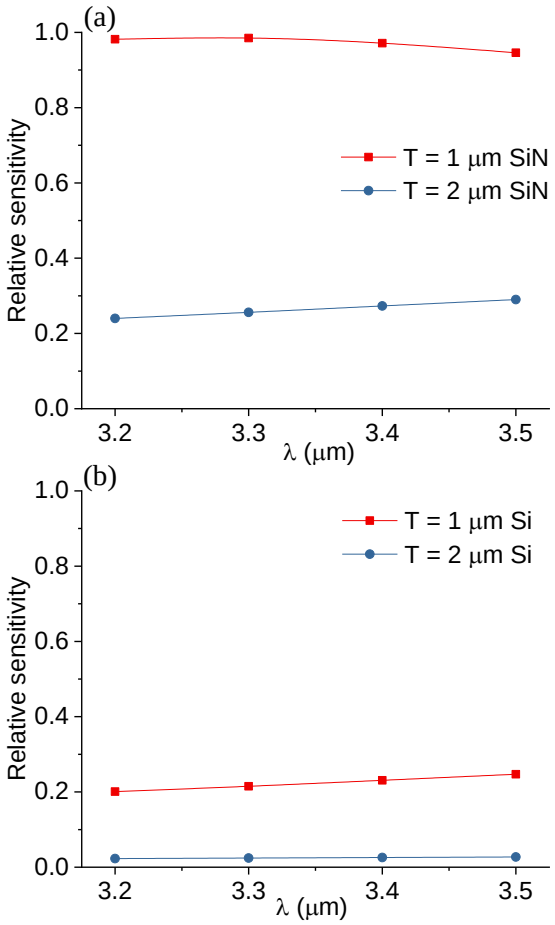

Figure 5.7 The sensitivity vs wavelength (λ) for (a) SiN and (b) Si waveguides at heights T = 1 and 2 μm, respectively.

5.4.3 Real-time VOC detection and absorption spectrum characterization

Figure 5.8 shows real-time VOC detection using the mid-IR SiN waveguide sensor illustrated in Figure 5.3. The SiN waveguide had a width of 10 μm and a height of 1 μm. The lowest T of the SiN and Si waveguides that can effectively confine the mid-IR lightwave is 1 μm and 0.85 μm, respectively. A SiN waveguide thinner than 1 μm will decrease the fiber-to-waveguide butt-coupling efficiency, since there is no conventional mid-IR lensed fiber. During the measurement, pure nitrogen was first injected into the PDMS chamber, and the waveguide intensity obtained was defined as the baseline. Once the waveguide intensity stabilized, VOC vapor was injected into the

PDMS chamber until the waveguide intensity stabilized. Each measurement was performed across three to four cycles of VOC injection and nitrogen purging to ensure the results were consistent and repeatable. The transient response during the acetone, ethanol, and isoprene measurements are plotted in Figure 5.8 (a), (b), and (c), respectively and showed a deviation over time within 1% for each of the gases.

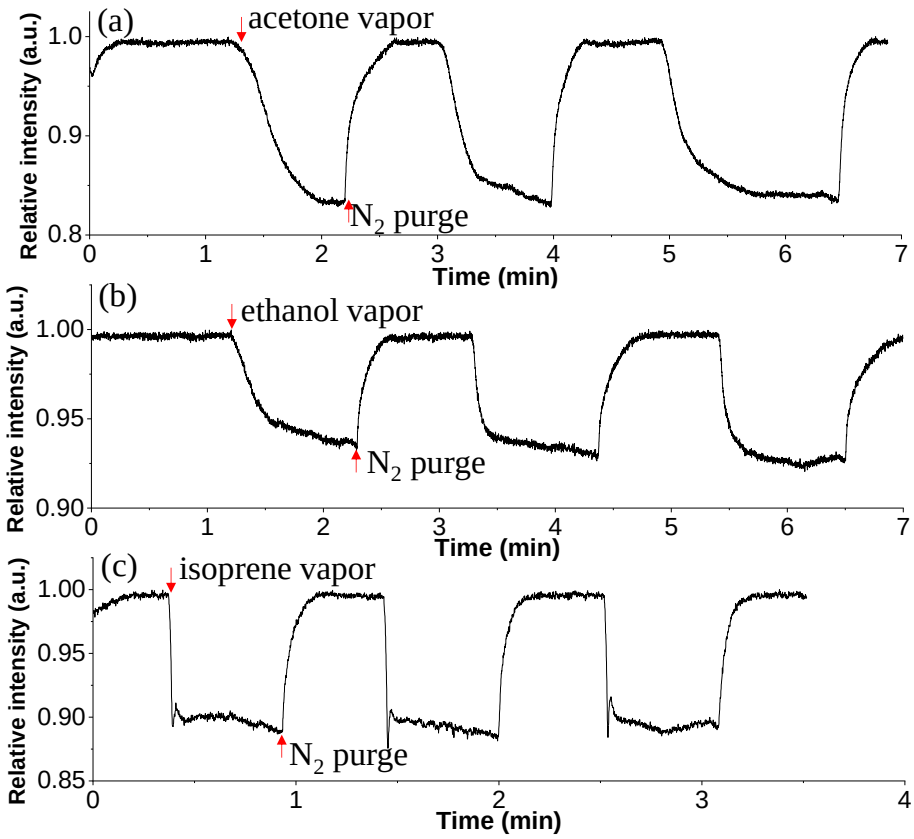

Figure 5.8 Real-time mid-IR monitoring of pulsed VOCs using SiN waveguides of width = 10 μm and height = 1 μm: (a) acetone at λ = 3.375 μm, (b) ethanol at λ = 3.375 μm, and (c) isoprene at λ = 3.400 μm.

The vibrational bands caused by the C-H stretching vibrations for acetone are 3.305 μm with A1 symmetry and3.168 μm with F2 symmetry. For ethanol, there are symmetric stretching vibration at 3.412 μm and symmetric stretching vibration at 3.364 μm. For acetone and ethanol vapor, the waveguide light intensity decreased over time when their vapor flowed into the chamber and then reached an equilibrium state after 10 – 20 s, indicating the VOC molecules steadily attached to the waveguide surface. Once the nitrogen was reinjected into the chamber, the waveguide intensity increased and recovered to its initial intensity level within 20 s. For isoprene, the waveguide light intensity dropped nearly instantaneously once the isoprene vapor was injected due to its high volatility. These results indicate that the SiN waveguide can detect different VOCs and measure their transient response. Unlike chalcogenide waveguides, due to the high chemical stability of the SiN and its resistance to moisture, our SiN waveguide sensor does not demonstrate degradation of signal and can be used for long-term repeatable VOCs monitoring.

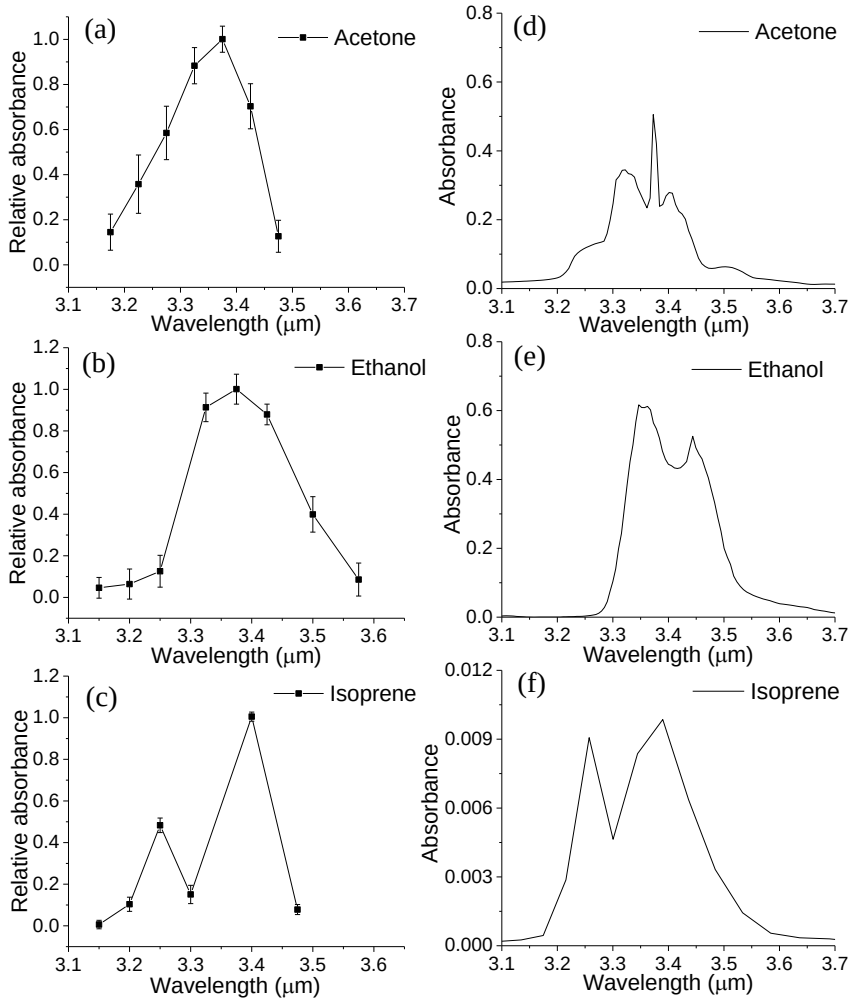

Figure 5.9 Mid-IR absorption spectra of acetone, ethanol, and isoprene. (a) - (c) Results from SiN waveguide measurement. (d) - (f) Spectra from the NIST database [35].

The absorption spectrum of VOCs can be calculated using the real-time measurement according to the Beer's law equation $A = -\log(I/I_0)$, where A is the absorbance, and I and I_0 are the waveguide intensities with and without the VOC, respectively. The spectra of acetone, ethanol and isoprene measured by the SiN waveguide are plotted in Figure 5.9 (a) - (c), where the absorbance in y-axis is normalized to its maximum. Note that the spectra are not meant to show the ability to separate these gas molecules spectrally but rather to show that the characteristic absorption bands caused by the C-H stretching vibrations between λ = 3.1 and 3.6 μm could be observed. The spectral features were consistent with FTIR spectra from the NIST WebBook database shown in Figure 5.9 (d) - (f), though the resolution of our tunable laser was not as high. For instance, the major absorption peak at λ = 3.35 μm was depicted for acetone and at 3.4 for μm ethanol for our system, but not the triplet or doublet as depicted using FTIR. However, the two broader isoprene absorption peaks at λ = 3.25 and 3.4 μm were depicted for both systems. Figure 5.10 shows the relative absorbance of acetone using a Si waveguide, compared to the results obtained using the SiN waveguides. Both Si and SiN waveguides were 10 μm wide and 1 μm tall in these experiments. The results of Figure 5.10 experimentally confirm the primary result anticipated from the FTID modeling, showing that attenuation (and therefore sensitivity) in the SiN waveguide was five times stronger compared to that of the Si waveguide. Figure 5.11 shows the relative absorbance with relative concentration of the individual VOCs. Gas concentration was controlled by adjusting the flow rates of MFC 1 and MFC 2; see Figure 5.3. The x-axis in Figure 5.11 is the ratio of flow rates: (MFC2)/(MFC1 + MFC2). We observe a monotonic increase in relative absorbance with VOC concentration, which is fairly linear below a ratio of 0.7 and then follows the nonlinear increase at higher ratios. The absorption curve can be explained by a superposition of an adsorption isotherm and a linear adsorption increase caused by the non-adhesive analytes within the waveguide's

evanescent field. In addition, applying the Antoine equation and gas flow rates, the limits of detection (LOD) of the concentration were 1.2 % for acetone, 1.3 % for ethanol and 2.5 % for isoprene [36]. The sensitivity of our mid-IR waveguide is better than the refractive-index-based sensing using a visible waveguide because of the strong characteristic mid-IR C-H vibrational absorption [37]. In the future, our waveguide sensitivity can be further increased with the use of slot waveguides and nanoparticles [38,39]. We expect that these advancements can enhance sensitivity by 100x, bringing it closer to that of MOS sensor of sub ppm level [40,41]. The potential for enhancement of sensitivity of waveguide-based sensing, taken together with intrinsically high, spectroscopic selectivity of Mid-IR detection [42] make this approach promising for future sensing applications of multiple gaseous analytes.

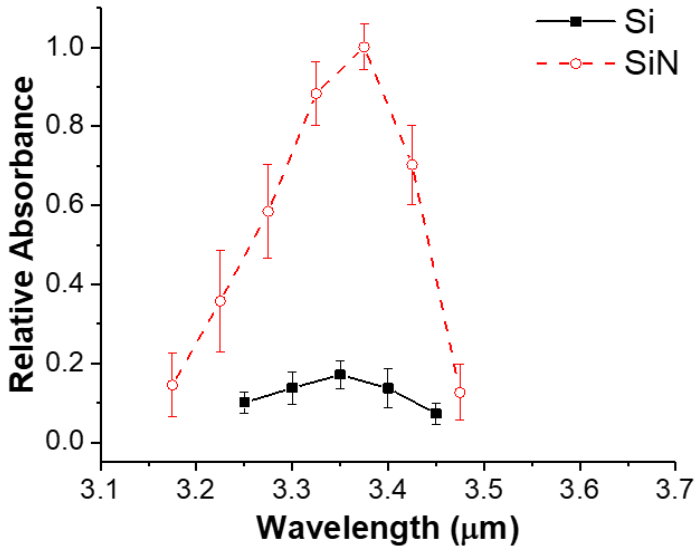

Figure 5.10 Measured results of acetone using SiN waveguides compared with Si waveguides. The waveguide width = 10 μm and height H = 1 μm.

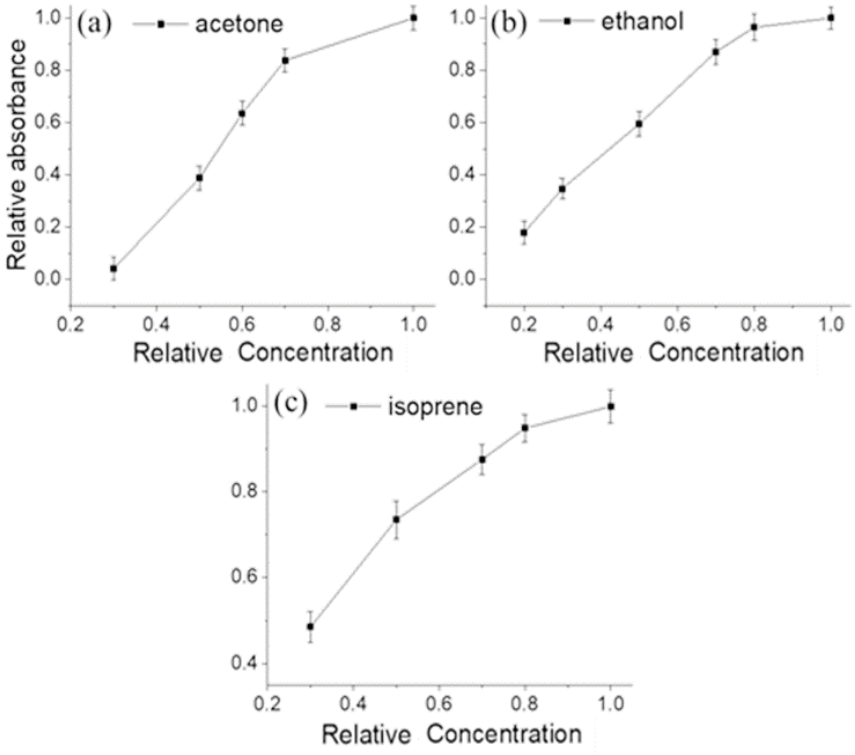

Figure 5.11 Relative absorbance vs relative VOC concentration for (a) acetone at λ = 3.375 μm, (b) ethanol at λ = 3.375 μm, and (c) isoprene at λ = 3.400 μm.

5.5 Conclusions

Mid-IR Si and SiN waveguide sensors were evaluated theoretically and experimentally as robust, chemically stable platforms for on-chip VOC detection. Utilizing C-H stretching vibrational mid-IR region between 3.1 to 3.5 μm, acetone, ethanol, and isoprene vapors were detected in real time using both waveguides. We demonstrated that due to their low refractive index, SiN waveguides had five-times higher sensitivity as compared to Si waveguides, and unlike Si waveguides were able to resolve the mid-IR absorption spectra of VOCs in the entire C-H strength region. Because of its CMOS compatibility, the proposed waveguide sensor can be integrated with wireless electronics and potentially provide a compact module for sensing of gaseous analytes for health, agricultural and environmental applications.

5.6 References

[1] Schnabel, R. *et al.* Analysis of volatile organic compounds in exhaled breath to diagnose ventilator-associated pneumonia. *Sci. Rep.* 5, 1-10 (2015).

[2] Ahmed, W. M. *et al.* Exhaled volatile organic compounds of infection: a systematic review. *ACS Infect. Dis.* **3**, 695-710 (2017).

[3] Jansen, R. *et al.* Detection of diseased plants by analysis of volatile organic compound emission. *Annu. Rev. Phytopathol.* **49**, 157-174 (2011).

[4] Li, Z. *et al.* Non-invasive plant disease diagnostics enabled by smartphone-based fingerprinting of leaf volatiles. *Nature Plants* **5**, 856-866 (2019).

[5] Cetin, E., Odabasi, M. & Seyfioglu, R. Ambient volatile organic compound (VOC) concentrations around a petrochemical complex and a petroleum refinery. *Sci. Total Environ.* **312**, 103-112 (2003).

[6] Lamote, K. *et al.* Breath analysis by gas chromatography-mass spectrometry and electronic nose to screen for pleural mesothelioma: a cross-sectional case-control study. *Oncotarget* **8**, 91593 (2017).

[7] Wang, X. R., Cassells, J. & Berna, A. Z. Stability control for breath analysis using GC-MS. *J. Chromatogr.* B 1097, 27-34 (2018).

[8] Masikini, M., Chowdhury, M. & Nemraoui, O. Metal oxides: Application in exhaled breath acetone chemiresistive sensors. *J. Electrochem. Soc.* **167**, 037537 (2020).

[9] Righettoni, M., Amann, A. & Pratsinis, S. E. Breath analysis by nanostructured metal oxides as chemo-resistive gas sensors. *Mater. Today* **18**, 163-171 (2015).

[10] Paul, R. K., Badhulika, S., Saucedo, N. M. & Mulchandani, A. Graphene nanomesh as highly sensitive chemiresistor gas sensor. *Anal. Chem.* **84**, 8171-8178 (2012).

[11] Park, C.-O., Fergus, J., Miura, N., Park, J. & Choi, A. Solid-state electrochemical gas sensors. *Ionics* **15**, 261-284 (2009).

[12] Marchi, I., Rudaz, S. & Veuthey, J.-L. Atmospheric pressure photoionization for coupling liquid-chromatography to mass spectrometry: a review. *Talanta* **78**, 1-18 (2009).

[13] Henderson, B. *et al.* Laser spectroscopy for breath analysis: towards clinical implementation. *Appl. Phys. B* **124**, 161 (2018).

[14] Selvaraj, R., Vasa, N. J., Nagendra, S. & Mizaikoff, B. Advances in Mid-Infrared Spectroscopy-Based Sensing Techniques for Exhaled Breath Diagnostics. *Molecules* **25**, 2227 (2020).

[15] Lin, P. T. *et al.* Chip-scale Mid-Infrared chemical sensors using air-clad pedestal silicon waveguides. *Lab Chip* **13**, 2161-2166 (2013).

[16] Su, P. *et al.* Monolithic on-chip mid-IR methane gas sensor with waveguide-integrated detector. *Appl. Phys. Lett.* **114**, 051103 (2019).

[17] Kumari, B., Barh, A., Varshney, R. & Pal, B. Silicon-on-nitride slot waveguide: a promising platform as mid-IR trace gas sensor. *Sens. Actuators B: Chem.* **236**, 759-764 (2016).

[18] Jin, T., Zhou, J. & Lin, P. T. Real-time and non-destructive hydrocarbon gas sensing using mid-infrared integrated photonic circuits. *RSC advances* **10**, 7452-7459 (2020).

[19] Chang, Y.-C. *et al.* Cocaine detection by a mid-infrared waveguide integrated with a microfluidic chip. *Lab on a Chip* **12**, 3020-3023 (2012).

[20] Messica, A., Greenstein, A. & Katzir, A. Theory of fiber-optic, evanescent-wave spectroscopy and sensors. *Appl.Opt.* **35**, 2274-2284 (1996).

[21] Pandraud, G. *et al.* Evanescent wave sensing: new features for detection in small volumes. *Sens. Actuators A: Phys.* **85**, 158-162 (2000).

[22] Jin, T., Zhou, J., Lin, H.-Y. G. & Lin, P. T. Mid-infrared chalcogenide waveguides for real-time and nondestructive volatile organic compound detection. *Analytical chemistry* **91**, 817-822 (2018).

[23] Ebnesajjad, S. & Ebnesajjad, C. *Surface treatment of materials for adhesive bonding*. (William Andrew, 2013).

[24] Krstic, Z. & Krstic, V. D. Silicon nitride: the engineering material of the future. *Journal of Materials Science* **47**, 535-552 (2012).

[25] Tai Lin, P., Singh, V., Kimerling, L. & Murthy Agarwal, A. Planar silicon nitride mid-infrared devices. *Appl. Phys. Lett.* **102**, 251121 (2013).

[26] Lin, P. T. *et al.* Label-Free Glucose Sensing Using Chip-Scale Mid-Infrared Integrated Photonics. *Adv. Opt. Mater.* **4**, 1755-1759 (2016).

[27] Koompai, N. *et al.* Analysis of Si3N4 waveguides for on-chip gas sensing by optical absorption within the mid-infrared region between 2.7 and 3.4 μm. *Results Phys.* **16**, 102957 (2020).

[28] Antonacci, G. *et al.* Ultra-sensitive refractive index gas sensor with functionalized silicon nitride photonic circuits. *APL Photonics* **5**, 081301 (2020).

[29] Chen, Y., Lin, H., Hu, J. & Li, M. Heterogeneously integrated silicon photonics for the mid-infrared and spectroscopic sensing. *ACS Nano* **8**, 6955-6961 (2014).

[30] Righettoni, M. & Tricoli, A. Toward portable breath acetone analysis for diabetes detection. *J. Breath Res.* **5**, 037109 (2011).

[31] Sun, M. *et al.* Study of breath acetone and its correlations with blood glucose and blood beta-hydroxybutyrate using an animal model with lab-developed type 1 diabetic rats. *RSC Adv.* **5**, 71002-71010 (2015).

[32] Andresen-Streichert, H., Müller, A., Glahn, A., Skopp, G. & Sterneck, M. Alcohol biomarkers in clinical and forensic contexts. *Deutsches Ärzteblatt Int.* **115**, 309 (2018).

[33] Bajtarevic, A. *et al.* Noninvasive detection of lung cancer by analysis of exhaled breath. *BMC Cancer* **9**, 348 (2009).

[34] Zhou, X. *et al.* Nanomaterial-based gas sensors used for breath diagnosis. *J. Mater. Chem. B* **8**, 3231-3248 (2020).

[35] Coblentz Society, Inc., "Evaluated Infrared Reference Spectra" in NIST Chemistry WebBook, NIST Standard Reference Database Number 69, Eds. P.J. Linstrom and W.G. Mallard, National Institute of Standards and Technology, Gaithersburg MD, 20899, https://doi.org/10.18434/T4D303, (retrieved November 8, 2020).

[36] Yaws, C. L. *The Yaws handbook of vapor pressure: Antoine coefficients*. (Gulf Professional Publishing, 2015).

[37] Nitiss, Edgars, Arturs Bundulis, Andrejs Tokmakovs, Janis Busenbergs, and Martins Rutkis. "All-Organic Waveguide Sensor for Volatile Solvent Sensing." (2019).

[38] Al Husseini, D. *et al.* Surface Functionalization Utilizing Mesoporous Silica Nanoparticles for Enhanced Evanescent-Field Mid-Infrared Waveguide Gas Sensing. *Coatings* **11**, 118 (2021).

[39] Lin, P. T. *et al.* Mid-infrared spectrometer using opto-nanofluidic slot-waveguide for label-free on-chip chemical sensing. *Nano Lett.* **14**, 231-238 (2014).

[40] Dey, A. Semiconductor metal oxide gas sensors: A review. *Materials Science and Engineering: B* **229**, 206-217 (2018).

[41] Zhang, J., Qin, Z., Zeng, D. & Xie, C. Metal-oxide-semiconductor based gas sensors: screening, preparation, and integration. *Physical Chemistry Chemical Physics* **19**, 6313-6329 (2017).

[42] Al Husseini, D. *et al.* All-nanoparticle layer-by-layer coatings for Mid-IR on-chip gas sensing. *Chem. Commun.* **56**, 14283-14286 (2020).

CHAPTER VI

FUTURE WORK AND CONCLUSIONS

This work explored the mid-infrared sensing for spectroscopic material characterization. Traditional mid-IR spectroscopy relies on bulk FTIR instrument which is unpractical for real-time, point of use applications. To address this issue, this work explored the mid-IR sensing utilizing mid-IR integrated photonics. A real-time noninvasive mid-IR multi-spectral material characterization system was proposed along with the key elements. To have the on-chip mid-IR multi-spectral sensing, an on-chip light source is needed. Nonlinear optical process such as optical parametric process can generate photons in mid-IR region. However, nonlinear materials that can efficiently be used for mid-IR on-chip light sources is still unexplored. Therefore, this study examined the nonlinear property of $BaTiO_3$ in mid-IR by second harmonic generation with a mid-IR pump source.

Another issue for mid-IR sensing is that it is difficult for single particle characterization. Vortex beam with orbital angular momentum can trap single particles. With mid-IR vortex beam, it is possible to trap single particles and analyze its mid-IR spectrum simultaneously. In this study, mid-IR vortex beam generation was first simulated using FDTD. Vortex beam generation in mid-IR was also experimentally demonstrated by 3D printed micro- spiral phase plates.

Last, mid-IR sensing was applied to VOC gas analysis. Integrated photonic waveguide sensor was used detect VOC gases. Currently, such integrated waveguide sensor suffers from low sensitivity which limits its applications. This study showed the materials refractive index plays an important role for waveguide sensors. SiN waveguides showed a 5 times enhancement compared with Si waveguides. To further enhance the sensitivity, nanoparticle coatings on the waveguide

was demonstrated with another 5-fold enhancement. With slot waveguides and nanoparticle coatings, the sensitivity of the waveguide sensors is believed to detect VOCs of ppm level.

With the demonstration of vortex beams, nonlinear materials and VOC gas sensing in mid-IR, this work laid a foundation for the future mid-IR integrated multi-spectral sensing systems.

As a direction for the future work, the mid-IR vortex beam can be utilized for single particle analysis. The first step would be to demonstrate single particle trapping by the mid-IR vortex beams. Next step is to analyze the absorption of the particle with a back photodetector. If a series of vortex beams with different wavelengths applied to the particle, the absorption at those different wavelengths of the particle could constitute the absorption spectrum of the particle, enabling single particle composition analysis.

For the nonlinear optical process, OPO or OPA could be integrated to the integrated photonics devices, providing the on-chip multi-wavelengths mid-IR light sources. The quasi-phase matching condition is critical for the OPO or OPA process. The possible developments of the on-chip OPO or OPA for mid-IR light generation include:

- Development of waveguide on periodically poled $LiNbO_3$ or $BaTiO_3$
- Development of GaN micro-ring devices using GaN epitaxial thin films for OPO process. Modal phase matching could be used for phase-matching condition.

The mid-IR integrated photonic sensors was demonstrated for detection of VOC gases. The sensitivity of the waveguide sensors still needs improvement for detecting VOCs of ppm or sub-ppm level. New waveguide structure such as slot waveguide can be explored. Instead of evanescent wave sensing by ridge waveguide, slot waveguide provides high sensitivity since all the slot waveguide mode can interact with the absorbing gases. For spectrum analysis, on-chip

spectrometer consisting of micro-rings along with tunable on-chip OPO/OPA light sources, can be explored.